

Alma Mater Studiorum - Università di Bologna

DOTTORATO DI RICERCA IN

IL FUTURO DELLA TERRA, CAMBIAMENTI CLIMATICI E SFIDE  
SOCIALI

Ciclo 35

**Settore Concorsuale:** 02/C1 - ASTRONOMIA, ASTROFISICA, FISICA DELLA  
TERRA E DEI PIANETI

**Settore Scientifico Disciplinare:** FIS/06 - FISICA PER IL SISTEMA TERRA E IL  
MEZZO CIRCUMTERRESTRE

EXPLOITING SPECTRALLY RESOLVED SATELLITE OBSERVATIONS  
TO ASSESS THE PERFORMANCE OF CLIMATE MODELS

**Presentata da:** Stefano Della Fera

**Coordinatore Dottorato**  
Prof.ssa Silvana Di Sabatino

**Supervisore**  
Dott.ssa Piera Raspollini

**Co-supervisor**  
Prof. Tiziano Maestri  
Dott. Federico Fabiano  
Dott. Ugo Cortesi  
Dott. Marco Ridolfi  
Prof. Jost von Hardenberg

**Esame finale anno 2023**



# Abstract

The accurate representation of the Earth Radiation Budget by General Circulation Models (GCMs) is a fundamental requirement to provide reliable historical and future climate simulations.

In this study, we found reasonable agreement between the integrated energy fluxes at the top of the atmosphere simulated by 34 state-of-the-art climate models and the observations provided by the Cloud and Earth Radiant Energy System (CERES) mission on a global scale, but large regional biases have been detected throughout the globe. Furthermore, we highlighted that a good agreement between simulated and observed integrated Outgoing Longwave Radiation (OLR) fluxes may be obtained from the cancellation of opposite-in-sign systematic errors, localized in different spectral ranges. To avoid this and to understand the causes of these biases, we compared the observed Earth emission spectra, measured by the Infrared Atmospheric Sounding Interferometer (IASI) in the period 2008-2016, with the synthetic radiances computed on the basis of the atmospheric fields provided by the EC-Earth GCM. To this purpose, the fast  $\sigma - IASI$  radiative transfer model was used, after its validation and implementation in EC-Earth.

From the comparison between observed and simulated spectral radiances, a positive temperature bias in the stratosphere and a negative temperature bias in the middle troposphere, as well as a dry bias of the water vapor concentration in the upper troposphere, have been identified in the EC-Earth climate model. The analysis has been performed in clear-sky conditions, but the feasibility of its extension in the presence of clouds, whose impact on the radiation represents the greatest source of uncertainty in climate models, has also been proven.

Finally, the analysis of simulated and observed OLR trends indicated good agreement and provided detailed information on the spectral fingerprints of the evolution of the main climate variables.



# Contents

<b>Introduction</b>	<b>15</b>
<b>1 Background</b>	<b>19</b>
1.1 Radiative transfer theory . . . . .	19
1.1.1 Radiance and spectral flux . . . . .	19
1.1.2 Radiative transfer equation . . . . .	21
1.2 The Earth Radiation Budget . . . . .	22
1.2.1 The Earth emission spectrum . . . . .	24
1.2.2 Energy Imbalance at TOA . . . . .	25
1.3 Climate models . . . . .	26
1.3.1 Energy Balance Model . . . . .	26
1.3.2 General Circulation Model . . . . .	26
1.3.3 Radiative Computation in Climate Models . . . . .	29
1.3.4 Matching the observations: the tuning technique . . . . .	33
<b>2 How well do climate models represent the Earth Energy Budget?</b>	<b>37</b>
2.1 The Coupled Model Intercomparison Project . . . . .	37
2.2 Climate Models Assessment . . . . .	38
2.2.1 Outgoing Longwave Radiation . . . . .	40
2.2.2 Outgoing Shortwave Radiation . . . . .	43
2.2.3 Cloud Radiative Effect . . . . .	44
2.2.4 Cloud Cover, Liquid and Ice content . . . . .	47
2.3 Conclusions . . . . .	48
<b>3 Teresina campaign: measurements of the Earth emission spectrum in the FIR and test of the <math>\sigma - IASI</math> radiative transfer model</b>	<b>51</b>
3.1 Teresina campaign . . . . .	51
3.2 The $\sigma$ -IASI radiative transfer model . . . . .	52
3.3 The inverse problem . . . . .	53
3.3.1 Maximum Likelihood . . . . .	54
3.3.2 The Gauss-Newton Method . . . . .	55
3.3.3 Averaging Kernels . . . . .	56
3.3.4 Retrieval strategy . . . . .	56
3.4 Validation of the retrieval . . . . .	57
3.5 Verification of the $\sigma$ -IASI radiative transfer model . . . . .	58
3.6 Conclusions . . . . .	59

---

<b>4</b>	<b>The contribution of IASI observed radiances to the detection of EC-Earth climate model biases</b>	<b>61</b>
4.1	Models	61
4.1.1	EC-Earth Climate Model	61
4.1.2	Implementation of the $\sigma$ -IASI RTM in the EC-Earth climate model	63
4.1.3	ECE radiance climatology	64
4.2	Observations	64
4.2.1	Fourier Transform Spectrometer	65
4.2.2	CERES	68
4.2.3	IASI radiance climatology	69
4.3	Results and Discussion	69
4.3.1	Model-Observation comparison strategy	69
4.3.2	Sensitivity of a simulated OLR spectrum to atmospheric temperature and gas concentrations	72
4.3.3	Assessment of EC-Earth biases in simulated clear-sky radiances with respect to IASI measurements	75
4.3.4	Temperature biases	76
4.3.5	Water vapour biases	80
4.3.6	Discussion	81
4.4	Conclusions	82
<b>5</b>	<b>Future perspectives</b>	<b>85</b>
5.1	Towards the EC-Earth-IASI comparison in all-sky conditions	85
5.2	Spectral trends	87
	<b>Conclusions</b>	<b>93</b>
	<b>Bibliography</b>	<b>99</b>

# List of Figures

1.1	Blackbody emission spectra for the Sun (temperature 5800 K) and Earth (temperature 255 K, as seen from space) as function of wavelength. . . . .	20
1.2	Earth global mean energy budget for July 2005-June 2015 (CERES dataset <a href="https://ceres.larc.nasa.gov/science/">https://ceres.larc.nasa.gov/science/</a> ). . . . .	23
1.3	Simulated Earth emission spectrum. . . . .	24
1.4	Example of the grid structure of a General Circulation Model. Figure from Edwards [2011] . . . . .	27
1.5	Scheme of the physical processes simulated in the "model physics" of General Circulation Models (from IFS documentation) . . . . .	30
1.6	Absorption coefficients due to carbon dioxide for a single layer (Pressure = 507 mbar) over the spectral range 630 – 700cm <sup>-1</sup> -a) absorption coefficients as function of the wavenumber; b) rearranged in ascending order. Figure from Mlawer et al. [1997] . . . . .	30
1.7	Most used overlap assumptions in climate models. Figure from Hogan and Illingworth [2000] . . . . .	32
1.8	Processes tuned in the ECHAM model in Mauritsen et al. [2012]. Parameters are (a) convective cloud mass flux above the level of nonbuoyancy, (b) shallow convective cloud lateral entrainment rate, (c) deep convective cloud lateral entrainment rate, (d) convective cloud water conversion rate to rain, (e) liquid cloud homogeneity, (f) liquid cloud water conversion rate to rain, (g) ice cloud homogeneity, and (h) ice particle fall velocity. . . . .	34
1.9	Example of tuning process described in Hourdin et al. [2017] involving the ice crystal fall velocity . . . . .	35
2.1	CMIP6 experiments configuration . . . . .	38
2.2	A: Observed OLR flux (top left); B: Multi-Model Mean of simulated OLR (top right); C: Difference (MODEL-OBSERVATION) (bottom left); D: Zonal multi-model mean and observed OLR (bottom right). The blue shade identifies the 1 $\sigma$ (standard deviation) of multi-model mean . . . . .	41
2.3	A: Observed OLRCS flux (top left); B: Multi-Model Mean of simulated OLRCS (top right); C: Difference (MODEL-OBSERVATION) (bottom left); D: Zonal multi-model mean and observed OLRCS (bottom right). The blue shade identifies the 1 $\sigma$ (standard deviation) of multi-model mean ( <i>ORLCS</i> ) averaged over 15 years . . . . .	42
2.4	TOA LW adjustment for (a) January, (b) April, (c) July, and (d) October based upon 10-yr climatology of CERES EBAF data for July 2005–June 2015 (units: $Wm^{-2}$ ). From Loeb et al. [2020] . . . . .	42

2.5	A: Observed RSR flux (top left); B: Multi-Model Mean of simulated RSR (top right); C: Difference (MODEL-OBSERVATION) (bottom left); D: Zonal multi-model mean and observed RSR (bottom right). The blue shade identifies the $1\sigma$ (standard deviation) of multi-model mean ( <i>RSR</i> ) averaged over 15 years . . . . .	44
2.6	A: Observed RSRCS flux (top left); B: Multi-Model Mean of simulated RSRCS (top right); C: Difference (MODEL-OBSERVATION) (bottom left); D: Zonal multi-model mean and observed RSRCS (bottom right). The blue shade identifies the $1\sigma$ (standard deviation) of multi-model mean ( <i>RSRCS</i> ) averaged over 15 years . . . . .	45
2.7	A: Observed CRE LW (top left); B: Multi-Model Mean of simulated CRE LW (top right); C: Difference (MODEL-OBSERVATION) (bottom left); D: Zonal multi-model mean and observed Cloud Cover (bottom right). The blue shade identifies the $1\sigma$ (standard deviation) of multi-model mean ( <i>CLT</i> ) averaged over 15 years . . . . .	46
2.8	A: Observed CRESW (top left) ; B: Multi-Model Mean of simulated CRESW (top right); C: Difference (MODEL-OBSERVATION) (bottom left); D: Zonal multi-model mean and observed Cloud Cover (bottom right). The blue shade identifies the $1\sigma$ (standard deviation) of multi-model mean ( <i>CLT</i> ) averaged over 15 years . . . . .	46
2.9	A: Observed Cloud Cover; B: Multi-Model Mean of simulated Cloud Cover; C: Difference (MODEL-OBSERVATION); D: Zonal multi-model mean and observed Cloud Cover. The blue shade identifies the $1\sigma$ (standard deviation) of multi-model mean ( <i>CLT</i> ) averaged over 15 years . . . . .	48
2.10	A: Zonal Cloud Liquid Water Path; B: Zonal Cloud Ice Water Path. The blue shade identifies the $1\sigma$ (standard deviation) of multi-model mean averaged over 15 years . . . . .	49
3.1	Examples of REFIR-PAD and IASI-Balloon measured spectra . . . . .	52
3.2	Newton's Method . . . . .	55
3.3	Comparison between the retrieved profiles of temperature (left) and water vapour (right), obtained from the inversion of REFIR-PAD measurements (rpad) and by the synergistic inversion of REFIR-PAD and IASI balloon measurements (syn). In the plot are also shown the measured profiles of temperature and water vapour provided by nearby radiosondes (Carolina, Floriano, Sao Luis). . . . .	58
3.4	Comparison between the observed (black) and simulated spectra (red) of REFIR-PAD and IASI balloon. For both spectra, the residuals (orange) and the measurement noise error ranges (blue) are plotted. . . . .	59
4.1	EC-Earth3 components and couplings . . . . .	62
4.2	COSP scheme from [Bodas-Salcedo et al., 2011] . . . . .	63
4.3	The dots indicate the center of the ECE model cells for which a spectral radiance is simulated. . . . .	65
4.4	Optical layout of a Michelson interferometer . . . . .	66
4.5	Sinc function . . . . .	67
4.6	IASI trace and geometry from [Clerbaux et al., 2009] . . . . .	68

## List of Figures

---

4.7	Number of observed (left) and simulated (right) spectral radiances that contribute to the clear-sky statistics, for each lat x long cell. . . . .	70
4.8	Number of observed (left) and simulated (right) spectral radiances that contribute to the clear-sky zonal means presented. . . . .	70
4.9	Spectrum simulated in clear-sky conditions over tropical ocean by the $\sigma$ -IASI RTM. The main absorption bands are highlighted. Dashed lines show the equivalent blackbody emission at typical surface (295 K) and tropopause (210 K) temperatures. . . . .	73
4.10	Absolute values of normalized Jacobians computed with $\sigma$ -IASI for a tropical standard atmosphere with respect to the temperature (top panel) and gases concentration (bottom panel). . . . .	74
4.11	Brightness Temperature differences (model - observations) over ocean, averaged over the period 2008 - 2016 . . . . .	76
4.12	Average (2008-2016) Brightness Temperatures computed by EC-Earth and measured by IASI over the tropical ocean [30° S, 30°N] (top panel). The bottom panel shows the BT differences model minus observation. . . . .	77
4.13	Brightness Temperature (BT) averaged in different spectral intervals over tropical ocean [30° S, 30°N]. The red line identifies the model BT while the black line describes the observed BT. The shadow areas represent the standard deviations. Note the different vertical scales used in the plots. On the right, the integrated jacobians of the temperature in the respective spectral bands. . . . .	78
4.14	Brightness Temperature (BT) averaged in different spectral intervals over the globe [60° S, 60°N] . . . . .	79
4.15	Differences between EC-Earth climate model and ERA5 reanalysis temperatures. Differences are a 15 years [2000 - 2014] average. . . . .	80
4.16	On the left, the integrated jacobians of the water vapour and temperature in the spectral bands 730 and 1400 $\text{cm}^{-1}$ . On the right, Brightness Temperature (BT) averaged at 1400 $\text{cm}^{-1}$ over tropical ocean [30° S, 30°N]. The red line identifies the model BT while the black line describes the observed BT. The shadow areas represent the standard deviations. . . . .	81
4.17	Differences between EC-Earth climate model and ERA5 water vapour concentration in the troposphere (left) and in the stratosphere (right). Differences are a 15 years [2000 - 2014] average. . . . .	82
4.18	Distribution of sea surface temperature for cloud fraction < 30 %, assuming the EC-Earth (red) or the CERES (grey) cloud fractions. The distributions were computed for tropical- [-30 °S, + 30° N] latitudes (left) and mid- [-60 °S, - 45° S] latitudes (right). . . . .	82
5.1	Simulated total cloud fraction for January 2008 - 06 UTC . . . . .	88
5.2	Radiance difference at 880 $\text{cm}^{-1}$ between method 3 and method 1 . . . . .	89
5.3	Zonal mean spectrally resolved linear trends from ECE climate model (2008-2016) . . . . .	90
5.4	Zonal mean spectrally resolved linear trends from IASI (2008-2016) . . . . .	91

5.5 Global Trends computed on the basis of ECE simulated radiances over the period 2008-2016. Panel A describes trends in the atmospheric window at  $850\text{ cm}^{-1}$ , panel B represents trends at  $660\text{ cm}^{-1}$ , panel C shows trends at  $730\text{ cm}^{-1}$  and panel D describes trends at  $1400\text{ cm}^{-1}$  . . . . . 92

# List of Tables

2.1	Global mean of CMIP6 models (AMIP simulations) and CERES over the period 2000-2014, with the respective standard deviations. . . . .	40
3.1	Degrees of freedom for each retrieved parameter type. We distinguish between results obtained from REFIR-PAD inversion (rpad) and synergistic inversion of REFIR-PAD and IASI balloon (syn). . . . .	59
4.1	Statistics of the IASI and ECE spectra contained in the respective climatologies . . . . .	71
4.2	Statistics of the IASI and ECE spectra contained in the respective climatologies after the application of the threshold . . . . .	71
4.3	Approximated spectral intervals of the atmospheric windows and the main absorption bands highlighted in Fig. 4.9. . . . .	72
4.4	Inferred BT biases estimated from the comparison between climate model outputs and ERA5 data and from the comparison of climate model and IASI BT climatologies . . . . .	79
4.5	Inferred BT biases estimated from the comparison between climate model outputs and ERA5 data and from the comparison of climate model and IASI BT climatologies . . . . .	81



# Acronyms

- ERB = Earth Radiation Budget
- EEI = Earth Energy Imbalance
- OLR = Outgoing Longwave Radiation
- RSR = Reflected Solar Radiation
- ASR = Absorbed Solar Radiation
- GCM = General Circulation Model
- CMIP = Coupled Model Intercomparison Projects
- RTM = Radiative Transfer Model
- TOA = Top of Atmosphere
- FIR = Far-Infrared
- MIR = Mid-Infrared
- GHG = Greenhouse Gas
- CERES = Cloud and Earth Radiant Energy System
- ERBE = Earth Radiation Budget Experiment
- IASI = Infrared Atmospheric Sounding Interferometer
- FORUM = Far-Infrared Outgoing Radiation and Monitoring
- REFIR-PAD = Radiation Explorer in the Far InfraRed for Applications and Development
- COSP = Cloud Feedback Model Intercomparison Project (CFMIP) Observation Simulator Package



# Introduction

Earth’s thermal equilibrium results from the balance between the incoming solar radiation, which is partly absorbed by the surface and the atmosphere and partly reflected back to space, and the Outgoing Longwave Radiation (OLR), the infrared energy emitted by the planet. Without external forcings, of natural or anthropic origin, over a long enough timescale compared to those controlling the redistribution of energy on a global scale, the net energy retained by the planet should be equal to zero at the top of the atmosphere (TOA).

For several decades, the dramatic increase in greenhouse gases (GHGs) and aerosol concentration in the atmosphere, both induced by human activities, has affected the amount of energy flowing inside and outside the planet, imposing a positive *radiative forcing* to the Earth System (IPCC-AR6 2018). Climate system responds to this forcing through different *feedback processes*, which act to amplify or dampen the initial perturbation.

In this framework, General Circulation Models (GCMs) represent the most advanced tools at our disposal to investigate climate evolution. By solving a set of physically based prognostic equations and by simulating the main processes occurring in the Earth system, models provide a description of a fictional planet, which is as similar as possible to the real one.

Therefore, accurate representation by GCMs of the radiative balance of the planet, the so-called Earth Radiation Budget (ERB), and the strength of climate feedbacks is crucial to get reliable historical and future simulations. In this context, the availability of large and continuous amounts of physical data, monitoring the state of the ERB, is essential to reduce the uncertainties of climate projections: observations are the first-order inputs required for GCMs and the unique benchmark for evaluating their performance. In addition, GCMs are regularly tuned by adjusting parameters related to sub-grid processes not explicitly represented in the model, to constrain the simulated energy fluxes to observed values.

This study represents a bridge activity between climate modeling and the use of observational data from a climate perspective. In the first part of the work, simulated and observed *broadband integrated fluxes* have been compared to highlight the main biases present in the representation of the ERB provided by the state-of-the-art GCMs. A specific focus is given to the OLR radiation, which is a key contribution to the ERB and the most sensitive quantity to atmospheric composition.

Furthermore, the OLR fluxes, whose measurements are mainly provided by the Earth Radiation Budget Experiment (ERBE) and the more recent Cloud and Earth Radiant Energy System (CERES) mission, have been monitoring since 1970s, making this quantity an excellent candidate to assess the performance of GCMs.

In this framework, Wild [2020] recently examined the radiative global budget of 40 state-of-the-art global climate models participating in the Coupled Model Intercomparison

Project phase 6 (CMIP6) through a systematic comparison of broadband energy fluxes at surface and TOA with CERES Energy Balanced and Filled (EBAF) dataset. The study has shown an important improvement of the CMIP6 models compared to the earlier model generations, but also a persistent inter-model spread, with a standard deviation of  $2.8 \text{ Wm}^{-2}$  for the all-sky OLR and of  $2.6 \text{ Wm}^{-2}$  for OLR in clear sky conditions.

In this thesis, the analysis of the CMIP6 models biases is extended to a regional scale exploiting the new release of the CERES dataset (EBAF 4.1).

However, although the comparison of observed and simulated OLR broadband fluxes provides fundamental information about the performance of climate models, the detection of model biases is complicated by the spectral integration, which may mask compensation errors in the OLR estimation. Conversely, the long-term comparison between simulated and observed *spectrally resolved radiances* represents a stricter test for the direct verification and improvement of GCMs. In fact, OLR radiances contain the signatures of greenhouse gases, water, and clouds, and monitoring their behavior by comparison to satellite measurements offers an unprecedented opportunity to attribute GCMs biases to a specific portion of the spectrum and, thus, to a specific variable [Kiehl and Trenberth, 1997].

From the mid-2000s, stable hyperspectral observations from satellites of the Earth emission spectrum in the Mid-Infrared (MIR) region ( $667$  to  $2750 \text{ cm}^{-1}$ ) have been provided by different sensors, such as the Atmospheric Infrared Sounding (AIRS, 2002-present) [Le Marshall et al., 2006], the Infrared Atmospheric Sounder Interferometer (IASI, 2006-present) [Clerbaux et al., 2009] and the Cross-track Infrared Sounder (CrIS, 2011-present) [Brindley and Bantges, 2016], opening interesting perspectives for climate applications.

In this context, Whitburn et al. [2021] evaluate linear trends in 10 years (2008 - 2017) of IASI clear-sky spectrally resolved fluxes. In this work, the spectral fingerprints due to the increase of  $\text{CO}_2$  and  $\text{CH}_4$  concentration in the atmosphere are highlighted and quantified. In addition, the effect of temperature variation on radiation at TOA, mainly related to El Niño activity, is assessed in a detailed way.

In the same framework, Susskind et al. [2012] investigate the OLR interannual variability using AIRS data from 2002 to 2011. They find a good agreement between the energy fluxes computed from AIRS spectrally resolved radiances and CERES broadband fluxes and highlight the crucial role of El Niño and La Niña events in the energy fluxes variations at TOA, both over tropical latitudes and on a global scale.

AIRS measurements are also exploited in Huang and Ramaswamy [2009] to detect change in the climate system evolution and to assess the performance of the Geophysical Fluid Dynamics Laboratory coupled atmosphere–ocean–land general circulation model. The study demonstrates how, under climate change, spectrally resolved radiances show more pronounced variations with respect to integrated broadband flux.

Using a similar approach, an existing negative bias in the OLR flux of about  $4 \text{ Wm}^{-2}$  in the AM2 GCM [Team et al., 2004], is investigated by Huang et al. [2006] by comparison of AIRS spectra to simulated radiances, and attributed to a water vapour transport deficiency of the model. In the same way, Huang et al. [2007] highlight the existence of opposite-in-sign biases in water vapour and in  $\text{CO}_2$  spectral bands, which produce fortuitous cancellations of spectral errors in the computation of the total broadband fluxes in the AM2 GCM.

While the aforementioned instruments are able to provide accurate measurements of the entire Mid-Infrared (MIR) portion of the spectrum, generally from  $667$  to  $2500 \text{ cm}^{-1}$

(4 - 15  $\mu\text{m}$ ), the Far-Infrared (FIR) spectral range, from 100 to 667  $\text{cm}^{-1}$  (15 - 100  $\mu\text{m}$ ), which accounts for at least half of the Earth's energy emitted to space [Harries et al., 2008], still lacks of systematic measurements from satellite because of the intrinsic difficulties of development of the proper FIR technology [Palchetti et al., 2020].

Planned for launch in 2027, the Far-Infrared Outgoing Radiation and Monitoring (FORUM) mission will fill this observational gap. FORUM will fly in loose formation with the IASI new generation (IASI-NG) on the Metop-SG-1A satellite [Ridolfi et al., 2020] thus, for the first time from space, the two instruments will cover the whole Earth's emission spectrum, allowing the validation of climate models on the whole range of the OLR.

In anticipation of these measurements, the IASI OLR radiances at TOA are exploited to inspect and evaluate the performance of the EC-Earth climate model. In particular, we describe how the comparison between simulated and observed spectrally resolved clear-sky radiances can provide detailed information on model biases in temperature and humidity at different atmospheric levels. This approach is preferred over the comparison of retrieval products for the following reason: the retrieval of vertical profiles from measured upwelling spectral radiances represents a strongly ill-conditioned inverse problem, therefore a priori profile estimates are always used to constrain the retrieval. The used a priori information causes both global biases and local systematic smoothing errors in the retrieved profiles [Rodgers, 2000], thus making tricky the comparison of climatologies of profiles derived from the model and from the inversion of spectral radiance measurements [Rodgers and Connor, 2003].

In order to simulate upwelling OLR radiances starting from the climate model atmosphere, the fast radiative transfer model (RTM)  $\sigma - IASI$  [Amato et al., 2002] has been implemented in the CFMIP Observation Simulator Package (COSP v.1.4.1) inside the EC-Earth GCM. On-line historical simulations with prescribed sea surface temperatures (SSTs) and sea ice concentration (SIC) have been performed using COSP +  $\sigma - IASI$  in clear-sky conditions, in the MIR and FIR spectral regions, over the period 2008 - 2016, compatible with IASI available observations.

*Chapter 1* recalls the basic radiometric definitions and the fundamentals of radiative transfer theory, the different components involved in the Earth Radiation Budget and principles of climate modeling, with a specific focus on the main approximations implemented in the radiative transfer calculations in GCMs. In *chapter 2*, the performances of a set of state-of-the-art climate models participating to the Coupled Model Intercomparison Project - Phase 6 (CMIP6) are assessed through a systematic comparison between simulated and observed integrated energy fluxes, provided by CERES dataset. In *chapter 3*, the  $\sigma - IASI$  Radiative Transfer Model is used to reconstruct synthetic spectrally resolved radiances, that are then compared to observed spectra measured during the Teresina campaign (2005).

The bulk of the thesis work is presented in *chapter 4*, which contains a detailed description of the implementation of the  $\sigma - IASI$  RTM in the EC-Earth climate model. The modified model is then used to simulate a clear-sky radiance climatology, which is compared to IASI observations to identify climate model biases.

The future perspectives are described in *chapter 5* and then we draw the conclusions.



# 1

## Background

In this section, we briefly recall the basic radiometric definitions used in the study and fundamentals of radiative transfer theory. We then provide a description of the present-day ERB on the basis of CERES measurements, with a particular focus on the Outgoing Longwave Radiation. Finally, we introduce some fundamentals of climate modelling, including state-of-the-art GCMs, and focus on the main approximations adopted in the model physics and radiative transfer calculations.

### 1.1 Radiative transfer theory

#### 1.1.1 Radiance and spectral flux

First of all, the spectral radiance is defined as the energy flowing through a unit area, per unit time, per unit wavenumber and solid angle. The radiance emitted by a black body is described by the Planck law as a function of the wavenumber  $\nu$ , or, equivalently, as a function of wavelength  $\lambda$ :

$$B_\nu = \frac{2h\nu^3c^2}{e^{\frac{h\nu}{kT}} - 1} \quad \text{or} \quad B_\lambda = \frac{2hc^2}{e^{\frac{hc}{\lambda kT}} - 1} \quad (1.1)$$

where  $h = 6.62 \cdot 10^{-34} Js$  is the Planck constant,  $c = 2.99 \cdot 10^8 \frac{m}{s}$  is the speed of light,  $k = 1.31 \cdot 10^{-23} \frac{J}{K}$  the Boltzmann constant and  $T$  the temperature of the emitting body.

The spectral radiance  $L_\nu$  emitted by a body of uniform temperature  $T$  at wavenumber  $\nu$  is described by the product of the black-body radiance  $B$  and the emissivity  $\epsilon$ :

$$L_\nu = B_\nu \epsilon_\nu \quad (1.2)$$

The radiation emitted by a black-body can be converted into another useful quantity, called Brightness Temperature (BT). Specifically, BT is defined as the temperature of the body emitting the radiance  $L_\nu$  at the wavenumber  $\nu$ .

By inverting 1.1:

$$T_\nu = \frac{hc\nu}{k \ln\left(1 + \frac{2hc^2\nu^3}{L_\nu}\right)}. \quad (1.3)$$

From the spectral radiance, it is possible to compute the spectral flux  $F_\nu$ , defined as the integral of the radiance over a hemisphere of solid angle:

$$F_\nu = \int_{\Omega} L_\nu(\theta, \phi) \cos(\theta) d\Omega \quad (1.4)$$

where  $d\Omega$  is the infinitesimal element of the solid angle  $\Omega$ , the hemispheric domain of integration. In spherical coordinates, it is represented as  $d\Omega = \sin(\theta)d\theta d\phi$ , where  $\theta$  is the zenith angle and  $\phi$  the azimuth angle:

$$F_\nu = \int_0^{2\pi} d\phi \int_0^{\pi/2} d\theta L_\nu(\theta, \phi) \cos(\theta) \sin(\theta) \quad (1.5)$$

As a consequence, if the radiance field is isotropic, the spectral flux can be simply obtained by the following expression:

$$F_\nu = \pi L_\nu \quad (1.6)$$

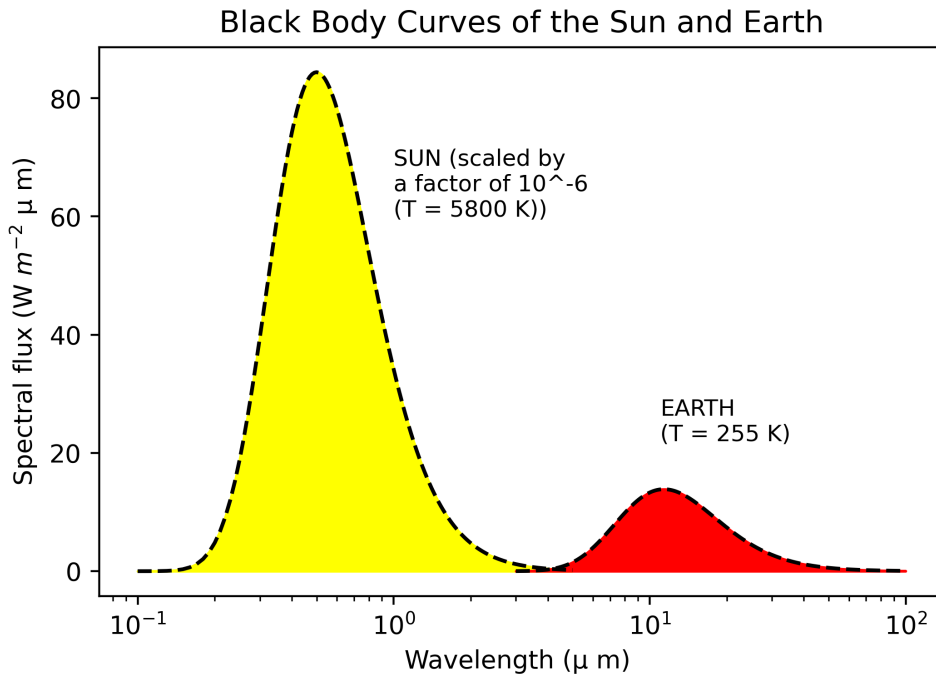


Figure 1.1: Blackbody emission spectra for the Sun (temperature 5800 K) and Earth (temperature 255 K, as seen from space) as function of wavelength.

As shown by the spectral flux depicted in Figure 1.1, most of the solar energy is confined in the spectral range between 0.2 and 4  $\mu\text{m}$  and is termed short-wave (SW) radiation, including near-infrared, visible and ultra-violet spectral ranges. Conversely, Earth emitted energy falls between approximately 3 and 100  $\mu\text{m}$  (from about 100 to

3000  $\text{cm}^{-1}$ ) and is known as Long-Wave (LW) radiation (Far-Infrared and Mid-Infrared spectral ranges).

The total flux can be obtained by integrating the spectral flux  $F_\nu$  over frequency  $\nu$ .

$$F = \int_{\nu_1}^{\nu_2} F_\nu d\nu \quad (1.7)$$

Under the assumption of isotropic radiation, the total flux of a black body computed over the spectral range from 0 to  $\infty$  is equal to:

$$F = \sigma T^4 \quad (1.8)$$

where  $\sigma = 5.67010 \cdot 10^{-8} \text{Wm}^{-2}\text{K}^{-4}$ . The formula, known as Stefan-Boltzmann law, demonstrates that the energy per unit time and unit area emitted by a black body depends on the fourth power of the temperature.

### 1.1.2 Radiative transfer equation

A beam of radiation (radiance  $L_\nu$ ) interacting with a medium experiences the processes of absorption, emission and scattering.

In the absence of scattering and emission, the pencil of radiation is reduced on the basis of the Lambert's law:

$$\frac{dL_\nu}{L_\nu} = -\rho k_{a,\lambda} ds \quad (1.9)$$

where  $\rho$  is the density of the medium,  $s$  is the distance traveled by the wave and  $k_{a,\lambda}$  is the absorption cross section, which has units of area/mass. Equation 1.9 can also be expressed replacing the product  $\rho k_{a,\lambda}$  with  $n \tilde{k}_{a,\lambda}$ , where  $n$  is the number of particles present in the medium and  $\tilde{k}_{a,\lambda}$  now represents the absorbing area of a single particle interacting with the radiation.

By integrating the Lambert's law along the path of radiation, we obtain the following:

$$L_\nu(s) = L_\nu(0) \exp\left(-\int_0^s \rho k_{a,\lambda} ds'\right) \quad (1.10)$$

Thus, the radiance decreases exponentially with the optical path  $\int_0^s \rho k_{a,\lambda} ds'$ , that is the distance traveled by the radiation weighted by the density and absorption cross section of the medium.

A useful quantity is the transmissivity, which is defined as the ratio between the incident beam of radiation and the radiation intensity at distance  $s$ :

$$\tau_\nu = \frac{L_\nu(s)}{L_\nu(0)} = \exp\left(-\int_0^s \rho k_{a,\lambda} ds'\right) \quad (1.11)$$

In order to maintain thermal equilibrium, the substance absorbing radiant energy must also emit it. In the previous section, by introducing the basic radiometric quantities, we have already introduced the spectral emissivity (see Eq. 1.2).

In Local Thermodynamic Equilibrium (LTE) condition a substance emits radiation as efficiently as it absorbs it. This statement derives from Kirchhoff's law, which expresses:

$$a_\nu = \epsilon_\nu \quad (1.12)$$

where  $a_\nu$  is the absorptivity.

The LTE condition is verified when energy transitions are controlled by molecular collisions and it generally occurs in the troposphere and stratosphere, at altitudes below 60 km.

Based on 1.2 and Kirchhoff's law, the following equation can be derived:

$$\frac{dL_\nu}{B_\nu(T)} = d\epsilon_\nu = da_\nu \quad (1.13)$$

Thus, from Lambert's law, we obtain:

$$dL_\nu = \rho k_{a,\lambda} J_\nu(T) ds \quad (1.14)$$

where  $J_\nu = B_\nu(T)$  is the source function in absence of scattering in LTE conditions.

Therefore, if a beam of radiation is confined in a small solid angle  $\Delta\Omega$  and experiences both absorption and emission processes, its variation is written as:

$$dL_\nu = -\rho k_{a,\lambda} L_\nu ds + \rho k_{a,\lambda} J_\nu(T) ds \quad (1.15)$$

The process of emission is isotropic, but the equation of radiative transfer 1.15 is derived in the case of absorption and emission along the single direction  $\vec{n}$ . We do not address in this section the study of the scattering processes that would require a more complex treatment, involving the angular dependence of the radiation field. However, if we continue to refer to a single direction, the scattering process can be embedded in equation 1.15 by considering a new cross section, defined as an extinction cross section, obtained by the sum of absorption and scattering cross sections:

$$k_{e,v} = k_{a,v} + k_{s,v}, \quad (1.16)$$

The solution of equation 1.15 is:

$$L_\nu(S) = L_\nu(0)e^{-\int_0^S \rho k_{e,v} ds} + \int_0^S \rho k_{e,v} B_\nu e^{-\int_s^S \rho k_{e,v} ds'} ds \quad (1.17)$$

that is known as Schwarzschild's equation. The first term describes the exponential decrease of the incident beam of radiation, while the second term represents the emission of each layer  $ds$  and how it is attenuated by the successive layers (between  $s$  and  $S$ ). The same equation can be written in a more synthetic way through the transmissivity term:

$$L_\nu(S) = L_\nu(0)\tau(0, S) + \int_0^S \rho k_{e,v} B_\nu \tau(s, S) ds \quad (1.18)$$

## 1.2 The Earth Radiation Budget

Earth Radiation Budget drives the evolution of the Earth's climate. At TOA, Earth gains energy from the solar radiation, which is partly reflected back to space, while it loses energy through the Outgoing Longwave Radiation, the infrared energy emitted by the planet. The balance between the absorbed solar energy (ASR) and the OLR determines the thermal equilibrium of the planet.

The first estimation of the ERB was performed in 1917 by Dines [1917], using balloon measurements. It was followed by several attempts, whose results were however unreliable

and strongly affected by the assumptions made in the calculations. For example, until the early 1970s, the planetary albedo, defined as the fraction of the solar radiation energy reflected back by the surface, was supposed to be between 40 % and 50% [Kiehl and Trenberth, 1997]. Only when the data provided by space-borne instruments were available, starting with Nimbus 6 in 1975 [Dewitte and Clerbaux, 2017], the assumptions were replaced by measurements and the planetary albedo was estimated to be approximately equal to 30%.

From the mid 1980s, the Earth Radiation Budget Experiment (ERBE) [Barkstrom, 1984] and then, from 2000s, the CERES mission [Loeb et al., 2018], have been continuously collecting measurements of the Earth energy fluxes at TOA, becoming the fundamental reference point for monitoring the evolution of the ERB.

In Figure 1.2, the present-day ERB is represented on the basis of CERES Energy Balanced and Filled (EBAF) observations, covering the period 2005-2015. Here, the SW (yellow arrows) and LW (red arrows) components are illustrated together with their mean values and uncertainties.

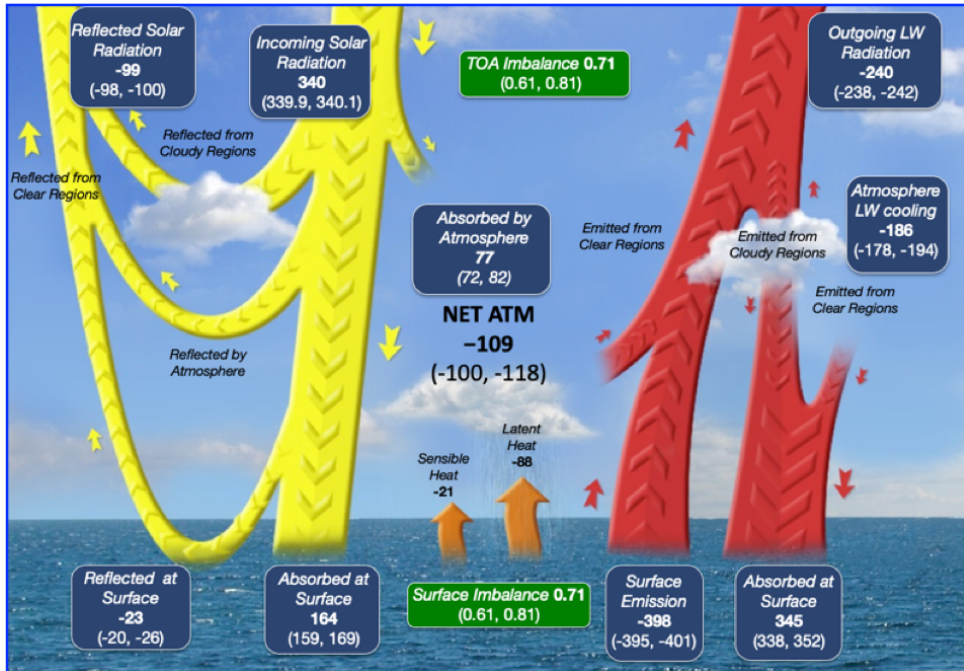


Figure 1.2: Earth global mean energy budget for July 2005-June 2015 (CERES dataset <https://ceres.larc.nasa.gov/science/>).

We can easily estimate the SW radiation flux of the Sun, starting from Figure 1.1. Here, the yellow area under the black-body curve, corresponding to the black-body flux of Eq. 1.8, describes the energy per unit time and area emitted by the Sun and it is equal to  $63 \cdot 10^6 \text{ Wm}^{-2}$ . Considering the surface of the Sun ( $6 \cdot 10^{12} \text{ km}^2$ ), the total energy emitted by the Sun is about  $3.8 \cdot 10^{26} \text{ W}$ .

The solar radiation arriving on a surface normal to the direction of light propagation and located at the mean distance Sun-Earth ( $1.5 \cdot 10^8 \text{ km}$ ) is about  $1370 \text{ Wm}^{-2}$  and is commonly known as *solar constant*. This amount of energy intercepts the surface of a circle of area  $\pi r_p^2$ , where  $r_p$  is the radius of the Earth and is then distributed over the entire surface of the planet, which is four times greater ( $4\pi r_p^2$ ). As a result, incident solar radiation can be approximated by one-fourth of the solar constant ( $\sim 340 \text{ Wm}^{-2}$ ).

Of this energy, a total of  $\sim -99 \text{ Wm}^{-2}$  is reflected back to space by the surface ( $\sim 23 \text{ Wm}^{-2}$ ), atmosphere and clouds ( $\sim -66 \text{ Wm}^{-2}$ ). Consequently, the ASR at the Earth's surface is approximately  $164 \text{ Wm}^{-2}$ .

On a global scale, the surface emits much more ( $\sim 398 \text{ Wm}^{-2}$ ) than the ASR because the ground also gains energy from the LW radiation emitted downward by the atmosphere. The surface loses its surplus of energy also by transferring sensible and latent heat to the atmosphere.

At TOA, the OLR flux is equal to  $\sim 240 \text{ Wm}^{-2}$  and can be approximated with the integral of the spectral flux (equation 1.5) in Figure 1.1, between 3 and  $100 \mu\text{m}$  (100 to about  $3000 \text{ cm}^{-1}$  in wavenumber).

### 1.2.1 The Earth emission spectrum

The OLR measured at TOA comes from the small portion of energy emitted by the surface, which freely passes through the atmosphere, and by the radiative cooling of the atmosphere and clouds. The interaction of infrared radiation emitted by the Earth with optically active gases, such as water vapour, carbon dioxide, methane and ozone, produces several absorption lines due to the vibrational and rotational transitions of these molecules (Section 1.1.2).

In Figure 1.3, a simulated OLR spectrum is shown under all-sky (blue curve) and clear-sky (black curve) conditions, distinguishing the Far-Infrared (FIR) and Mid-Infrared (MIR) spectral regions. The dashed lines show the equivalent blackbody emission at typical surface (295 K) and tropopause (210 K) temperatures. The main gas absorption bands are indicated.

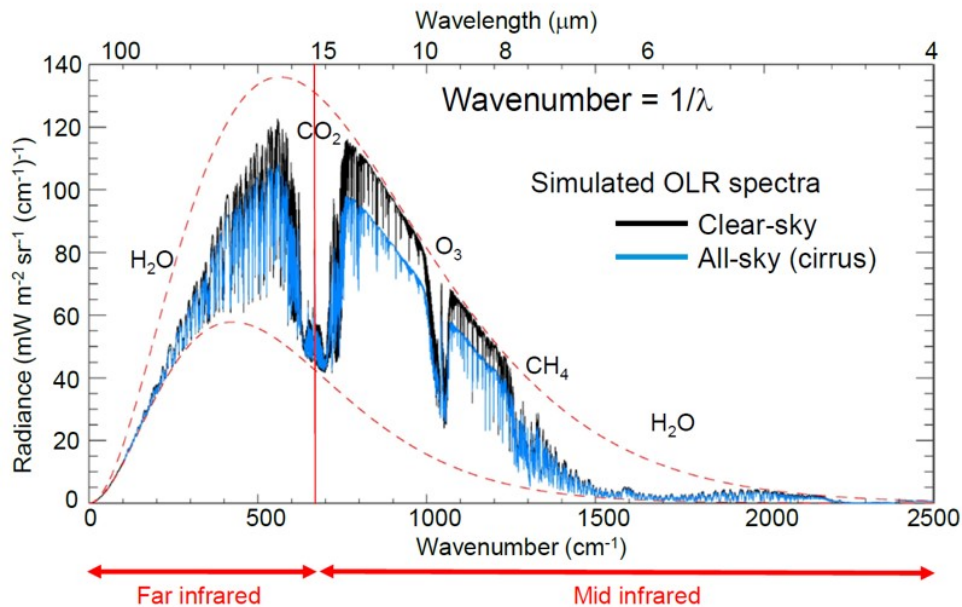


Figure 1.3: Simulated Earth emission spectrum.

Spectrally resolved radiances have been measured for the first time from space in the 1970s [Brindley and Bantges, 2016], but only starting from the 2000s stable hyperspectral observations of the MIR spectral range became available, with the key satellite missions

of the Atmospheric InfraRed Sounder (AIRS, 2002-present) [Le Marshall et al., 2006], the Infrared Atmospheric Sounding Interferometer (IASI, 2006-present) [Clerbaux et al., 2009] and the Cross-track Infrared Sounder (CrIS, 2011-present) [Bloom, 2001].

A more accurate description of the IASI mission together with a thorough analysis of the Earth emission spectrum and its sensitivity to temperature and gas concentrations, will be provided in Chapter 4.

### 1.2.2 Energy Imbalance at TOA

The Earth Energy Imbalance (EEI) represents one of the most important metrics for defining the status of global climate change. EEI derives from the difference between the net incoming solar radiation and the emitted OLR at TOA. Therefore, a positive (negative) EEI value indicates that the planet is accumulating (losing) energy: consequently, the Earth's system will warm (cool) until a new energy balance is restored.

From several decades, observational data have confirmed that the climate system is out of balance. In this framework, Von Schuckmann et al. [2020] provided an accurate estimate of the heat gain in the ocean, atmosphere, cryosphere and land on the basis of in situ data, multi-satellite data, atmospheric reanalysis, radiosonde records and microwave sounding techniques and during the period 1971-2018 a long-term increase in EEI is found, corresponding to a total heat gain of  $0.47 \pm 0.10 \text{ Wm}^{-2}$ .

One of the major difficulty of estimating EEI derives from the multiple internal and external factors acting on the ERB over different time and space scales. For example, internal natural forcings, such as El Niño, La Niña, or weather systems, occur from monthly/annual timescales to several decades. In a similar way, external forcing represented by volcanic eruptions or changes in solar radiation can affect the energy imbalance at TOA. However, among external factors, in recent decades, EEI has become increasingly dominated by human activities (IPCC-AR6, 2018) through the growth of greenhouse gas concentrations in the atmosphere, which causes a dramatic accumulation of energy in the system [Hansen et al., 2011]. Most of this excess energy is stored in the oceans (93%), while the remaining portion warms the surface and the atmosphere [Meysignac et al., 2019].

Since the ocean is the key energy storage for EEI, the energy accumulated therein is constantly monitored through the Global Ocean Observing System (GOOS). From the most recent measurements, the increase of the global Ocean Heat Content (OHC) is found to be in the range between  $0.1$  and  $0.9 \text{ Wm}^{-2}$  [Von Schuckmann et al., 2016].

On the basis of CERES data, obtained between 2005 and 2015, the magnitude of the EEI is equal to about  $0.7 \text{ Wm}^{-2}$  (see Figure 1.2). However, this estimation is still very challenging and the energy fluxes involved in the computation of the EEI are affected by errors (calibration and conversion of radiances to fluxes) that are of the same order of magnitude of the EEI expected value [Loeb et al., 2018, 2009].

For this reason, the availability of long-term measurements of radiative fluxes from space, combined with the ground observing system, are essential to reduce the uncertainty in EEI and it is fundamental to investigate the actual roles of the different forcings on climate evolution.

## 1.3 Climate models

Numerical climate models provide a physically based estimation of the past and future climate and allow to investigate the response of climate system to different forcings over long time scales.

### 1.3.1 Energy Balance Model

The simplest type of model is represented by *Energy Balance Model* (EBM), which belongs to the first generation of models and is exclusively based on the energy conservation equation.

By simply describing the energy conservation equation for a single atmospheric layer, we can write:

$$4\pi R^2 h \rho c \frac{dT}{dt} = \pi R^2 (1 - \alpha) S_0 - 4\pi R^2 \epsilon k T^4 \quad (1.19)$$

where  $h$  is the vertical extent of the layer,  $\rho$  the density of the air,  $c$  the specific heat of the air,  $T$  the global temperature,  $\alpha$  the planetary albedo,  $S_0$  the solar constant,  $\epsilon$  the emissivity of the planet, and  $k$  the Stefan-Boltzmann constant.

As discussed in the previous section, the global heat uptake of the atmosphere (left term of the equation) is modulated by the incoming solar energy (first term on the right) and the energy emitted by the Earth, here in a simplified form (second term on the right).

When the equilibrium is reached, the first term is equal to zero and the average global temperature is:

$$T = \left( \frac{(1 - \alpha) S_0}{4\epsilon\alpha} \right)^{\frac{1}{4}} \quad (1.20)$$

The resulting equilibrium temperature depends directly on the emissivity and the planetary albedo.

More reliable EBMs take into account two (or more) energy conservation equations for the planet surface and for the atmospheric layers. EBMs can also be one- or two-dimensional, by considering meridional and zonally energy flows or both of them.

### 1.3.2 General Circulation Model

Full-physics models, known as *General Circulation Models* (GCMs), explicitly resolve the dynamics of the atmosphere on a three-dimensional grid and provide a representation of all relevant thermodynamic and physical processes in the system.

Since the 1940s, with the advent of digital computers, the first GCMs were developed, initially as numerical weather prediction (NWP) models, for forecast limited over time and space, and later as climate models, extending the forecast to global scale and to longer time scales [Edwards, 2011].

## The Dynamical Core

All GCMs are characterized by a "dynamical core" capable of simulating the evolution of the atmospheric flow using primitive equations integrated over a three-dimensional grid (Figure 1.4).

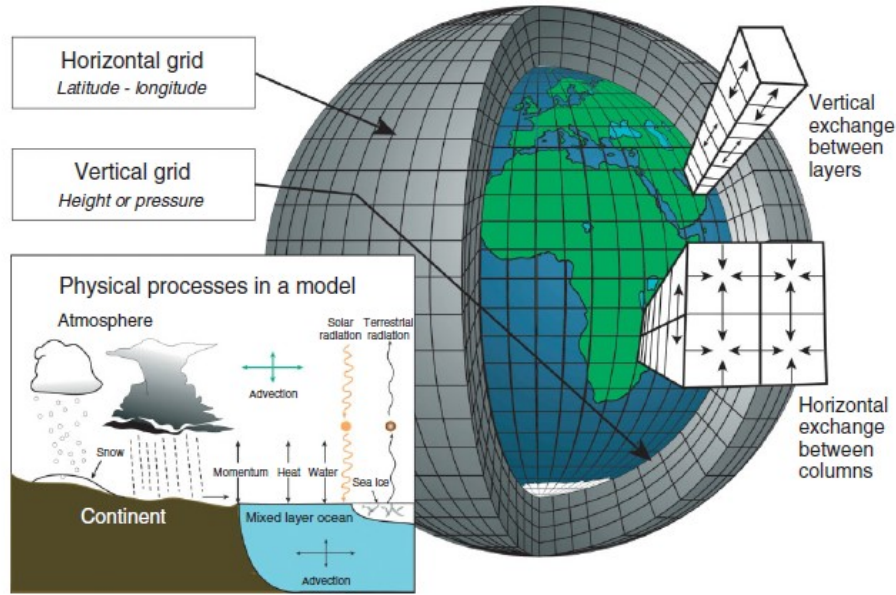


Figure 1.4: Example of the grid structure of a General Circulation Model. Figure from Edwards [2011]

The continuous equations integrated in the model are expressed in the coordinates  $(\lambda, \theta, \sigma)$  where  $\lambda$  is the longitude,  $\theta$  is the latitude and  $\sigma$  the vertical coordinate. In most models, the vertical coordinate is not expressed as function of pressure or height but it is described by a hybrid *terrain following* coordinate, depending on the surface pressure and constrained by the following conditions:

$$\sigma(0, p_s) = 0 \quad \text{and} \quad \sigma(p_s, p_s) = 1 \quad (1.21)$$

In this coordinate system, the primitive equations are as follows:

- Momentum equations:

$$\begin{aligned} \frac{\partial U}{\partial t} + \frac{1}{r_p \cos^2 \theta} \left( U \frac{\partial U}{\partial \lambda} + V \cos \theta \frac{\partial U}{\partial \theta} \right) + \frac{d\sigma}{dt} \frac{\partial U}{\partial \sigma} - fV + \\ + \frac{1}{r_p} \left( \frac{\partial \phi}{\partial \lambda} + R_d T_v \frac{\partial (\ln p)}{\partial \lambda} \right) = P_u + K_u \end{aligned} \quad (1.22)$$

$$\begin{aligned} \frac{\partial V}{\partial t} + \frac{1}{r_p \cos^2 \theta} \left[ U \frac{\partial V}{\partial \lambda} + V \cos \theta \frac{\partial V}{\partial \theta} + \sin \theta (U^2 + V^2) \right] + - \frac{d\sigma}{dt} \frac{\partial V}{\partial \sigma} + fU + \\ \frac{\cos \theta}{r_p} \left( \frac{\partial \phi}{\partial \theta} + R_d T_v \frac{\partial (\ln p)}{\partial \theta} \right) = P_v + K_v \end{aligned} \quad (1.23)$$

where  $r_p$  is the radius of the Earth,  $\phi$  is the geopotential,  $R_d$  is the gas constant for dry air,  $T_v$  the virtual temperature defined as:

$$T_v = T + [1 + (\frac{R_v}{R_d} - 1)q] \quad (1.24)$$

where  $q$  is the specific humidity and  $R_v$  the gas constant of water vapour. Finally,  $P_u$  and  $P_v$  describe the parametrized physical processes, while  $K_u$  and  $K_v$  are the horizontal diffusion terms.

- Thermodynamic equation:

$$\frac{\partial T}{\partial t} + \frac{1r_p}{\cos^2\theta} \left[ U \frac{\partial T}{\partial \lambda} + V \cos\theta \frac{\partial T}{\partial \theta} \right] + \frac{d\sigma}{dt} \frac{dT}{d\sigma} - \frac{kT_v\omega}{(1 + (\delta - 1)q)p} = P_T + K_T \quad (1.25)$$

where  $k$  is  $\frac{R_d}{cp_{dry}}$  with  $cp_{dry}$  the specific heat of dry air at constant pressure,  $\omega$  is the vertical velocity expressed as  $(\frac{dp}{dt})$  and  $\delta$  is  $\frac{cp_{vap}}{cp_{dry}}$  with  $cp_{vap}$  the specific heat of water vapour at constant pressure.

- Moisture equation:

$$\frac{\partial q}{\partial t} + \frac{1}{r_p \cos^2\theta} \left[ U \frac{\partial q}{\partial \lambda} + V \cos\theta \frac{\partial q}{\partial \theta} \right] + \frac{d\sigma}{dt} \frac{dq}{d\sigma} = P_q + K_q \quad (1.26)$$

- Continuity equation:

$$\frac{\partial}{\partial t} \left( \frac{\partial p}{\partial \sigma} \right) + \nabla \left( \vec{v}_h \frac{\partial p}{\partial \sigma} \right) + \frac{\partial}{\partial \sigma} \left( \frac{d\sigma}{dt} \frac{\partial p}{\partial \sigma} \right) = 0 \quad (1.27)$$

where  $\nabla$  is the horizontal gradient operator in spherical coordinates and  $\vec{v}_h = (u, v)$  is the horizontal wind.

These equations are discretized over the grid cells of the model (Figure 1.4) and numerically solved to provide the main prognostic variables, such as wind components, temperature, specific humidity, cloud cover and ice/liquid content.

From the 1980s, climate models moved in the direction of increasingly comprehensive models. In the so-called *coupled atmosphere-ocean general circulation models* (AOGCMs), the atmospheric and ocean components - each one represented by a GCM - are put into communication and at fixed time steps, momentum, heat and water fluxes are exchanged. Global ocean models in AOGCMs also contain a representation of the sea-ice in polar regions.

Finally, *Earth System Models* (ESMs) also include other processes/components of the climate system, for example biogeochemical cycles (carbon cycle, sulfur cycle, or ozone), land ice, dynamic vegetation and interactive chemistry, representing the most comprehensive tools available today to simulate the past and future response of the climate system.

### Model Physics and Parametrizations

In addition to the "dynamical core", all the other relevant physical processes (radiative transfer, cloud formation and precipitation, ..) and all dynamical processes involving scales smaller than the model grid (convection, turbulence, orographic drag, etc.) are represented by the so-called "model physics". In fact, even if these processes are dynamical in nature, they are not explicitly resolved in the model through the primitive equations, and their effects have to be formulated in terms of the resolved grid-scale variables through physical parametrizations.

Here, we briefly introduce the main physical processes simulated in the Integrated Forecast System (IFS) model of the European Centre for Medium-Range Weather Forecasts (ECMWF), which is the atmospheric component of the EC-Earth climate model used in this work.

Starting from the prognostic variables provided by the model, the radiative transfer scheme is generally the first process to be simulated. The way the radiative computation is solved in climate models will be further described in the following section.

Orography strongly affects the air flow in the lowest atmospheric layers and at the standard model resolution (today of the order of tens to hundreds of kilometers for climate models) many details of the orographic features cannot be directly described [Pithan et al., 2016]. The impact of the sub-grid orographic drag on the atmospheric dynamics is then represented by the parametrization introduced by Lott and Miller [1997]. The orography drag is also strictly related to the representation of the turbulent processes at the surface and, for this reason, the scheme that simulates the transfer of heat, momentum and moisture between the surface and the lowest atmospheric levels is generally called by the climate model right after the orographic drag scheme.

As shown in Figure 1.5, other fundamental processes contained in the "model physics" of GCMs involve cloud, precipitation and convection. The prognostic scheme used for simulating stratiform and convective clouds is described in Tiedtke [1993]. The same scheme also takes into account several important cloud processes like cloud-top entrainment, precipitation of water and ice and evaporation of precipitation.

A distinction is made between the deep, mid-level and shallow convection: the deep convection is directly related to the instability of the air column and it is modulated by the Convective Available Potential Energy (CAPE), while the mid-level convection depends on large-scale vertical velocity and the shallow convection is mainly controlled by sub-cloud layer turbulence [LeMone and Pennell, 1976].

### 1.3.3 Radiative Computation in Climate Models

In this section, we present a brief description of the Rapid Radiative Transfer Model (RRTM), that is implemented in most of the models presented in the following chapter, including EC-Earth. RRTM can provide accurate simulations of energy fluxes in the LW spectral interval, which is the region where we will focus our analysis.

Solving the radiative transfer equation to calculate the energy fluxes is computationally expensive. As a consequence, the spatial grid used for radiative calculations in climate models is generally coarser than the actual model resolution and the full radiation scheme is called at lower temporal frequency.

One of the existing strategies used to limit the computational cost in climate models is based on the correlated-k distribution method, an approximate and fast procedure

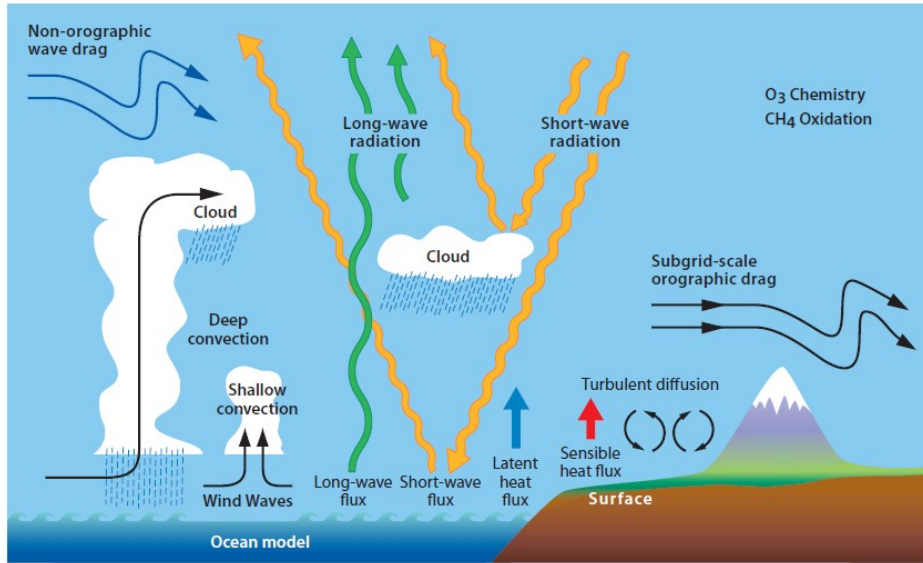


Figure 1.5: Scheme of the physical processes simulated in the "model physics" of General Circulation Models (from IFS documentation)

that can provide the fluxes and cooling rate of the atmosphere [Mlawer et al., 1997]. The results obtained with this approximation have been widely validated [Hogan and Matricardi, 2020] against the more accurate outputs obtained by line-by-line radiative transfer models, whose usage in climate models remains prohibitive.

The correlated-k distribution method consists in dividing the spectrum into a number of bands and then reordering the gaseous absorption coefficients  $k$  (see paragraph 1.1.2) within each band based on their amplitude.

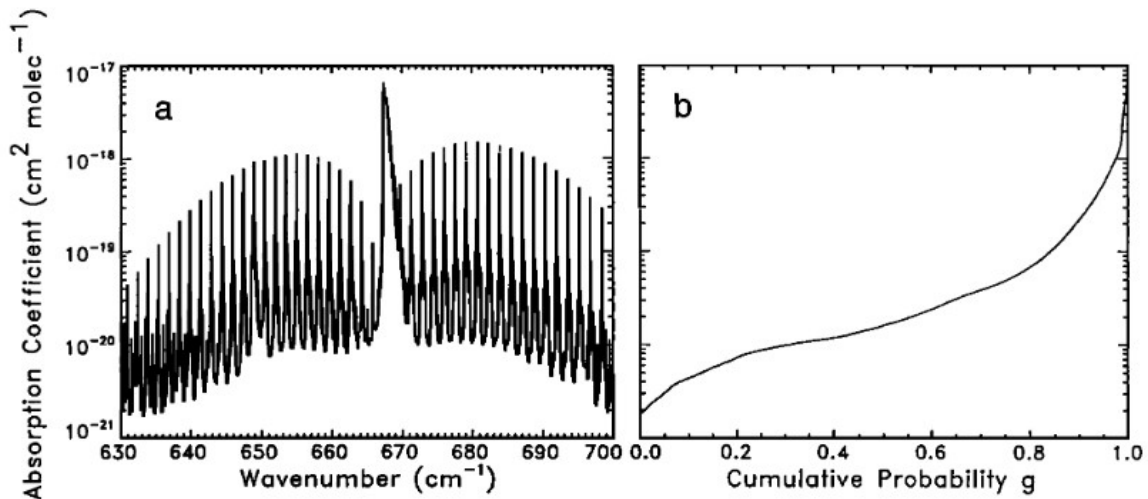


Figure 1.6: Absorption coefficients due to carbon dioxide for a single layer (Pressure = 507 mbar) over the spectral range 630 – 700 $\text{cm}^{-1}$  -a) absorption coefficients as function of the wavenumber; b) rearranged in ascending order. Figure from Mlawer et al. [1997]

Panel A of Figure 1.6 shows the carbon dioxide absorption coefficient  $k(\nu)$  as a function of the wavenumber from 630 to 700  $\text{cm}^{-1}$ . By mapping the  $k(\nu)$  to the  $g$ -space, where

$g(k)$  is the cumulative distribution function, or the fraction of the absorption coefficients smaller than  $k$ , we obtain the curve illustrated in panel B.

While a line-by-line model solves the radiative transfer equation for each spectral line, the correlated- $k$  distribution (CKD) method works with this smoothly increasing  $g(k)$  function, which is equivalent to solving the radiative transfer equation for monochromatic radiation [Hogan and Matricardi, 2020].

Starting from the averaged radiance  $R$  over the interval  $[\nu_1, \nu_2]$ , we can write:

$$R = \frac{1}{\nu_2 - \nu_1} \int_{\nu_1}^{\nu_2} d\nu \left\{ R_0(\nu) + \int_{t_\nu}^1 [B(\nu, T(t'_\nu)) - R_0(\nu)] dt'_\nu \right\} \quad (1.28)$$

where  $R_0$  is the incoming radiance to the layer taken into account,  $B(\nu, T)$  is the Planck function at wavenumber  $\nu$  and temperature  $T$  while  $t_\nu$  is the transmittance for the layer optical path, and  $t'_\nu$  is the transmittance at a specific point of the optical path in the layer.

By rearranging the absorption coefficients in ascending order, we obtain the monotonic function  $k(g)$  represented in panel B of Figure 1.6. Thus, mapping  $\nu$  to  $g$ , the previous equation becomes:

$$R = \int_0^1 dg \left\{ B(g, T_g) + [R_0(g) - B(g, T_g)] \exp[-k(g, P, T) \frac{\rho \Delta z}{\cos \phi}] \right\} \quad (1.29)$$

The dependence of the transmittance is now written in terms of the absorption coefficient  $k(g, P, T)$ , characterized by a pressure  $P$  and a temperature  $T$ , a density  $\rho$ , a vertical thickness of the layer  $\Delta z$ , and the angle  $\phi$  of the optical path.

For a given spectral interval, such as that represented in panel A of figure 1.6, the domain of the variable  $g$  is then divided into a number of sub-intervals (called  $g$ -points) on the basis of the shape of the  $k(g)$  function. Then, for each sub-interval, a single representative value of  $k$  ( $k_{sel}$ ) is chosen.

Now, for each  $k_{sel}$  the outgoing radiance can be computed as:

$$R_{sel} = [B + (R_0 - B) \exp(-k_{sel} \frac{\rho \Delta z}{\cos \phi})] \quad (1.30)$$

The average radiance over all the spectral range corresponds to the sum of the radiance  $R_j$  computed over the  $n$  sub-intervals or  $g$ -points.

$$R_j = \sum_j W_j [B + (R_0 - B) \exp(-k_j \frac{\rho \Delta z}{\cos \phi})] \quad (1.31)$$

where  $W_j$  is the size of the sub-intervals with  $\sum_j W_j = 1$ .

### Radiative Computation in presence of clouds

As discussed in the previous paragraph, climate models are able to provide broadband integrated fluxes through approximated methods, which are extremely faster than the

calculations performed by line-by-line radiative transfer models. Another complication arises when the radiative equation is solved in presence of clouds. The resolution of the climate models, generally in the order of tens to hundred of kilometers, is not adequate to correctly represent the sub-grid scale structure of the clouds.

Indeed, the model is only able to provide the profile of cloud cover, ice and liquid water content representative of the whole grid cell. In addition, clouds are homogeneous within the cloudy portion of the cell. To take into account the vertical and horizontal clouds heterogeneity in a single cell, the radiative computation is performed by introducing assumptions on how sub-grid clouds overlap [Zhang and Jing, 2016].

The most used overlap schemes, shown in Figure 1.7, are listed below:

- the Maximum Overlap assumes clouds at different levels with the maximum overlap. The total cloud fraction corresponds to the largest single-layer cloud cover;
- the random overlap assumes that clouds are randomly overlapped;
- the Maximum-Random Overlap is based on both the previous schemes. When two clouds are adjacent, clouds are maximum overlapped, while, when there is a gap between two cloud layers, clouds are randomly overlapped.

Many climate models implement the maximum-random overlap scheme, even if a more realistic assumption is represented by the exponential-random overlap [Hogan and Illingworth, 2000].

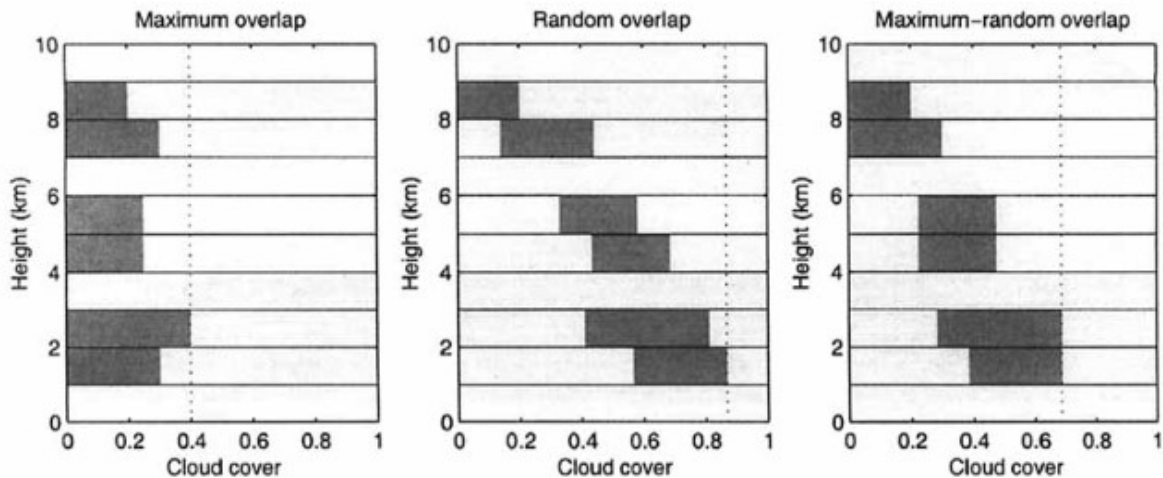


Figure 1.7: Most used overlap assumptions in climate models. Figure from Hogan and Illingworth [2000]

A more flexible technique to compute domain-average radiative fluxes was proposed and validated by Pincus et al. [2003] and it is known as the Monte Carlo Independent Column Approximation (McICA).

This scheme is based on the division of the large spatial domain, represented by the grid cell of the model, into a number  $N$  of sub-columns. In each layer of the sub-column, the cloud fraction can be only 0 or 1 and the ice and water content is constant. The sub-columns are stochastically generated by a cloud generator algorithm, following one of the overlap assumptions described above, and its ensemble reproduce the probability

distribution function corresponding to the cloud profiles of the model grid cell [Räisänen et al., 2004].

In principle, when the sub-columns are generated, the total flux should be computed by the sum of the fluxes obtained in each sub-column:

$$F_{tot} = \frac{1}{N} \sum_{n=1}^N F_n \quad (1.32)$$

Given the number  $K$  of spectral intervals (g-points of Section 1.3.3) where the flux is computed, the same expression can be written as:

$$F_{tot} = \frac{1}{N} \sum_{n=1}^N \sum_{k=1}^K w_k F_{n,k} \quad (1.33)$$

where  $w_k$  is a spectral weight corresponding to  $k$ -th spectral interval.

Because the computation cost of the double sum of 1.33 is too expensive for a climate model, McICA adopts the following approximation, simplifying the equation in:

$$F_{McICA} \approx \sum_{k=1}^K F_{n_k,k} \quad (1.34)$$

where  $F_{n_k,k}$  is the monochromatic flux computed for a single randomly selected sub-column  $n_k$ . Consequently, the computational cost of 1.34 is the same as a full spectral integration on a single subcolumn. Since the McICA method uses randomly selected sub-columns in the computation of the fluxes, a random error is associated to the estimation. However, the impact of McICA noise has been already addressed and in different models was found to be negligible [Barker et al., 2008].

As mentioned, this approximation is implemented in the radiative scheme of climate models, such as RRTM, together with a cloud generator based on specific cloud overlap rules.

### 1.3.4 Matching the observations: the tuning technique

As discussed above, the sub-grid processes, involving turbulent, convective dynamics and clouds, have to be parameterized in climate models. These parameterizations affect the radiation, thermodynamics, dynamics, etc., of the model and rely on a set of parameters which sometimes are poorly constrained by observations [Hourdin et al., 2017]. The process of "model tuning" consists in adjusting the values of these parameters in order to best match the known state of the Earth system.

There is no single procedure to tune a climate model but, generally, the first-order requirement is to provide a correct temperature of the system in equilibrium conditions, usually representing a pre-industrial climate. Moreover, it is fundamental to have globally outgoing (reflected) shortwave and longwave radiation at TOA which are in good agreement with the satellite observations [Mauritsen et al., 2012]. In this respect, almost all state-of-the-art climate models are tuned on the basis of the energy fluxes provided by the CERES-EBAF dataset.

To better illustrate the tuning of a climate model, we refer to figure 1.8, where the main processes tuned in the ECHAM model are shown [Mauritsen et al., 2012].

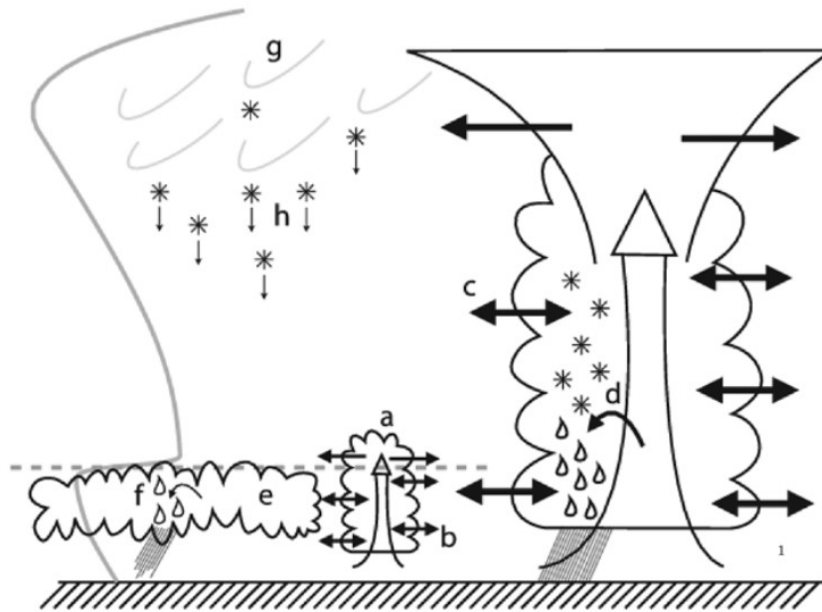


Figure 1.8: Processes tuned in the ECHAM model in Mauritsen et al. [2012]. Parameters are (a) convective cloud mass flux above the level of nonbuoyancy, (b) shallow convective cloud lateral entrainment rate, (c) deep convective cloud lateral entrainment rate, (d) convective cloud water conversion rate to rain, (e) liquid cloud homogeneity, (f) liquid cloud water conversion rate to rain, (g) ice cloud homogeneity, and (h) ice particle fall velocity.

Following the example of Hourdin et al. [2017], we consider the effect of the tuning of the ice crystal fall velocity, depicted by the process h in Figure 1.8. The effect of the scaling of this parameter on the RSR and the OLR is shown in Figure 1.9: when the fall velocity increases, the amount of ice clouds is reduced and, as a consequence, the reflected solar radiation, while the outgoing longwave radiation increases. Scientists set the value of this parameter so that the simulated OLR flux corresponds to the observed value within the measurement error ( $240 \pm 4 W m^{-2}$ ).

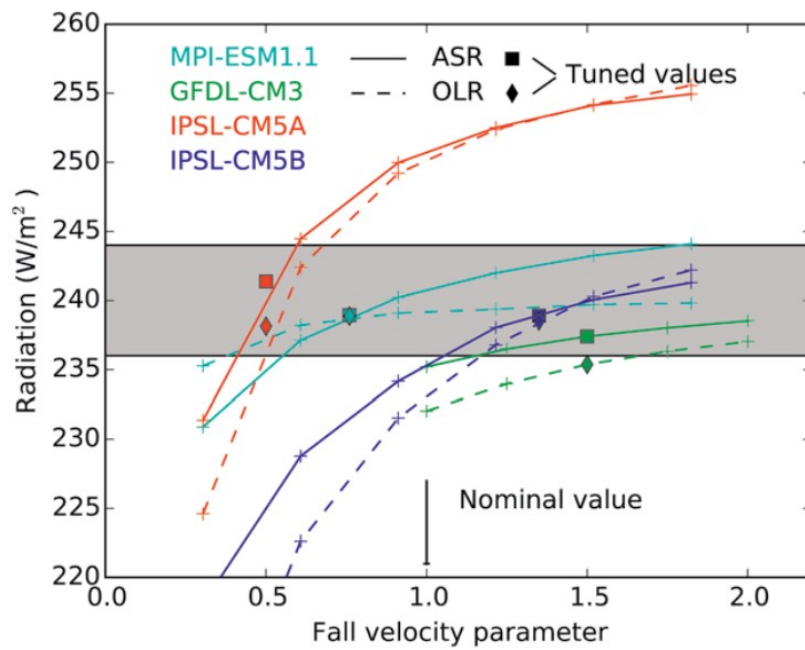


Figure 1.9: Example of tuning process described in Hourdin et al. [2017] involving the ice crystal fall velocity



# 2

## How well do climate models represent the Earth Energy Budget?

### 2.1 The Coupled Model Intercomparison Project

A large number of climate models is currently developed in different scientific centers around the world. These are periodically assessed and compared through the Coupled Model Intercomparison Projects (CMIPs). The CMIP, which has reached its sixth phase, represents the largest existing framework for the analysis, development and testing of climate models.

Its structure comprises five baseline experiments:

- Atmospheric Model Intercomparison Project (AMIP) simulation from 1979 to 2014;
- Pre-industrial control simulation (piControl or esm-piControl);
- Simulation forced by an abrupt quadrupling of CO<sub>2</sub> (abrupt-4× CO<sub>2</sub>);
- Simulation forced by a 1 % year CO<sub>2</sub> increase (1pct CO<sub>2</sub>);
- coupled historical simulation from 1850 to 2014.

In *AMIP simulations*, the Sea Surface Temperatures (SSTs) and Sea Ice Concentration (SIC) are prescribed based on observations. In this way, the internal variability of the models, as short-term climate cycles in the oceans, such as El Niño and La Niña events, are constrained to be as similar as possible to the real world. The prescribed SST and SIC come from the AMIP protocol configuration for CMIP6 [Eyring et al., 2016] and are provided as standard input to all models participating to CMIP6 (see also <https://pcmdi.llnl.gov/mips/amip/> and <https://esgfnod.llnl.gov/projects/input4mips/>). The comparison between AMIP simulations and observations allows to directly test the atmospheric component of the climate model.

Experiment short name	CMIP6 label	Experiment description	Forcing methods	Start year	End year	Minimum no. years per simulation	Major purpose
<b>DECK experiments</b>							
AMIP	<i>amip</i>	Observed SSTs and SICs prescribed	All; CO <sub>2</sub> concentration prescribed	1979	2014	36	Evaluation, variability
Pre-industrial control	<i>piControl</i> or <i>esm-piControl</i>	Coupled atmosphere-ocean pre-industrial control	CO <sub>2</sub> concentration prescribed or calculated	n/a	n/a	500	Evaluation, unforced variability
Abrupt quadrupling of CO <sub>2</sub> concentration	<i>abrupt-4xCO2</i>	CO <sub>2</sub> abruptly quadrupled and then held constant	CO <sub>2</sub> concentration prescribed	n/a	n/a	150	Climate sensitivity, feedback, fast responses
1 % yr <sup>-1</sup> CO <sub>2</sub> concentration increase	<i>1pctCO2</i>	CO <sub>2</sub> prescribed to increase at 1 % yr <sup>-1</sup>	CO <sub>2</sub> concentration prescribed	n/a	n/a	150	Climate sensitivity, feedback, idealized benchmark
<b>CMIP6 historical simulation</b>							
Past ~ 1.5 centuries	<i>historical</i> or <i>esm-hist</i>	Simulation of the recent past	All; CO <sub>2</sub> concentration prescribed or calculated	1850	2014	165	Evaluation

Figure 2.1: CMIP6 experiments configuration

*Pre-industrial control runs* are used to analyze the natural variability of the model at equilibrium, without external forcing, and to provide the reference outputs for the comparison with the other configurations. In the *Abrupt-4 CO<sub>2</sub>* experiments, the CO<sub>2</sub> concentration is fixed at 1120 ppm, four times higher than the pre-industrial value (280 ppm). These idealized simulations allow us to investigate the response of the Earth System to a strong radiative forcing, starting from a pre-industrial climate and holding all the other parameters constant. The *1pct CO<sub>2</sub>* represents another diagnostic test, where CO<sub>2</sub> emissions from pre-industrial levels is increased by 1% per year.

The so-called *historical runs* start from 1850 and allow scientists to compare long-term observations to model simulations, which are performed under observed (or estimated, for the first part) atmospheric greenhouse gas concentration, other natural and anthropogenic forcings (including aerosols), land use, etc. In addition, CMIP6 includes a large set of additional "MIPs", with experiments targeting specific issues in climate studies. The most participated is the ScenarioMIP, which defines a set of future scenarios of GHG, aerosol and land-use changes for the 21st century.

## 2.2 Climate Models Assessment

In this chapter, we assess the performance of the CMIP6 climate model in representing the energy fluxes at TOA. To do this, we have compared 15 years (2000-2014) of model outputs, provided by the AMIP simulations of 34 CMIP6 models, with the observational data contained in the CERES Energy Balance and Filled (EBAF) dataset. This dataset (<https://ceres.larc.nasa.gov/data/>) is built from observations collected by several instruments: CERES instruments, MODIS, VIIRS and almost 20 geostationary satellites. The observed fluxes are affected by uncertainties derived from calibration errors and from the conversion of the radiances, measured by different instruments, into fluxes. The calibration error is equal to about 2 Wm<sup>-2</sup> (two standard deviation) for the reflected solar energy

## Chapter 2. How well do climate models represent the Earth Energy Budget?

---

and to about  $4 \text{ Wm}^{-2}$  (two standard deviation) for the OLR [Loeb et al., 2018].

The study follows the work of Wild [2020], that has recently examined the radiative global budget of 40 state-of-the-art global climate models participating in the Coupled Model Intercomparison Project phase 6 (CMIP6) through a systematic comparison of global-averaged broadband energy fluxes at surface and TOA with the CERES-EBAF dataset (v. 4.0). In this work, these results are also compared to CMIP5 multi-model means. On the one hand, the last model generation shows better agreement with the observed values, as for the shortwave atmospheric clear-sky component and the radiative fluxes at the surface, which present important improvements with respect to CMIP5 models. On the other hand, large inter-model spreads persist, in particular for Cloud Radiative Effect at TOA and global mean latent heat fluxes.

In this thesis, we extended the analysis of the CMIP6 model biases on a regional scale, exploiting the new release of the CERES dataset as observational benchmark (v 4.1) .

The 34 CMIP6 models listed below have been selected for comparison because they provide all the variables under consideration over the whole period taken into account: BCC-ESM1, CAMS-CSM1, CERESM2, CESM2-FV2, CESM2-WACCM, CESM2-WACCM-FV2, CIESM, CMCC-CM2-HR4, CMCC-CM2-SR5, CNRM-CM-1, CNRM-CM6-HR, CNRM-ESM2, E3SM-1, EC-Earth3, EC-Earth3-AerChem, EC-Earth3-CC, EC-Earth3-Veg, FGOALS-f3-L, GISS-E2-1-G, HadGEM3-GC31-LL, HadGEM3-GC31-MM, INM-CM4-8, INM-CM5-0, IPSL-CM6A-LR, KIOST-ESM, MIROC6, MIROC-ES2L, MPI-ESM-1-2-HR, MPI-ESM-1-2-LR, MPI-ESM-1-2-HAM, MRI-ESM2-0, NESM3, NorESM2-LM, SAM0-UNICON.

In addition, the simulated variables we compared to the observed ones are listed below:

- OLR (Outgoing Longwave Radiation TOA)
- OLRCs (Outgoing Longwave Radiation TOA - clear sky conditions)
- RSR (Reflected Shortwave Radiation TOA)
- RSRCs (Outgoing Shortwave Radiation TOA - clear sky conditions)
- Clt (Cloud Cover)
- CRE<sub>lw</sub> (Cloud Radiative Effect Longwave)
- CRE<sub>sw</sub> (Cloud Radiative Effect Shortwave)
- LWP (Cloud Liquid Water Path)
- IWP (Cloud Ice Water Path)

Starting from the CMIP6 model outputs and the CERES dataset, we computed the global averages of both the observed and simulated quantities over the period 2000 - 2014, shown in Table 2.1. In the following, we discuss each variable in detail in a separate paragraph.

Then, to better investigate the distribution of the biases over the globe, we compare the simulated and observed climatologies. For the variables in Table 2.1, we provide the following plots: taking Figure 2.2 as example, the observed values are shown in panel A (top-left), the multi-model mean in panel B (top-right), their differences in panel C (bottom-left) and their zonal means in panel D. All the values are averaged over 15 years (2000-2014).

Variable	CERES	Multimodel	Unit
OLR	240.23 ± 0.23	238.40 ± 0.21	Wm <sup>-2</sup>
OLRCS	266.17 ± 0.30	262.21 ± 0.27	Wm <sup>-2</sup>
RSR	99.20 ± 0.25	100.64 ± 0.28	Wm <sup>-2</sup>
RSRCS	53.84 ± 0.14	52.94 ± 0.14	Wm <sup>-2</sup>
CLT	67.46 ± 0.16	64.23 ± 0.13	%
CRELW	25.90 ± 0.25	23.80 ± 0.34	Wm <sup>-2</sup>
CRESW	-45.35 ± 0.27	-47.70 ± 0.31	Wm <sup>-2</sup>

Table 2.1: Global mean of CMIP6 models (AMIP simulations) and CERES over the period 2000-2014, with the respective standard deviations.

## 2.2.1 Outgoing Longwave Radiation

As mentioned in Section 1.1.1, the total OLR flux is defined as the Earth radiance emitted at TOA, integrated over the solid angle and over the spectral range, from 100 to about 3000 cm<sup>-1</sup> (3 - 100 μm).

$$F = \int_{100}^{3000} d\nu \int_0^{2\pi} d\phi \int_0^{\pi/2} d\theta L_\nu(\theta, \phi) \cos(\theta) \sin(\theta) \quad (2.1)$$

OLR at TOA is mainly controlled by surface temperature and atmospheric humidity. As a consequence, maximum values of OLR on the globe are present over subtropical dry zones [15-30° N, 15-30° S], corresponding to the subsiding branches of the Hadley Cell. In contrast, over the narrow tropical belt of convective clouds, between about 15° S and 15° N, known as the intertropical convergence zone (ITCZ), the OLR drastically drops because the radiation emitted by the surface and lower atmospheric layers is absorbed by clouds and re-emitted at the cloud top at lower temperatures (see panels A,B in Figure 2.2).

On a global scale, the CMIP6 ensemble mean simulated OLR is about 2Wm<sup>-2</sup> less than the observed OLR (see Table 2.1). However, this result is within the 2 standard deviation uncertainty of CERES measurements.

Despite the good agreement on a global scale, the global map of the bias (panel C), shows how negative model biases dominate at most latitudes, with the exception of significant positive differences (reaching about 10 Wm<sup>-2</sup>) affecting tropical regions [15°S-15°N], especially Central Africa, South America and Indonesia. Although in the subtropics [15-30° S and 15-30° N] the negative biases are still visible in the zonal mean, over the tropics the biases are completely offset (panel D) when zonally averaged.

### Clear-sky

In the absence of clouds, the OLR is mostly controlled by the surface and vertical profile of temperature and concentration of GHGs. As a consequence, it is mainly related to the latitude and height of the emitting ground (see panels A,B in Figure 2.3). The pronounced minimum over the tropics found in the all-sky case (Fig 2.2 - panel D) is now strongly mitigated, even if the high concentration of water vapour still present here reduces the amount of the emitted OLR flux at TOA, with respect to subtropical latitudes. In this comparison, the negative biases occur throughout the globe, as shown in panels C and D.

## Chapter 2. How well do climate models represent the Earth Energy Budget?

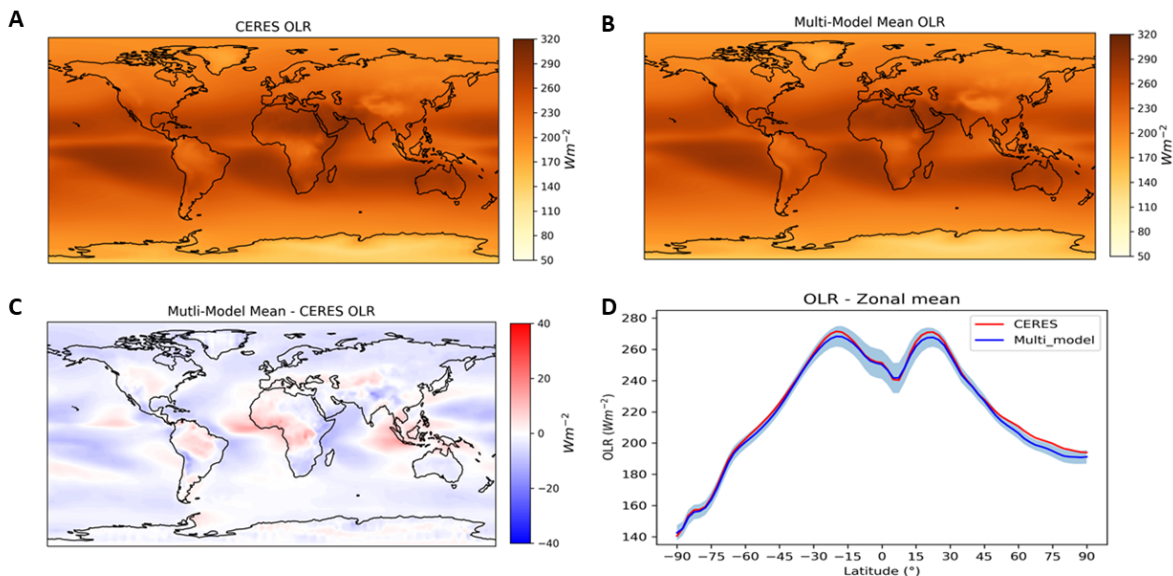


Figure 2.2: A: Observed OLR flux (top left); B: Multi-Model Mean of simulated OLR (top right); C: Difference (MODEL-OBSERVATION) (bottom left); D: Zonal multi-model mean and observed OLR (bottom right). The blue shade identifies the  $1\sigma$  (standard deviation) of multi-model mean

However, before going into more detail, it is relevant to indicate that the simulated clear-sky fluxes are generally not directly comparable to clear-sky observations. In fact, while the latter are inferred from clear-sky pixels or regions within the CERES instruments footprints that are cloud-free (on the basis of information provided by the high-spatial resolution spectral imager [Trepte et al., 2019]), clear-sky radiative computations in climate models exploit the same all-sky properties (e.g., surface temperature, temperature/humidity profile, surface albedo, aerosol), with only clouds removed. Since the temperature and humidity profiles of the models continue to be affected by the presence of clouds, a systematic negative bias persists when clear-sky simulated fluxes are compared with the observed ones.

According to Sohn et al. [2006], this difference can be significant, reaching up to  $-12 Wm^{-2}$  in active convective regions at tropical latitudes.

To mitigate this bias and to provide TOA clear-sky fluxes that are more in line with the clear-sky fluxes produced by climate models, a new adjustment factor ( $\Delta$ ) has been introduced in the CERES EBAF 4.1 dataset [Loeb et al., 2020], we exploit in this comparison. The correction term is derived from a monthly comparison of the synthetic fluxes computed following the approach of climate models and those inferred from clear-sky pixels of the observations. The  $\Delta$  factor is then used to correct the estimations of the clear-sky TOA fluxes contained in the previous release of the CERES dataset (EBAF 4.0) [Loeb et al., 2018].

As shown in Figure 2.4, the impact of  $\Delta$  is significant in the LW and it is negative over the tropical, subtropical and middle latitudes. As already mentioned, observed clear-sky fluxes are generally warmer with respect to climate model clear-sky output because models use moister and thus colder profiles in the radiative computation. On the contrary, the radiative computation in climate models produces the opposite impact over high latitudes,

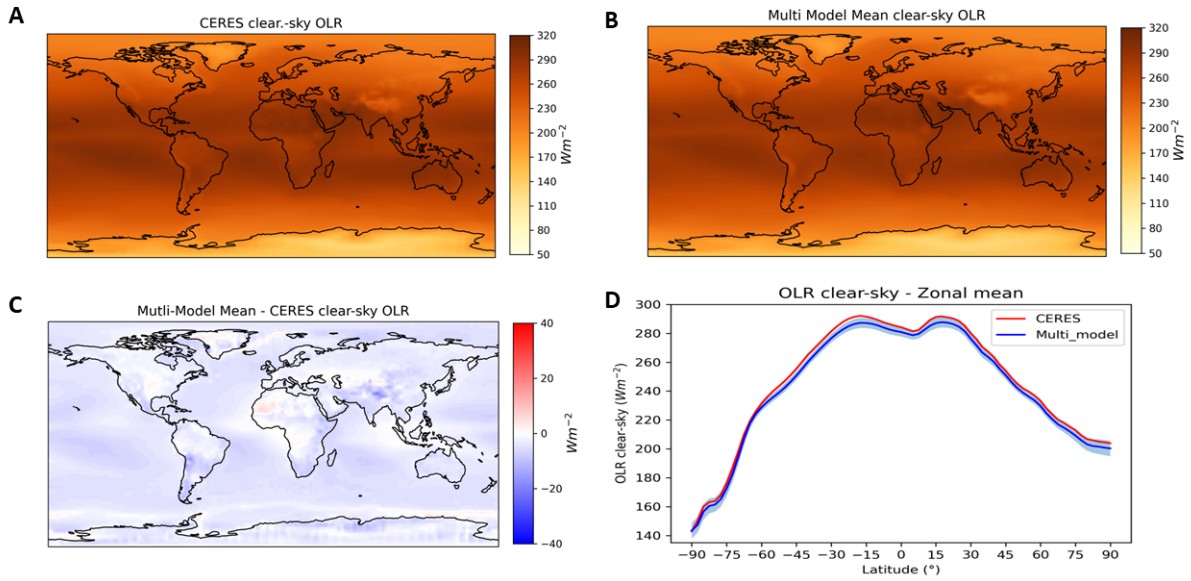


Figure 2.3: A: Observed OLRCS flux (top left); B: Multi-Model Mean of simulated OLRCS (top right); C: Difference (MODEL-OBSERVATION) (bottom left); D: Zonal multi-model mean and observed OLRCS (bottom right). The blue shade identifies the  $1\sigma$  (standard deviation) of multi-model mean ( $ORLCS$ ) averaged over 15 years

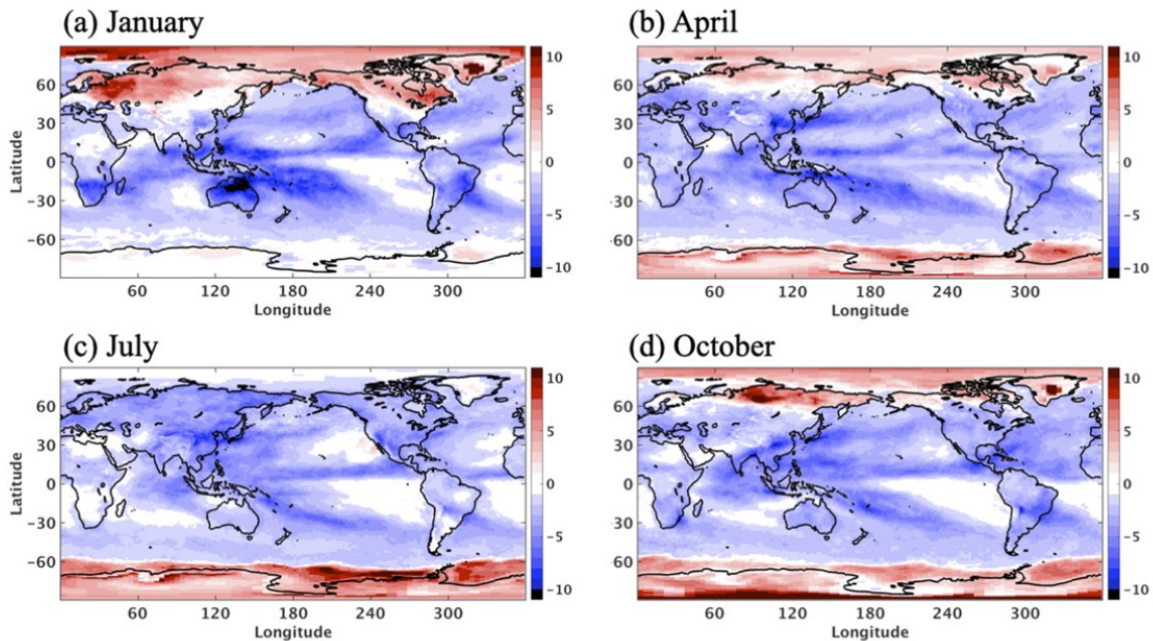


Figure 2.4: TOA LW adjustment for (a) January, (b) April, (c) July, and (d) October based upon 10-yr climatology of CERES EBAF data for July 2005–June 2015 (units:  $Wm^{-2}$ ). From [Loeb et al. \[2020\]](#)

keeping surface temperatures warm compared to observed cloud-free conditions. The global mean value of  $\Delta$  over the 10 years, from 2005 to 2015, is  $-2.2 Wm^{-2}$  with an error of  $0.15 Wm^{-2}$ .

## Chapter 2. How well do climate models represent the Earth Energy Budget?

---

In the analysis carried out by Wild [2020], which is based on the CERES dataset 4.0, the difference of the OLR clear-sky fluxes between CMIP6 models and observations is about  $6 \text{ Wm}^{-2}$ . On the contrary, in our comparison, due to the correction, this discrepancy is reduced to  $4 \text{ Wm}^{-2}$  on a global scale.

Wild [2020] also found that the CMIP6 models show a relevant improvement in the OLR estimation compared to the earlier model generations (CMIP5), even if a significant inter-model spread persists, with a standard deviation of  $2.8 \text{ Wm}^{-2}$  ( $2.9 \text{ Wm}^{-2}$  for the CMIP5 models) for the all-sky OLR and of  $2.6 \text{ Wm}^{-2}$  for OLR under clear sky conditions ( $3.3 \text{ Wm}^{-2}$  for CMIP5 models).

### 2.2.2 Outgoing Shortwave Radiation

The Reflected Shortwave Radiation (RSR) flux at TOA is defined as the solar reflected radiance integrated over the solid angle and over the spectral range, from about  $2500$  to about  $50000 \text{ cm}^{-1}$  ( $0.2 - 4 \mu\text{m}$ )

$$F_\nu = \int_{2500}^{50000} d\nu \int_0^{2\pi} d\phi \int_0^{\pi/2} d\theta L_\nu(\theta, \phi) \cos(\theta) \sin(\theta) \quad (2.2)$$

The area of maximum RSR corresponds to surfaces of high reflectivity, such as deserts, ice, snow and sea ice, or regions persistently affected by clouds. Indeed, the highest RSR values are found over the ITCZ, the Sahara desert, the Tibetan Plateau and over high-latitude areas such as Greenland and Antarctica, although much less incident solar radiation. On the contrary, the lowest RSR values are present over subtropical oceans dry zones. Even if simulated RSR radiation under all-sky and clear-sky conditions (RSR,RSRCS) shows good agreement with observations on a global scale, with a bias of about  $1 \text{ Wm}^{-2}$  (within 1 standard deviation of observational uncertainty), large regional differences are found throughout the globe (panel C of Figure 2.5) and between models, as indicated by the zonal standard deviation in panel D.

Positive biases dominate the oceans with the exception of the western coastlines of South and North America, Indian Ocean and Atlantic Ocean, where the difference between simulated and observed RSR reaches the value of  $-30 \text{ Wm}^{-2}$ . These biases can be related to the marine low clouds representation, that affects these regions with high frequency. Previous model generations (CMIP3, CMIP5) already exhibited large spread in the representation of marine low cloud cover (LCC), in particular in the subtropical stratocumulus regions off the west coasts of continents [Qu et al., 2014, Soden and Vecchi, 2011]. Furthermore, in this analysis, also the simulated aerosol concentration in the atmosphere could play a significant role: aerosol and their interactions with clouds induce a cooling effect on climate and the strength of this forcing is affected by large uncertainties (IPCC, 2018) and still poorly represented in AMIP models.

Finally, the uniform negative difference between modelled and observed RSR over the Southern Ocean is again most likely linked to LCC since the extension of this bias is too large to be compatible with the sea-ice cover. This known issue will be discussed further in the following paragraph.

#### Clear-sky

In the absence of clouds (see Figure 2.6), surface reflectivity directly controls the RSR flux reaching the TOA. As a consequence, the highest RSR values are found in the polar

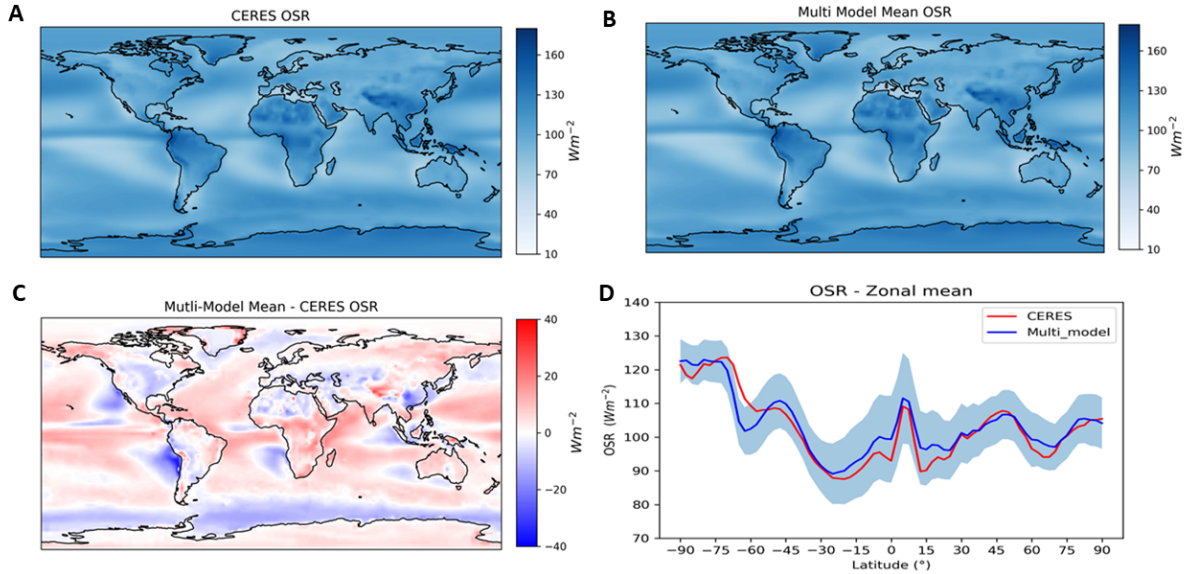


Figure 2.5: A: Observed RSR flux (top left); B: Multi-Model Mean of simulated RSR (top right); C: Difference (MODEL-OBSERVATION) (bottom left); D: Zonal multi-model mean and observed RSR (bottom right). The blue shade identifies the  $1\sigma$  (standard deviation) of multi-model mean ( $RSR$ ) averaged over 15 years

regions and desert areas (panels A,B). It is evident that, in clear sky conditions, the differences between the simulated and observed RSR fluxes are strongly reduced (panels C and D) with respect to the all-sky case, highlighting the importance of clouds for the representation of the global energy budget.

Strong negative differences still occur over North America, especially during boreal summer and spring (not shown), whereas a positive bias persists over Antarctica and northern polar regions, suggesting a potential bias in modeled snow reflectivity. Finally, a strong negative bias is present during austral summer along the Antarctica coastline (not shown), likely due to an overly simplified representation of sea-ice in climate models.

The strong positive bias occurring over the Tibetan Plateau in panel C of Figure 2.6 is likely due to the complexity of topography of the region, which is not well represented in plane-parallel radiative transfer schemes of the models [Lee et al., 2013].

The inter-model spread in the global mean RSR in CMIP6 and CMIP5 models has remained unchanged [Wild, 2020], indicating that model biases are persistent in this respect. The adjustment factor  $\Delta$  introduced in CERES-EBAF v4.1 (see previous paragraph), has a limited impact on the RSR: the global value of  $\Delta$ , obtained from the 10 years 2005 - 2015, is  $0.47 \pm 0.16 Wm^{-2}$ .

### 2.2.3 Cloud Radiative Effect

The presence of clouds strongly influences the TOA energy fluxes, with an opposite effect on the SW and LW radiation. To quantify the impact of clouds on radiation, clear-sky fluxes at TOA are compared to fluxes computed in the presence of clouds. The cloud radiative effect (CRE), in the LW and SW spectral ranges separately, is defined as follows:

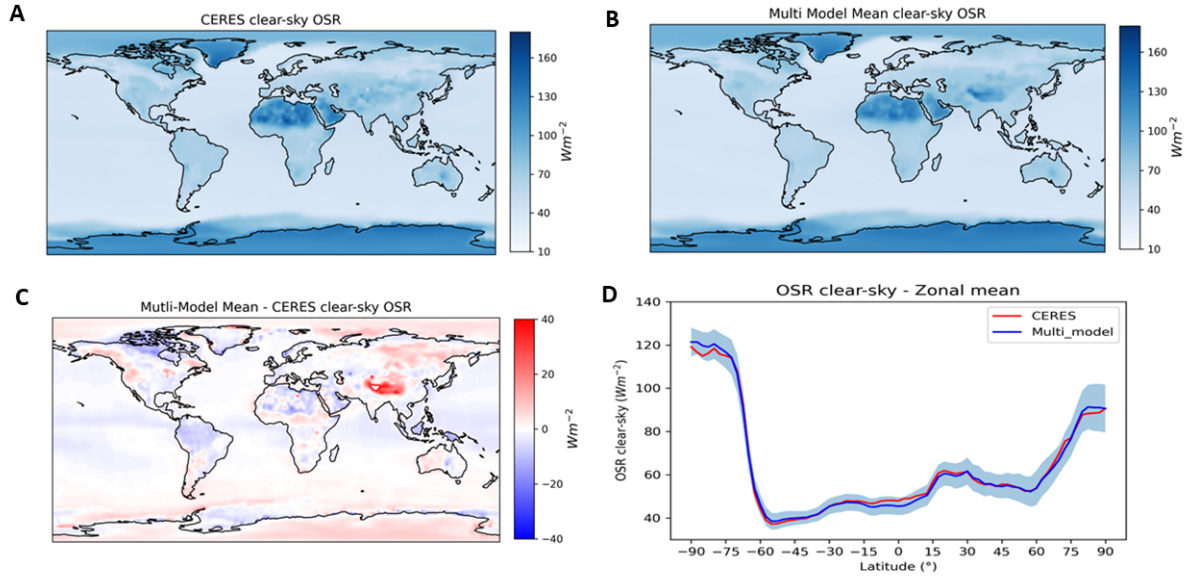


Figure 2.6: A: Observed RSRCS flux (top left); B: Multi-Model Mean of simulated RSRCS (top right); C: Difference (MODEL-OBSERVATION) (bottom left); D: Zonal multi-model mean and observed RSRCS (bottom right). The blue shade identifies the  $1\sigma$  (standard deviation) of multi-model mean ( $RSRCS$ ) averaged over 15 years

$$CRE_{LW} = OLR_{clear-sky} - OLR_{all-sky} \quad (2.3)$$

$$CRE_{SW} = RSR_{clear-sky} - RSR_{all-sky} \quad (2.4)$$

Generally, low clouds, that contain large amounts of water droplets, which are highly reflective, reflect back solar incoming radiation, resulting in a cooling effect of the climate [Stephens, 1978]. At the same time, the cloud top is low ( $< 2$  km), so the emission temperature at the cloud top is not that different from the surface one. On a global scale, in the SW spectral range, about  $-45.3$   $Wm^{-2}$  is reflected back to space due to clouds. In the CMIP6 multi-model mean this value is about  $-47.4$   $Wm^{-2}$ .

On the contrary, for the optically thick clouds or high clouds, the amount of reflected SW radiation is generally lower than the quantity of LW energy they trap in the Earth's System: in fact, they efficiently absorb the LW radiation and then re-emit it at higher altitude and, consequently, at a lower temperature. As a result, the emitted radiation is less than the absorbed one, causing a warming effect: from observational data, about  $25.9$   $Wm^{-2}$  of OLR are retained in the climate system due to clouds. Climate models simulate a lower CRE in the LW, approximately equal to  $23.8$   $Wm^{-2}$ .

Thus, on the one hand, climate models underestimate the CRE in the LW, while, on the other hand, they overestimate the CRE in the SW. The total CRE, given by the sum of LW and SW CRE components, shows an overall cooling effect of clouds in the Earth system: this amounts to about  $-20$   $Wm^{-2}$ , based on the CERES dataset, while it is approximately equal to  $-24$   $Wm^{-2}$  in the multi-model mean of CMIP6 models. So there is a general overestimation of the cooling effect of clouds in CMIP6 models, amounting to about  $4$   $Wm^{-2}$  globally.

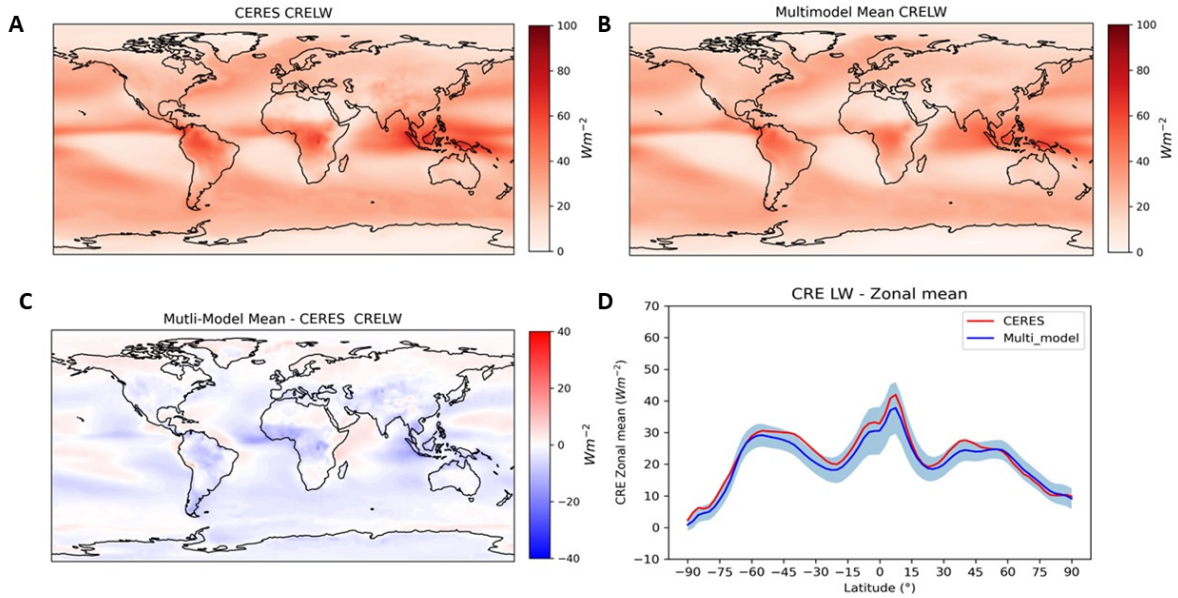


Figure 2.7: A: Observed CRE LW (top left); B: Multi-Model Mean of simulated CRE LW (top right); C: Difference (MODEL-OBSERVATION) (bottom left); D: Zonal multi-model mean and observed Cloud Cover (bottom right). The blue shade identifies the  $1\sigma$  (standard deviation) of multi-model mean ( $CLT$ ) averaged over 15 years

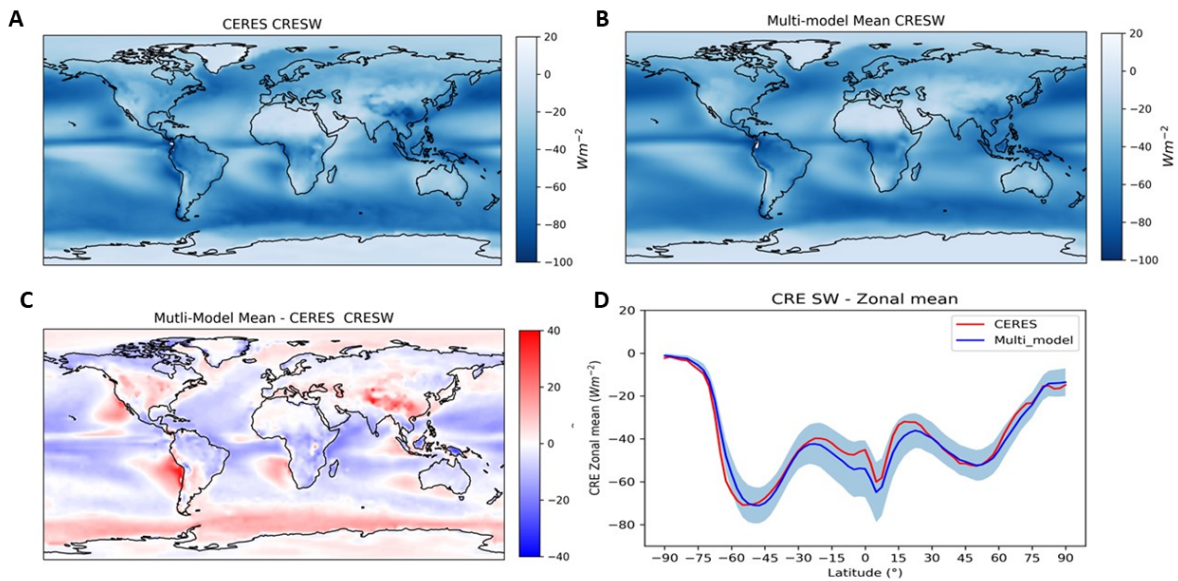


Figure 2.8: A: Observed CRESW (top left) ; B: Multi-Model Mean of simulated CRESW (top right); C: Difference (MODEL-OBSERVATION) (bottom left); D: Zonal multi-model mean and observed Cloud Cover (bottom right). The blue shade identifies the  $1\sigma$  (standard deviation) of multi-model mean ( $CLT$ ) averaged over 15 years

In Wild [2020], the global comparison of CRE between CMIP6 models and the observations provided by CERES shows a slightly greater discrepancy, approximately  $5 \text{ Wm}^{-2}$ . In fact, in that study the reference used for the comparison is the previous version of

## Chapter 2. How well do climate models represent the Earth Energy Budget?

---

CERES EBAF (edition 4.0), and the observed CRE in the LW and in the SW were about 28 and  $-46 \text{ Wm}^{-2}$  respectively [Loeb et al., 2018]. This difference depends again on the  $\Delta$  adjustment factor (see Section 2.2.1) that most affects the estimation of the CRE in the LW. Limited differences are found between the two CERES datasets for CRE in the SW, where the factor  $\Delta$  is smaller.

Panels C and D of Figure 2.7 highlight that the simulated CRE in the LW shows mostly negative biases, distributed quite homogeneously across the globe. Larger biases (of the order of  $30 \text{ Wm}^{-2}$ ) are detected in the shortwave CRE, where also the intermodel spread strongly increases (panel D of Figure 2.8).

Since the simulated and observed CRE in the shortwave are negative, when the biases in panel D of Figure 2.8 are positive, it indicates that climate models underestimate the effect of clouds on the reflected radiation (see Section 2.2.2). In this context, a long-standing issue in models concerns the underestimation of reflected shortwave radiation from clouds across the Southern Ocean [Trenberth and Fasullo, 2010] (Figure 2.8, panel C).

Kay et al. [2016] demonstrates that, in the case of the CESM1(CAM5) climate model, the bias is most likely originating from an insufficient amount of simulated supercooled liquid clouds, which strongly affect radiation at these latitudes.

### 2.2.4 Cloud Cover, Liquid and Ice content

Simulated cloud cover shows substantial differences with respect to observations (see Figure 2.9). Observed cloud properties of the CERES dataset are derived from MODIS and geostationary imager measurements [Minnis et al., 2020]. By comparing the output of the CMIP5 and CMIP6 models with observational data acquired by CLOUDSAT and CALIPSO over the period 2006 - 2011, Vignesh et al. [2020] found that the global mean cloud fractions of CMIP6 increased by about 4.5% with respect to CMIP5, reducing the gap with respect to observations (see Table 2.1). In the same work, a negative cloud cover bias is observed in most of the tropics and the mid-latitudes in both hemispheres, while a positive bias is found over high-latitudes, between  $60^\circ\text{N}$ – $80^\circ\text{N}$  and the  $60^\circ\text{S}$ – $80^\circ\text{S}$ . These results are in line with our comparison, shown in panels C and D of Figure 2.9.

At latitudes between  $60^\circ\text{S}$  and  $60^\circ\text{N}$ , the smallest biases occur in the tropics (5%), while the highest discrepancies are present in the subtropics and locally reach 10 %. At latitudes between  $15^\circ\text{S}$  and  $30^\circ\text{S}$ , the observed cloud cover is out the  $1 \sigma$  multi-model standard deviation range (see Figure 2.9 - panel D). These areas, affected by the largest negative differences, correspond to the regions affected by the highest discrepancies in the RSR comparison (see Section 2.2.2).

Finally, large differences are present at polar latitudes, especially over Antarctica, where models overestimate cloud cover. However, cloud cover detection in these regions is generally less reliable because the cloud tops and the surface have similar temperature and reflectivity [Trepte et al., 2003].

Cloud liquid water path (LWP) and cloud ice water path (IWP) are defined, respectively, as the total amount of liquid and ice particles vertically integrated inside the clouds. The zonally averaged observed values of LWP and IWP in Figures 2.10 are shown within  $70^\circ\text{S}$ ,  $+70^\circ\text{N}$  because, over polar latitudes, especially over Antarctica, few retrieval points are available from MODIS measurements in the CERES dataset. Since these variables show large differences between models, as shown by the zonal standard deviation, the ob-

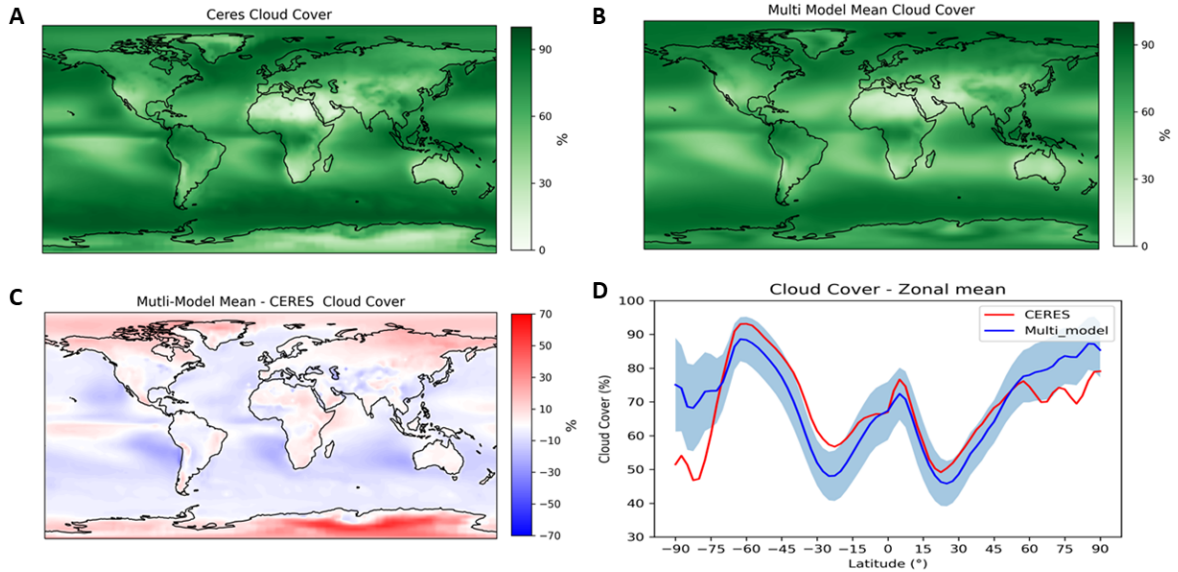


Figure 2.9: A: Observed Cloud Cover; B: Multi-Model Mean of simulated Cloud Cover; C: Difference (MODEL-OBSERVATION); D: Zonal multi-model mean and observed Cloud Cover. The blue shade identifies the  $1\sigma$  (standard deviation) of multi-model mean ( $CLT$ ) averaged over 15 years

served LWP is always within the multi-model standard deviation range (panel A of Fig. 2.10). In this context, it is also important to note that the accuracy of retrieved LWP from MODIS measurements is still debated. For example, a recent work of Khanal et al. [2020], highlights that LWP tends to be overestimated by MODIS measurements, particularly at high latitudes and, over around  $50^\circ$ , the bias can reach values up to  $+50 \text{ gm}^{-2}$ .

The observed distribution of IWP appears instead completely outside the range of CMIP6 models (Figure 2.10, right panel). However, this large difference between observed and simulated values is due to the fact that models make a clear distinction between precipitating and suspended cloud ice, while the retrieval products, computed from observations, constitute a mixture of both. In climate models, at each step, the precipitating ice cloud is removed and only the floating cloud ice is accounted for, which amounts to approximately 10 - 30 % of the total column of ice particles [Waliser et al., 2009]. Therefore, model results are in good agreement with this estimation, since the multi-model mean of the cloud ice water path is about 20% of the observed value.

## 2.3 Conclusions

In this work, we have compared the radiative fluxes and cloud variables obtained from climate model simulations with observational data provided by CERES, over the period 2000 - 2014. The comparison is based on multi-model means computed from 34 climate models participating to CMIP6, both in clear-sky and all-sky conditions. We consider here the AMIP simulations, so that all models are constrained with observed SSTs and SIC.

In general, CMIP6 models show good agreement with observations on a global scale, better than any previous generation of models [Wild, 2020]. In all-sky conditions, both

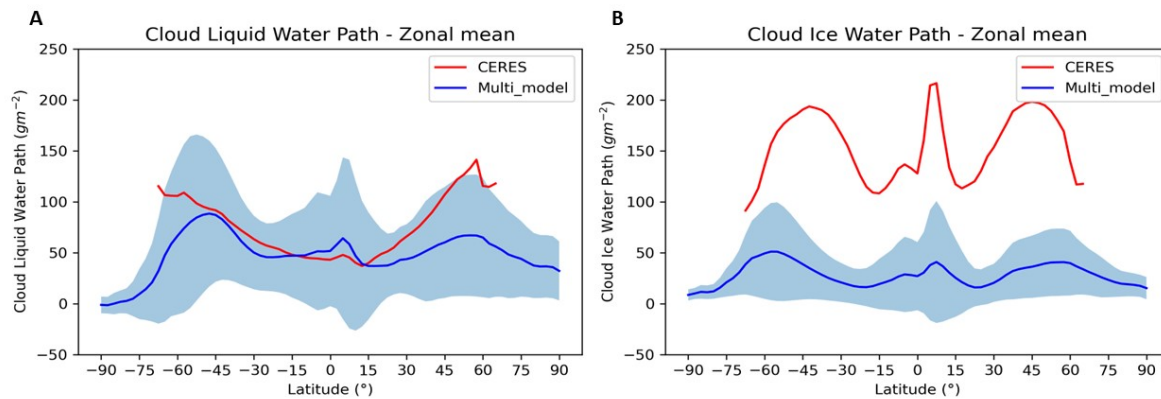


Figure 2.10: A: Zonal Cloud Liquid Water Path; B: Zonal Cloud Ice Water Path. The blue shade identifies the  $1\sigma$  (standard deviation) of multi-model mean averaged over 15 years

the OLR and RSR multi-model means are very close to the CERES reference values and largely within the  $2\sigma$  observational uncertainties provided by [Loeb et al. \[2018\]](#).

Nevertheless, the grid-point comparison performed here allows to highlight regions affected by significant biases, avoiding spatial compensation effects produced by the zonal and global averages. For example, at tropical and subtropical latitudes, the OLR at TOA, in all-sky conditions, shows large areas of positive and negative biases (up to  $10 \text{ Wm}^{-2}$ ), which are completely offset in the zonal average. Spatial compensation errors are even more pronounced in the comparison of all-sky RSR, where we found biases of the order of  $30 \text{ Wm}^{-2}$  locally, despite the good agreement between the observed and simulated global averages.

Comparisons of the all-sky and clear-sky OLR and RSR demonstrate that the largest biases originate mainly from the representation of clouds in models. This is especially evident for the RSR: while in the all-sky conditions large biases affect tropics, subtropics and the Southern Ocean, in the clear-sky comparison, differences are smaller and only limited to land, most likely due to the poor representation in climate models of topography, as in the case of the Tibetan Plateau, and snow reflectivity, as highlighted over polar regions.

In addition, climate models underestimate the positive LW CRE of approximately  $2 \text{ Wm}^{-2}$ , while they overestimate for about  $2 \text{ Wm}^{-2}$  the negative SW CRE (in absolute value). As a consequence, from the multi-model mean, the simulated cooling effect of clouds on the climate is approximately  $4 \text{ Wm}^{-2}$  more than that found in observations.

Despite the significant improvement achieved with respect to CMIP5 models, the cloud cover is still generally underestimated by climate models, which also show a significant inter-model spread. Largest differences occur over subtropics, where the reflected solar

radiation, analyzed through the CRE in the SW spectral range, is overestimated by models along the western coastlines of America, Africa and Australia. These biases are mostly linked to the representation of marine low clouds, which dominate over large-scale subsidence regions. Furthermore, the same type of clouds may be responsible for the wide and long-standing bias found over the Southern Ocean. In this context, a recent study of [Kay et al. \[2016\]](#) highlighted that this bias may originate from the insufficient amount of simulated supercooled liquid clouds at these latitudes.

Finally, a strong inter-model spread is found in the representation of the cloud liquid and ice content. However, the comparison of these variables is also made difficult due to lower reliability of the LWP and IWP inferred from measurements and the different definitions of the retrieved and simulated quantities.

The comparison of observed and simulated broadband fluxes provides fundamental information about the performance of climate models, and highlights the prominent role of clouds and the importance of their reliable representation in models. However, the detection of specific model biases is complicated by spectral integration, which may mask compensation errors, for example in the computation of the OLR. On the basis of these considerations, in the next Sections the analysis focuses on the comparison between simulated and observed spectrally resolved radiances. Indeed, the use of spectrally resolved OLR allows avoiding potential compensation errors. Furthermore, radiances contain the fingerprints of temperature, individual gases and clouds: from the differences between observations and simulations in specific spectral ranges, it is then possible to attribute the observed biases to the representation of specific climate variables in the GCMs.

# 3

## Teresina campaign: measurements of the Earth emission spectrum in the FIR and test of the $\sigma - IASI$ radiative transfer model

In the first chapter, we stressed the importance of spectrally resolved measurements of the outgoing longwave radiation, in addition to broadband fluxes. We here perform a first comparison between simulated and observed spectrally resolved radiances: observed spectra, measured during the field campaign of Teresina (Brazil) in 2005, are compared to synthetic spectra computed with the radiative transfer model (RTM)  $\sigma - IASI$ , on the basis of retrieved atmospheric profiles. The retrieval is performed using the FAsT Retrieval Model (FARM), a Bayesian retrieval algorithm, using the  $\sigma - IASI$  as forward model and for the calculations of Jacobians. Through this procedure, we verified the accuracy of the  $\sigma - IASI$  RTM in reproducing the Earth emission spectrum, both in the Far-Infrared and the Mid-Infrared spectral regions.

### 3.1 Teresina campaign

On June 30th 2005, from the airfield of Timon, near Teresina (Brazil), the first spectral measurements of FIR Earth's emission spectrum were performed by the Radiation Explorer in the Far InfraRed Prototype for Applications and Development (REFIR-PAD) from a stratospheric balloon. REFIR-PAD was the result of previous prototyping activities aimed at measuring spectrally resolved radiances in the FIR region without using expensive and inefficient cooled detectors, indispensable until that moment [Carli et al., 1999, Rizzi et al., 2002].

The field campaign was led by the French Centre National d'Etudes Spatiales (CNES) in collaboration with the European Space Agency (ESA) and REFIR-PAD was integrated

onboard the Laboratoire de Physique Moléculaire pour l'Atmosphère et l'Astrophysique (LPMAA) gondola, also hosting the Infrared Atmospheric Sounding Interferometer (IASI) balloon. During the 8 hours of flight at floating altitude of 34 km, REFIR-PAD acquired 45 sequences of observations (10 spectra per sequence) of the outgoing longwave radiance, covering the spectral range from 100 to 1400  $\text{cm}^{-1}$ , with a spectral apodized resolution of 0.475  $\text{cm}^{-1}$ .

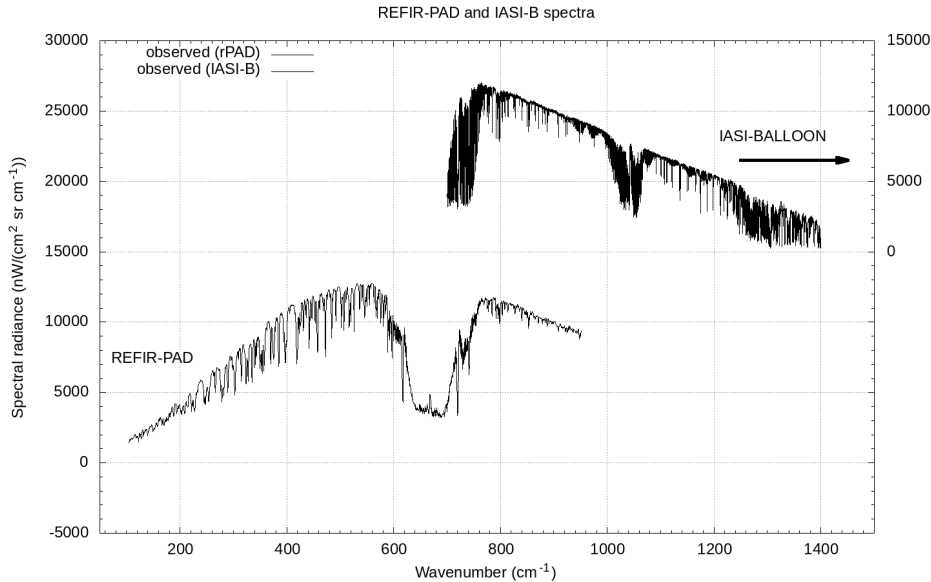


Figure 3.1: Examples of REFIR-PAD and IASI-Balloon measured spectra

On the same platform, IASI balloon measured radiances in the MIR spectral range, from 700 to 1400  $\text{cm}^{-1}$ . With a geometry similar to the IASI space-borne instrument, whose details will be presented in the next chapter, IASI balloon provided radiance measurements with a spectral apodized resolution of 0.1  $\text{cm}^{-1}$

### 3.2 The $\sigma$ -IASI radiative transfer model

$\sigma$ -IASI Radiative Transfer Model, developed at University of Basilicata [Amato et al., 2002], is a fast monochromatic RTM able to simulate up-welling infrared radiances at high resolution (0.01  $\text{cm}^{-1}$ ) in the 10 - 3000  $\text{cm}^{-1}$  range, Consequently, any Spectral Response Function (SRF) can be convoluted with the high-resolutions radiances, according to the specific instrument being processed. For each atmospheric layer, absorbing gas and wavenumber, the optical depths are computed using polynomial parametrizations determined on the basis of pre-tabulated values. The pre-tabulated optical depths of all trace species in correspondence of an appropriate and fixed layering were computed by KLIMA, a validated line-by-line RTM developed at IFAC-CNR [Cortesi et al., 2014, Del Bianco et al., 2013]. The inputs to the  $\sigma - IASI$  RTM are the surface pressure and temperature, the surface spectral emissivity, the profiles of temperature, humidity and concentrations of 11 gases (O<sub>3</sub>, CO<sub>2</sub>, N<sub>2</sub>O, CO, CH<sub>4</sub>, SO<sub>2</sub>, HNO<sub>3</sub>, NH<sub>3</sub>, OCS, HDO, CF<sub>4</sub>) and the cloud parameters (cloud cover, ice and liquid water content, effective radius of ice and liquid particles). The radiative transfer calculations are then performed using 61

### Chapter 3. Teresina campaign: measurements of the Earth emission spectrum in the FIR and test of the $\sigma - IASI$ radiative transfer model

---

fixed pressure levels and on a fixed wavenumber grid with a step of  $0.01 \text{ cm}^{-1}$ . The radiative code is also able to compute Jacobians with respect to all the geophysical variables, including the cloud parameters. Once the synthetic spectrum has been calculated by the RTM, it is possible to simulate the instrumental effects by convolving the spectral radiance with an Apodized Instrument Spectral Response Function (AISRF). In this case, to simulate the REFIR-PAD apodized measurement, we use as AISRF a Norton-Beer strong apodizing function [Norton and Beer, 1976, 1977] relative to a sampling of  $1/(2 \text{ MOPD}) = 0.5 \text{ cm}^{-1}$ , where MOPD is the Maximum Optical Path Difference adopted for the measurement. For IASI balloon spectra, we use the same AISRF relative to a sampling of  $1/(2 \text{ MOPD}) = 0.1 \text{ cm}^{-1}$ .

The  $\sigma - IASI$  RTM has been extensively validated against IASI measurements [Liuzzi et al., 2017], Aircraft based Measurements (NAST-I) [Grieco et al., 2007] and ground-based measurements [Serio et al., 2008]. In this work, we further test the accuracy of  $\sigma - IASI$  following 3 steps:

- The retrieval of surface and atmospheric properties from the measurements of REFIR-PAD and IASI balloon, considering single (only REFIR-PAD) and synergistic retrievals (section 3.3)
- The verification of retrieved quantities with correlative radiosondes measurements (section 3.4)
- The comparison of the observed and simulated spectra (section 3.5)

### 3.3 The inverse problem

To simulate the spectrally resolved radiances corresponding to the REFIR-PAD and IASI-balloon observations, we need to know the surface and atmospheric properties present during the measurements. In many cases, especially for satellite-borne instruments, we do not directly measure these quantities, but we derive them from the observed radiances  $\mathbf{y}$ . This is called the *inverse* problem.

Let assume that the state of the atmosphere is defined by a limited set of parameters (i.e., temperature, pressure, gases concentration, etc.) that are collected in the state vector  $\mathbf{x}$ . The computation of  $\mathbf{x}$ , starting from observations  $\mathbf{y}$ , is known as the inverse or retrieval problem.

First, to solve the inverse problem, we need a model that relates the measurements  $\mathbf{y}$  and the state vector  $\mathbf{x}$ :

$$\mathbf{y} = \mathbf{f}(\mathbf{x}) + \epsilon \tag{3.1}$$

Here,  $\mathbf{f}(\mathbf{x})$  represents the forward model or, in other terms, the radiative transfer equation used to simulate radiances starting from  $\mathbf{x}$ , while  $\epsilon$  describes the measurement error. In this study, the forward model is represented by the  $\sigma - IASI$  RTM followed by the AISRF convolution process.

In a Bayesian view, the inverse problem consists in finding the conditional probability  $P(\mathbf{x}|\mathbf{y})$  that is the probability the state vector  $\mathbf{x}$  is true under the condition we have obtained the measurements  $\mathbf{y}$ .

From the Bayes theorem:

$$P(\mathbf{x}|\mathbf{y}) = \frac{P(\mathbf{y}|\mathbf{x})P(\mathbf{x})}{P(\mathbf{y})} \quad (3.2)$$

Assuming that error  $\epsilon$  is normally distributed and characterized by its covariance matrix  $\mathbf{S}_y$ , we can explicitly write the terms of the equation 3.2:

- Assuming that  $\mathbf{y}$  is normally distributed, conditional probability  $P(\mathbf{y}|\mathbf{x})$  is written as a m-dimensional Gaussian distribution with mean  $\mathbf{f}(\mathbf{x})$  and standard deviation  $\mathbf{S}_y$ :

$$P(\mathbf{y}|\mathbf{x}) = \frac{1}{(2\pi)^{\frac{m}{2}} \det \mathbf{S}_y} e^{-\frac{(\mathbf{y}-\mathbf{f}(\mathbf{x}))^t \mathbf{S}_y^{-1} (\mathbf{y}-\mathbf{f}(\mathbf{x}))}{2}} \quad (3.3)$$

- We introduce an a-priori estimation of the vector state  $\mathbf{x}$ , identified by  $\mathbf{x}_a$ , and an associated error represented by the covariance matrix  $\mathbf{S}_a$ .

Assuming  $\mathbf{x}$  normally distributed, the a-priori probability  $P(\mathbf{x})$  is defined as:

$$P(\mathbf{x}) = \frac{1}{(2\pi)^{\frac{n}{2}} \det \mathbf{S}_a} e^{-\frac{(\mathbf{x}-\mathbf{x}_a)^t \mathbf{S}_a^{-1} (\mathbf{x}-\mathbf{x}_a)}{2}} \quad (3.4)$$

- Finally, we do not have an analytical expression for  $P(\mathbf{y})$  but it does not depend on  $\mathbf{x}$  and it is just a normalization factor.

As a result, from the previous equations, we obtain:

$$P(\mathbf{x}|\mathbf{y}) = \frac{1}{(2\pi)^{\frac{n+m}{2}} \det \mathbf{S}_a \det \mathbf{S}_y} e^{-\frac{(\mathbf{x}_a-\mathbf{x})^t \mathbf{S}_a^{-1} (\mathbf{x}_a-\mathbf{x}) + (\mathbf{y}-\mathbf{f}(\mathbf{x}))^t \mathbf{S}_y^{-1} (\mathbf{y}-\mathbf{f}(\mathbf{x}))}{2}} \quad (3.5)$$

### 3.3.1 Maximum Likelihood

It is now possible to extract the best estimate of  $\mathbf{x}$  starting from equation 3.5. The maximum likelihood method seeks the solution that "best" explains the observed dataset  $\mathbf{y}$ , assuming that it is described by a normal distribution.

In order to maximize the probability in 3.5, we have to minimize the exponent, that is the cost function:

$$\chi^2 = (\mathbf{x}_a - \mathbf{x})^t \mathbf{S}_a^{-1} (\mathbf{x}_a - \mathbf{x}) + (\mathbf{y} - \mathbf{f}(\mathbf{x}))^t \mathbf{S}_y^{-1} (\mathbf{y} - \mathbf{f}(\mathbf{x})) \quad (3.6)$$

Thus, we look for the solution of  $\nabla_x \chi^2 = 0$ .

We can write:

$$\nabla_x \chi^2 = -2\mathbf{K}^t \mathbf{S}_y^{-1} (\mathbf{y} - \mathbf{f}(\mathbf{x})) - 2\mathbf{S}_a^{-1} (\mathbf{x} - \mathbf{x}_a) \quad (3.7)$$

where  $\mathbf{K}$  is the jacobian matrix of the function  $\mathbf{f}(\mathbf{x})$ , defined as:

$$K_{i,j} = \frac{\partial f_i(x)}{\partial x_j} \quad (3.8)$$

In many cases, the equation 3.7 does not have an analytical solution and it is necessary to solve it numerically.

### 3.3.2 The Gauss-Newton Method

The Gauss-Newton method represents one of the numerical methods we can apply to solve equation 3.7. Considering we want to find the zero of a uni-dimensional function  $g(x)$ , with  $x \in (a, b)$  (see picture 3.2), we can write:

$$x_{i-1} - x_i = g(x_{i-1}) \tan(\pi/2 - \alpha) = \frac{g(x_{i-1})}{g'(x_{i-1})} \quad (3.9)$$

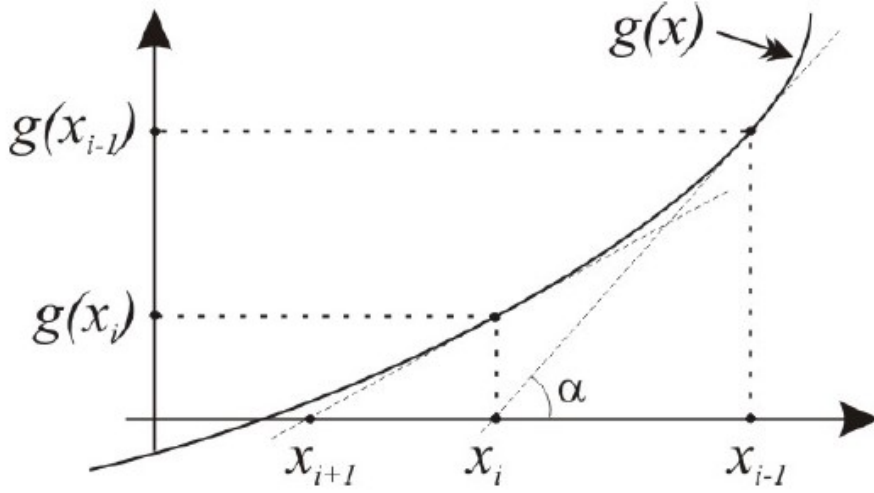


Figure 3.2: Newton's Method

As a consequence, we have:

$$x_i = x_{i-1} - g(x_{i-1}) \tan(\pi/2 - \alpha) = \frac{g(x_{i-1})}{g'(x_{i-1})} \quad (3.10)$$

We can now find the tangent of the function at the point  $x_i$  and apply the same procedure to find the intersection of the tangent at the point  $x_{i+1}$ .

This expression can be iterated until convergence is reached, on the basis of a predefined convergence criteria.

It is important to note that the iterative method just explained fails if the functions is not monotonic or if more zeros of the function exist.

Extending the solution to n-dimensional space, we can write:

$$\mathbf{x}_i = \mathbf{x}_{i-1} - \mathbf{J}^{-1} \mathbf{g}(\mathbf{x}_{i-1}) \quad (3.11)$$

where  $\mathbf{J}$  is the jacobian of  $\mathbf{g}$ , defined as  $J_{k,h} = \left[ \frac{\partial g_k}{\partial x_h} \right]_{x=x_{i-1}}$

If we apply this method to the inverse problem, we aim to find the minimum of  $\chi^2$  expressed by equation 3.6. The Jacobian  $\mathbf{J}$  is now the Hessian of the  $\chi^2$  and it results:

$$\mathbf{J} = \frac{\partial \nabla \chi^2(\mathbf{x})}{\partial \mathbf{x}} = 2\mathbf{K}^t \mathbf{S}_y^{-1} \mathbf{K} - 2[\nabla_x \mathbf{K}^t] \mathbf{S}_y^{-1} (\mathbf{y} - \mathbf{f}(\mathbf{x})) + 2\mathbf{S}_a^{-1} \quad (3.12)$$

The second term in the expression above is related to the second derivatives of the function  $\mathbf{f}$ . The approximation, known as Gauss-Newton method, consists in neglecting

this term, which is often small. With this approximation, the Gauss-Newton method provides the following result:

$$\mathbf{x}_i = \mathbf{x}_{i-1} + (\mathbf{K}^t \mathbf{S}_y^{-1} \mathbf{K} + \mathbf{S}_a)^{-1} [\mathbf{K}^t \mathbf{S}_y^{-1} (\mathbf{y} - \mathbf{f}(\mathbf{x}_{i-1})) + \mathbf{S}_a^{-1} (\mathbf{x}_a - \mathbf{x}_{i-1})] \quad (3.13)$$

This expression can be iterated until convergence is reached, on the basis of a pre-defined convergence criteria. Finally, we can write the following solution:

$$\tilde{\mathbf{x}} = \mathbf{x}_0 + (\mathbf{K}^t \mathbf{S}_y^{-1} \mathbf{K} + \mathbf{S}_a^{-1})^{-1} [\mathbf{K}^t \mathbf{S}_y^{-1} (\mathbf{y} - \mathbf{f}(\mathbf{x}_0)) + \mathbf{S}_a^{-1} (\mathbf{x}_a - \mathbf{x}_0)] \quad (3.14)$$

The error of the solution, depending on the error affecting the a-priori estimation and the error associated to the measurements  $\mathbf{y}$ , is described by the following equation:

$$\mathbf{S}_x = (\mathbf{K}^t \mathbf{S}_y^{-1} \mathbf{K} + \mathbf{S}_a^{-1})^{-1} \quad (3.15)$$

### 3.3.3 Averaging Kernels

The Averaging Kernels Matrix  $\mathbf{A}$  defines the relation between the retrieved state vector  $\tilde{\mathbf{x}}$  and the true state vector  $\mathbf{x}$ . Indeed, its elements are the partial derivatives  $\frac{\partial \tilde{x}_i}{\partial x_j}$  of the  $i$ -th component of the estimated state variables with respect to the  $j$ -th component of the true state variable  $\mathbf{x}$ .

We can compute the expression for the averaging kernels from the equation 3.13:

$$\mathbf{A} = (\mathbf{K}^t \mathbf{S}_y^{-1} \mathbf{K} + \mathbf{S}_a^{-1})^{-1} (\mathbf{K}^t \mathbf{S}_y^{-1} \mathbf{K}) \quad (3.16)$$

The  $i$ -th row of the matrix  $\mathbf{A}$  indicates how much the  $i$ -th component of the retrieval is sensitive to the different components of the atmospheric state. If the retrieval is perfectly constrained and the error of the *a-priori* is equal to zero ( $\mathbf{S}_a = 0$ ),  $\mathbf{A}$  is the identity matrix. However, in general, the matrix  $\mathbf{A}$  is not symmetric and the non-diagonal elements represent the effect of the perturbation of the true state on the retrieved parameters.

A useful metric to test the sensitivity of the retrieval is to compute the degrees of freedom (DOFs), defined as the trace of matrix  $\mathbf{A}$ :  $Tr(\mathbf{A}) = \sum_i \mathbf{A}_{i,i}$ . For a well constrained problem, the number of degrees of freedom is close to the number of retrieved parameters.

### 3.3.4 Retrieval strategy

The MIR and FIR intervals of the electromagnetic spectrum are differently sensitive to atmospheric and surface variables. In this work, atmospheric profiles are retrieved both using REFIR-PAD measurements alone and also combining IASI balloon and REFIR-PAD measurements, in order to extract information from different spectral regions, improving the retrieval product in terms of resolution and errors reduction [Ridolfi et al., 2022]. This procedure is called synergistic retrieval and its solution is obtained by fitting simultaneously the radiances acquired by the two instruments with the forward model simulations, i.e., by minimizing the cost function:

$$\chi^2 = (\mathbf{x}_a - \mathbf{x})^t \mathbf{S}_a^{-1} (\mathbf{x}_a - \mathbf{x}) + \sum_{i=1,2} (\mathbf{y}_i - \mathbf{f}_i(\mathbf{x}))^t \mathbf{S}_{y_i}^{-1} (\mathbf{y}_i - \mathbf{f}_i(\mathbf{x})) \quad (3.17)$$

### Chapter 3. Teresina campaign: measurements of the Earth emission spectrum in the FIR and test of the $\sigma - IASI$ radiative transfer model

where we indicate with  $i=1$  REFIR-PAD and  $i=2$  IASI balloon. From the Gauss-Newton method, we obtain the same solution of 3.13, but extended to two instruments:

$$\tilde{\mathbf{x}} = \mathbf{x}_0 + \left[ \sum_{i=1,2} \mathbf{K}_i^t \mathbf{S}_{y_i}^{-1} \mathbf{K}_i + \mathbf{S}_a^{-1} \right]^{-1} \left[ \sum_{i=1,2} \mathbf{K}_i^t \mathbf{S}_{y_i}^{-1} (\mathbf{y}_i - \mathbf{f}_i(\mathbf{x}_0)) + \mathbf{S}_a^{-1} (\mathbf{x}_a - \mathbf{x}_0) \right] \quad (3.18)$$

The error expressed by the covariance matrix is now described by:

$$\mathbf{S}_{\tilde{\mathbf{x}}} = \left[ \sum_{i=1,2} \mathbf{K}_i^t \mathbf{S}_{y_i}^{-1} \mathbf{K}_i + \mathbf{S}_a^{-1} \right]^{-1} \quad (3.19)$$

In the application of the synergistic retrieval, we select correspondent REFIR-PAD and IASI balloon measurements with temporal mismatch within few minutes. As a consequence, the measurements refer to the same atmospheric condition and we retrieve one state vector  $\mathbf{x}$ , characterizing the same atmosphere:

$$\mathbf{x} = \begin{pmatrix} \mathbf{T}(p) \\ \mathbf{x}_{\text{CO}_2}(p) \\ T_s \\ \mathbf{q}(p) \\ \mathbf{x}_{\text{O}_3}(p) \end{pmatrix} \quad (3.20)$$

The state vector includes the surface temperature  $T_s$ , the profiles of temperature  $\mathbf{T}(p)$ , water vapour  $\mathbf{q}(p)$ , ozone  $\mathbf{x}_{\text{O}_3}(p)$  and carbon dioxide  $\mathbf{x}_{\text{CO}_2}(p)$ .

All the quantities are retrieved at 48 heights, from the surface ( $p = 1009$  hPa) to the stratosphere ( $p = 29$  hPa).

Finally, the a-priori values ( $\mathbf{x}_a$ ) are provided by the dataset of the Atmospheric Constituent Profiles [Anderson et al., 1986], referring to a standard tropical atmosphere.

## 3.4 Validation of the retrieval

The temperature and the humidity profiles derived from the inversion of REFIR-PAD measurements (rpad-red) and from the synergistic inversion of REFIR-PAD and IASI balloon measurements (syn-black) are shown in figure 3.3. In the same plot, we added the temperature and water vapour profiles measured up to 10 km on 30 June 2005 by three nearby radiosondes, that are distant about 400 km from each other and about 250 km from Teresina.

The spectra used for the retrieval are chosen in order to have the best coincidence with the daily measurements provided at 12 UTC by the radiosondes.

The measured temperature profiles are well reproduced by the retrieved ones and the largest discrepancy is found only at about 6 km and it is limited to the synergistic case.

On the contrary, water vapour concentration profiles obtained from REFIR-PAD and IASI present some discrepancies with respect the radiosondes measurements. However, also the water vapour profiles provided by the radiosondes show a marked variability (right plot in figure 3.3), in particular way between 5 and 10 km. In addition, radiosondes perform higher spatial resolution measurements compared to the retrieved profiles.

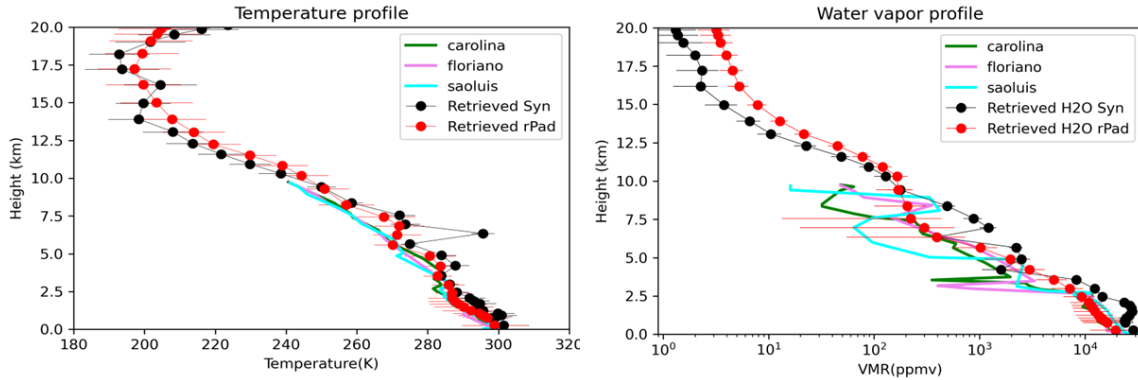


Figure 3.3: Comparison between the retrieved profiles of temperature (left) and water vapour (right), obtained from the inversion of REFIR-PAD measurements (rpad) and by the synergistic inversion of REFIR-PAD and IASI balloon measurements (syn). In the plot are also shown the measured profiles of temperature and water vapour provided by nearby radiosondes (Carolina, Floriano, Sao Luis).

Since Teresina is distant about 200 km from the closest radiosonde site (Floriano), we can consider the results of the two retrievals in a reasonable agreement with the measurements.

Now we wonder to what extent the observations contribute to determining the state vector  $\mathbf{x}$ . A value of DOF equal to 0 means that all information is provided by *a-priori*. In contrast, a value of DOF equal to the dimension of the retrieved profiles indicates that all the information is extracted from the measurements.

The DOFs computed for each variable, shown in Table 3.1, suggest that the results of the retrieval take enough information from the measurements, in both the inversion cases (rpad, syn). However, in the synergistic retrieval, profiles result better constrained by the measurements and less dependent on the *a priori*: for example, in the case of temperature profile, the DOFs are approximately 18 compared to 12 obtained from the inversion based exclusively on the REFIR-PAD measurements, but the same generally occurs for all the other quantities.

### 3.5 Verification of the $\sigma$ -IASI radiative transfer model

Starting from the retrieved profiles, we compute the synthetic spectra through the forward RTM  $\sigma - IASI$ . Figure 3.4 shows the comparison of the observed and simulated spectra for the two instruments in the case of synergistic retrieval. The black spectra indicate the observations, while the red ones represent the simulated spectra. In both cases, the residuals (differences between observation and simulation) are very small and they are

### Chapter 3. Teresina campaign: measurements of the Earth emission spectrum in the FIR and test of the $\sigma - IASI$ radiative transfer model

Parameter	Dimension	DOFs (rpad)	DOFs (syn)
$\mathbf{T}(p)$	48	12.36	18.43
$\mathbf{x}_{\text{CO}_2}(p)$	48	6.20	11.97
$T_s$	1	0.99	1.00
$\mathbf{q}(p)$	48	3.78	8.49
$\mathbf{x}_{\text{O}_3}(p)$	48	0.29	3.48

Table 3.1: Degrees of freedom for each retrieved parameter type. We distinguish between results obtained from REFIR-PAD inversion (rpad) and synergistic inversion of REFIR-PAD and IASI balloon (syn).

within the measurement error ranges.

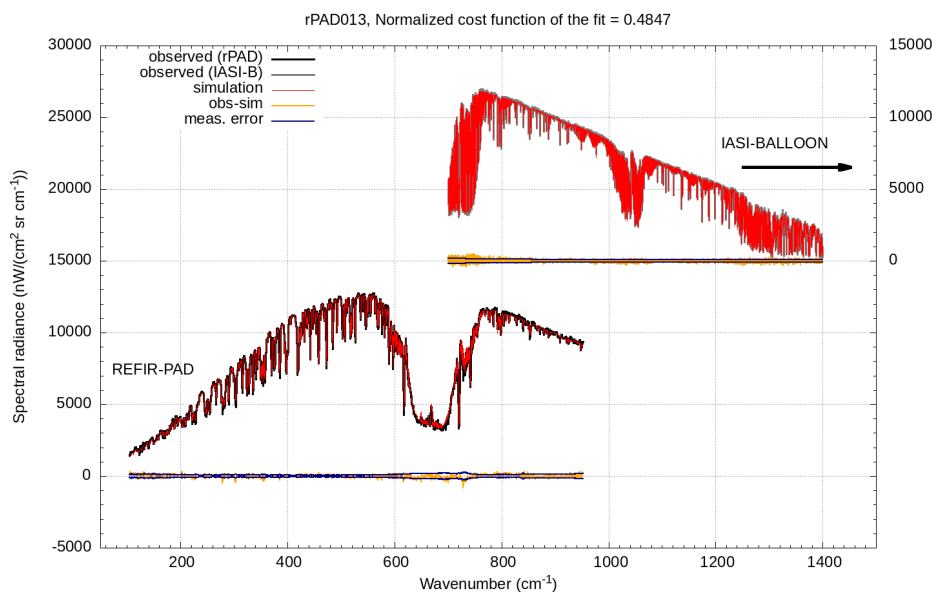


Figure 3.4: Comparison between the observed (black) and simulated spectra (red) of REFIR-PAD and IASI balloon. For both spectra, the residuals (orange) and the measurement noise error ranges (blue) are plotted.

## 3.6 Conclusions

In this chapter, we described the measurement campaign carried out in Teresina (Brazil), in 2005. The measurements performed in this occasion are important in the study of the Earth emission spectrum because, for the first time, the FIR spectral range was measured without the use of cooled detectors by the REFIR-PAD instrument. This technology allowed to design the FORUM mission, that from 2027 will provide measurements of the FIR spectral range from space. During the Teresina campaign, on the same platform hosting REFIR-PAD, the IASI balloon instrument was also operated, in order to perform measurements of the OLR radiances over the MIR spectral interval.

Surface temperature  $T_s$  and profiles of temperature  $\mathbf{T}(p)$ , water vapour  $\mathbf{q}(p)$ , ozone  $\mathbf{x}_{\text{O}_3}(p)$  and carbon dioxide  $\mathbf{x}_{\text{CO}_2}(p)$  were retrieved from the measurements. Retrieval has

been performed both using only the REFIR-PAD measurements and using the combined measurements of REFIR-PAD and IASI balloon. The products obtained from the two procedures show that in the second case, the so-called synergistic retrieval, more information is extracted from the measurements and the derived profiles are less dependent on the a-priori. This is due to the different sensitivity of the MIR and FIR spectral ranges to the atmospheric variables we inferred, and to the greater amplitude of the spectral interval involved in the synergistic retrieval. In addition, the retrieved profiles of temperature and water vapour agree with the existing measurements performed by nearby radiosondes.

Finally, we compared the observations provided by these two instruments, with the simulations performed with the  $\sigma$ -IASI RTM, a fast radiative code able to provide high resolution radiances of the whole Earth emission spectrum, which can be convolved with the spectral function response of any instrument. Although the accuracy of  $\sigma$ -IASI has already been assessed in the past by comparison with different sensors (ground-based, space-borne), we further tested the accuracy of this RTM by extending the comparison to balloon-borne measurements involving also the FIR region. This further validation strengthens our confidence on the  $\sigma$ -IASI performance, in view of its implementation in a climate model. The synthetic spectra were calculated on the basis of profiles inferred from the synergistic retrieval. The good agreement, both in the case of REFIR-PAD and IASI balloon, confirms the high accuracy of  $\sigma$ -IASI RTM.

Based on these results, as described in the next chapter, the  $\sigma$ -IASI RTM has been implemented in a climate model, with the aim to build a climatology of synthetic, spectrally resolved, radiances to be compared to analogous climatology, based on satellite measurements.

# 4

## The contribution of IASI observed radiances to the detection of EC-Earth climate model biases

The work presented in this chapter aims at the assessment of possible wavenumber-dependent biases in the OLR predicted by the EC-Earth climate model. To this end, we first implemented the  $\sigma$ -IASI RTM in the Cloud Feedback Model Intercomparison Project (CFMIP) Observation Simulator Package (COSP) that can be run online with the climate model. After verification, the EC-Earth model equipped with the upgraded COSP module has been run with prescribed sea surface temperature and sea-ice concentration, every 6 hours, to build a climatology of OLR spectral radiances in the years from 2008 to 2016, a timeframe consistent with the availability of IASI measurements. We then computed an analogous climatology of IASI measured spectral radiances and carried out a critical comparison of measured and model climatologies in  $10\text{ cm}^{-1}$ -wide intervals spanning the IASI spectral region, from  $650$  to  $2760\text{ cm}^{-1}$ . As explained in the next Sections, for convenience the analysis focuses on geographical regions over the ocean, in the latitude belt from  $30^\circ\text{S}$  to  $30^\circ\text{N}$ , and is limited to clear sky conditions. The results of this analysis are also published in [Della Fera et al. 2022](#).

### 4.1 Models

#### 4.1.1 EC-Earth Climate Model

The EC-Earth climate model version 3.3.3 ([Hazeleger et al. \[2010\]](#), [Döscher et al. \[2021\]](#), <http://www.ec-earth.org>) is a state-of-the-art, high-resolution Earth-system model participating in the last intercomparison project (CMIP6) [[Eyring et al., 2016](#)]. EC-Earth model (Figure 4.1) includes advanced, robust and validated components for the atmosphere (the ECMWF IFS model cy36r4), the ocean (NEMO 3.6, [[Madec et al., 2017](#)]), sea

ice (LIM3, [Fichefet and Maqueda, 1997]) and land processes (H-Tessel, [Balsamo et al., 2009]). The model exploits the approximations introduced in Section 1.3.3 to compute the integrated broadband fluxes. Furthermore, it has been tuned by minimizing the differences in the radiative fluxes at TOA and at the surface with respect to the observed fluxes from the CERES-EBAF-Ed4.0 dataset [Döscher et al., 2021].

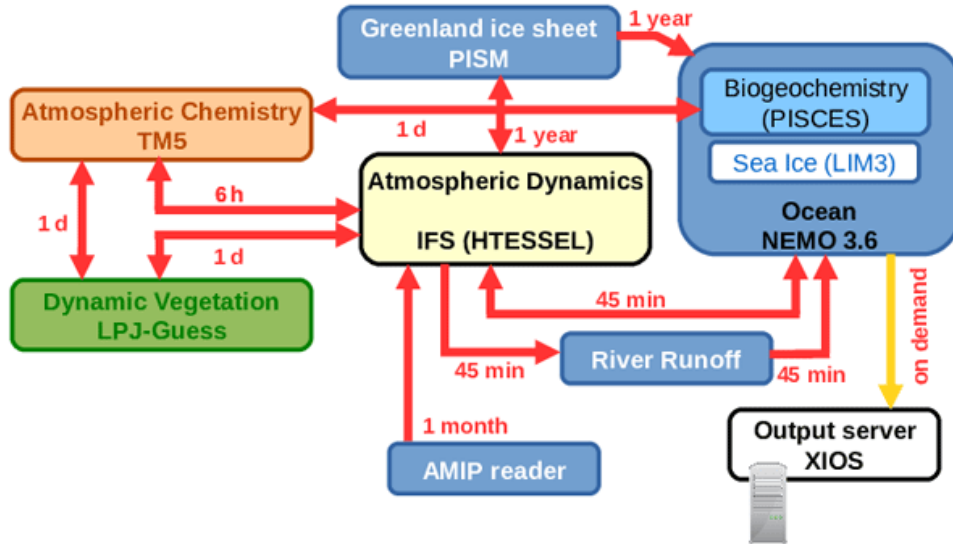


Figure 4.1: EC-Earth3 components and couplings

In this work, atmosphere-only historical simulations have been performed with prescribed Sea Surface Temperatures (SSTs) and Sea Ice Concentration (SIC) in the standard resolution TL255L91-ORCA1 used for CMIP6. More in detail, the prescribed SST and SIC come from the AMIP protocol configuration for CMIP6 [Eyring et al., 2016] and are provided as standard input to all models participating in CMIP6 (see also <https://pcmdi.llnl.gov/mips/amip/> and <https://esgfnod.llnl.gov/projects/input4mips/>). The dataset is created with the procedure described in Hurrell et al. [2008] and merges the HadISST observational dataset (since 1870) to the more recent NOAA-OI (since 1981). EC-Earth reads the SST and SIC as mid-month boundary conditions, which are then interpolated daily in the model run.

In this configuration, the atmospheric model IFS is characterized by a horizontal resolution of approximately 80 km and uses 91 vertical layers [Döscher et al., 2021].

Spectrally resolved OLR radiances are not provided by GCMs outputs. In the case of EC-Earth, we extracted spectral radiances by implementing the  $\sigma$ -IASI RTM [Amato et al., 2002] inside the COSP module (v 1.4.1), a simulator package capable of mapping the state of the climate model into synthetic observations that are directly comparable to the measurements of the real instruments [Bodas-Salcedo et al., 2011].

The current version of COSP implemented in EC-Earth includes simulators for passive sensors such as MODIS and MISR and active sensors like CALIOP. It also provides a simulator of the International Satellite Cloud Climatology Project (ISCCP) dataset, a simulator of the observation products of CLOUDSAT and an interface for an old version (v. 9.1) of the Radiative Transfer for Television and Infrared Observation Satellite (TIROS) Operational Vertical Sounder (RTTOV), which can be linked to the package (see Figure 4.2).

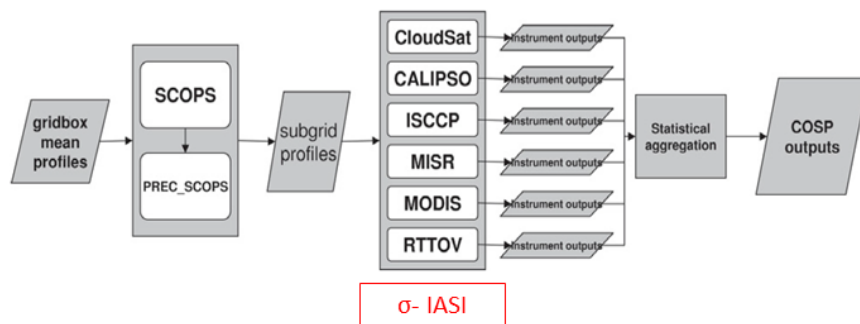


Figure 4.2: COSP scheme from [Bodas-Salcedo et al., 2011]

### 4.1.2 Implementation of the $\sigma$ -IASI RTM in the EC-Earth climate model

We created a specific GCM-RTM interface inside the COSP module of the EC-Earth climate model to perform radiative transfer calculations *online*, i.e., by passing instantaneous atmospheric fields on a global scale to the RTM with a time step of 6 hours.

In the radiative scheme of IFS, the spectral emissivity of the surface is assumed to be constant and equal to 0.99 outside the atmospheric window region (800 - 1250  $\text{cm}^{-1}$ ). Conversely, within this region the emissivity depends on 8 types of surface: open sea, sea ice, interception layer, low and high vegetation, exposed and shaded snow and bare ground. These emissivity values are interpolated into a regular wavenumber grid with steps of 10  $\text{cm}^{-1}$ , in the range from 100 to 3000  $\text{cm}^{-1}$  and supplied to the  $\sigma$ -IASI RTM. The surface pressure and surface temperature are supplied directly to  $\sigma$ -IASI, while the simulated temperature, humidity and gases concentration profiles are first interpolated into the fixed pressure grid used by  $\sigma$ -IASI. Carbon dioxide, methane and nitrous oxide concentrations are assumed horizontally and vertically uniform, depending only on time. More in detail, the  $\text{CO}_2$ ,  $\text{CH}_4$ ,  $\text{N}_2\text{O}$ , concentrations used are the global and annual mean observed values (interpolated daily from one year to the other) provided by CMIP6 for the AMIP simulations and referenced in Meinshausen et al. [2017]. Finally, the ozone mixing ratio used in the model simulation is a function of pressure, latitude and time, as described in Fortuin and Langematz [1995]. The concentrations of the other trace gases required by  $\sigma$ -IASI ( $\text{SO}_2$ ,  $\text{CO}$ ,  $\text{HNO}_3$ ,  $\text{NH}_3$ ,  $\text{OCS}$ ,  $\text{HDO}$ ,  $\text{CF}_4$ ) are not modeled in the IFS, thus they are extracted from the U.S. Standard Atmosphere of the Atmospheric Constituent Profiles dataset [Anderson et al., 1986]. In order to minimize the huge impact of the radiative code on the GCM computing performance, the Look-Up Tables (LUTs) of optical depths parametrization coefficients are allocated and loaded from file only once at the beginning of the simulation, stored, and deallocated at the end of the process. Moreover, the outgoing radiance is computed only one every 4 latitude x longitude grid points of the EC-Earth model, for a total of about 6000 simulated spectra every 6 hours. To limit the data storage required, the high resolution spectrum computed by  $\sigma$ -IASI is convolved with a 10  $\text{cm}^{-1}$ -wide box function and sampled every 10  $\text{cm}^{-1}$ . Since EC-Earth does not include variables with a spectral dimension, we stored the simulated spectra in new auxiliary 4D variables declared in the IFS grib code scheme, using the dimension corresponding to

vertical model levels for the spectral channels. The implemented simplifications allowed to strongly reduce the computational cost of the model run, passing from an initial value of 90000 core hours per simulated year (CHPSY) to 4000 CHPSY, which is comparable to the cost of the other simulators already present in COSP and about 8 times higher than an EC-Earth standard atmosphere-only simulation without COSP (about 500 CHPSY).

### 4.1.3 ECE radiance climatology

The model was run with prescribed SSTs and SIC, using observed GHG concentrations, from January 2008 to December 2014. Strictly speaking, for the last 2 years (2015-16), we used the SSP2-4.5 scenario data [Meinshausen et al. \[2020\]](#), which, however, matches observations until 2017.

Due to the complication in comparing all-sky measurements at different resolutions, here we focus only on the clear-sky part, leaving the analysis of cloudy sky to a future work.

However, as described in section 2.2.1 of chapter 2, the radiative computation in clear-sky conditions in climate models exploits the same all-sky profiles (temperature, humidity, etc.). While in the CERES-EBAF 4.1 dataset, the adjustment factor  $\Delta$  is introduced to generate TOA clear-sky fluxes that are more in line with the clear-sky fluxes represented in climate models, in the EC-Earth vs. IASI comparison, to mitigate this problem, we select only the spectra computed over grid cells where the simulated total cloud cover is less than 30%.

This threshold allows to remove most humid grid cells, while ensuring a good global coverage. In particular, the threshold is the result of a trade-off between reducing the impact of this potential source of bias and keeping a significant number of measurements in the analysis. In principle, a lower threshold would be more desirable, but, at the same time, would reduce the statistics.

Furthermore, to save computing time, ECE simulates spectra in correspondence of only once every 4 latitude x longitude grid cells. The actual model cells for which the spectra are simulated are shown in Figure 4.3.

For each of these cells, we compute the monthly average radiance using only the simulated spectra with local solar time between 6 and 12 hours. The same conditions are used to build the IASI radiance climatology, in order to mitigate the potential bias deriving from the temporal mismatch of the simulated and observed radiances. We then compute the monthly zonal averages by averaging the monthly mean radiances relating to the model cells within the considered latitude belt. With this procedure, all model cells contribute to the zonal mean with equal weight.

## 4.2 Observations

The large amount of data available from sensors able to perform measurements of the Earth emission spectrum opened interesting perspectives for intercomparisons of instrumental measurements and long-term analysis. [Whitburn et al. \[2020\]](#) computed OLR spectral fluxes starting from IASI radiances, using precalculated angular distribution models (ADM), and compared IASI OLR integrated fluxes to CERES and AIRS broadband OLR products. In his later work, [Whitburn et al. \[2021\]](#) exploits ten years (2008-2017) of IASI data to evaluate linear trends in clear-sky spectrally resolved OLR. [Susskind](#)

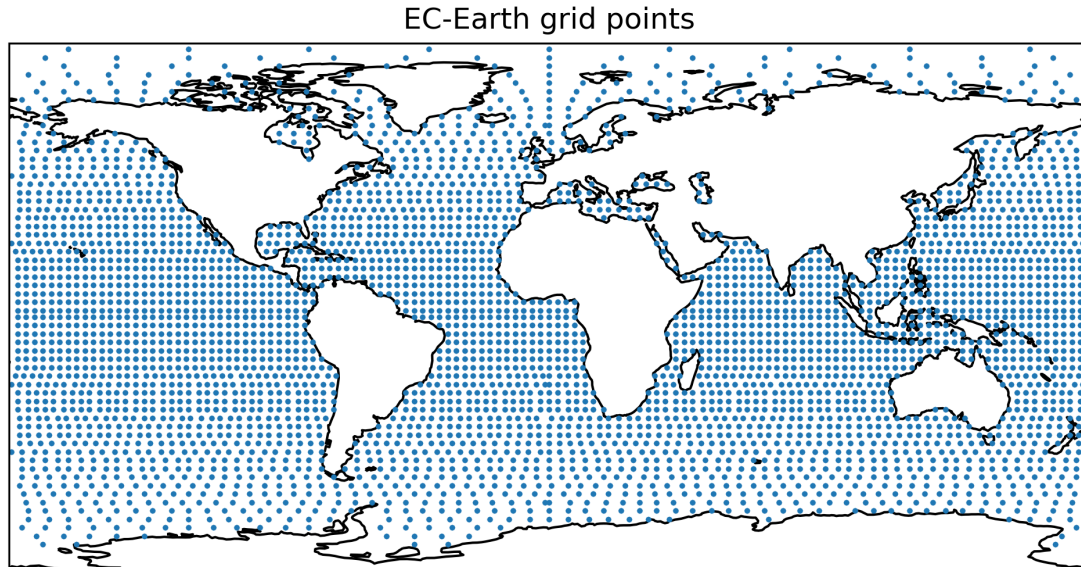


Figure 4.3: The dots indicate the center of the ECE model cells for which a spectral radiance is simulated.

et al. [2012] investigated the interannual variability of OLR using AIRS data from 2002 to 2011 and compared the energy fluxes computed from spectrally resolved radiances to CERES broadband fluxes. In the same framework, Brindley et al. [2015] explored the interannual variability of spectrally resolved radiances at different spatial scales using 5 years of IASI/MetOp-A data. While the aforementioned instruments are able to provide accurate measurements of the entire Mid-Infrared (MIR) portion of the spectrum, from  $667$  to  $2500$   $\text{cm}^{-1}$  ( $4 - 15$   $\mu\text{m}$ ), the Far-Infrared (FIR) spectral range, from  $100$  to  $667$   $\text{cm}^{-1}$  ( $15 - 100$   $\mu\text{m}$ ), which accounts for at least half of the Earth's energy emitted to space [Harries et al., 2008], still lacks of systematic measurements from satellite because of the intrinsic difficulties of development of the proper FIR technology [Palchetti et al., 2020]. Planned for launch in 2027, the Far-Infrared Outgoing Radiation and Monitoring (FORUM) mission will fill this observational gap.

### 4.2.1 Fourier Transform Spectrometer

IASI and FORUM sensors are Fourier Transform Spectrometers (FTS). The operating principle is that of the Michelson interferometer, as illustrated in Figure 4.4.

A source of monochromatic light crosses a semi-reflective mirror (beam splitter (BS)) and it is divided in two different beams that are reflected again by a movable mirror (M1) and a fixed mirror (M2), respectively. The two paths crossed by the lights have different lengths in order to produce a phase shift. The beams cross again the beam splitter and meet the detector R.

The intensity of a monochromatic source measured by the detector is:

$$I = E^2 \epsilon [1 + \cos(2\pi\sigma x)] \quad (4.1)$$

Where in equation 4.1  $E$  is the sum of the electric fields of the two beams,  $\epsilon$  is the

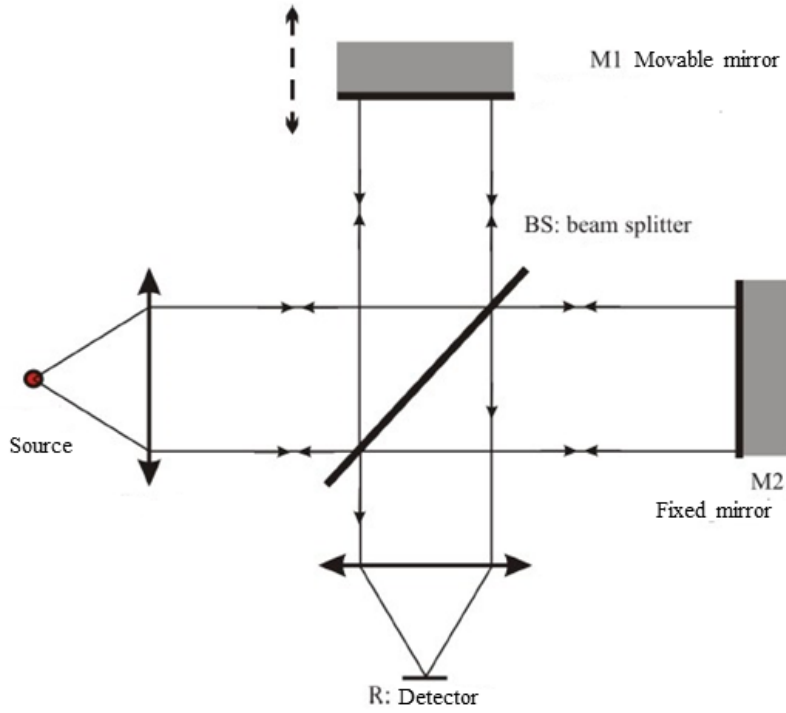


Figure 4.4: Optical layout of a Michelson interferometer

efficiency of the beam splitter,  $\sigma$  is the wavenumber and  $x$  is the optical path difference between the two beams.

When the source is not monochromatic and is characterized by a continuum spectral distribution  $B(\nu)$  we can define the relation:

$$dE^2(\sigma) = B(\sigma)d\sigma \quad (4.2)$$

We can now introduce the interferogram  $I$ , defined as:

$$dI = \epsilon B(\sigma) \cos(2\pi\sigma x)d\sigma \quad (4.3)$$

Thus, the total interferogram is obtained by an integration over the wavenumber  $\sigma$ :

$$I(x) = \int_0^{+\infty} \epsilon B(\sigma) \cos(2\pi\sigma x)d\sigma \quad (4.4)$$

The spectrum  $B(\sigma)$  is obtained from the inverse Fourier transform of 4.4 :

$$B(\sigma) = \int_{-\infty}^{+\infty} I(x) \cos(2\pi\sigma x)dx \quad (4.5)$$

This solution is based on the assumption that the optical path difference between the beams, that is to say the distance covered by the movable mirror, can be infinite. But,

## Chapter 4. The contribution of IASI observed radiances to the detection of EC-Earth climate model biases

in a real case,  $x \in (-L, +L)$ , where  $L$  is the Maximum Optical Path Difference (MOPD) for which the interferogram has been measured.

The truncation of this integral is equivalent to multiplying the integral in 4.5 by a function  $F(x) = 1$  for  $x \in (-L, +L)$  and 0 elsewhere.

Based on the properties of Fourier transform, this operation is equivalent to convolute the spectrum obtained from the interferogram with the "sinc" function:

$$B'(\sigma) = B(\sigma) * \text{sinc}(2\pi\sigma L) \quad (4.6)$$

A graph of the function  $\text{sinc}(y) \equiv \sin(y)/y$ , also called instrument response function (or instrument line-shape) is shown in Fig. 4.5. The first intersection of the function with

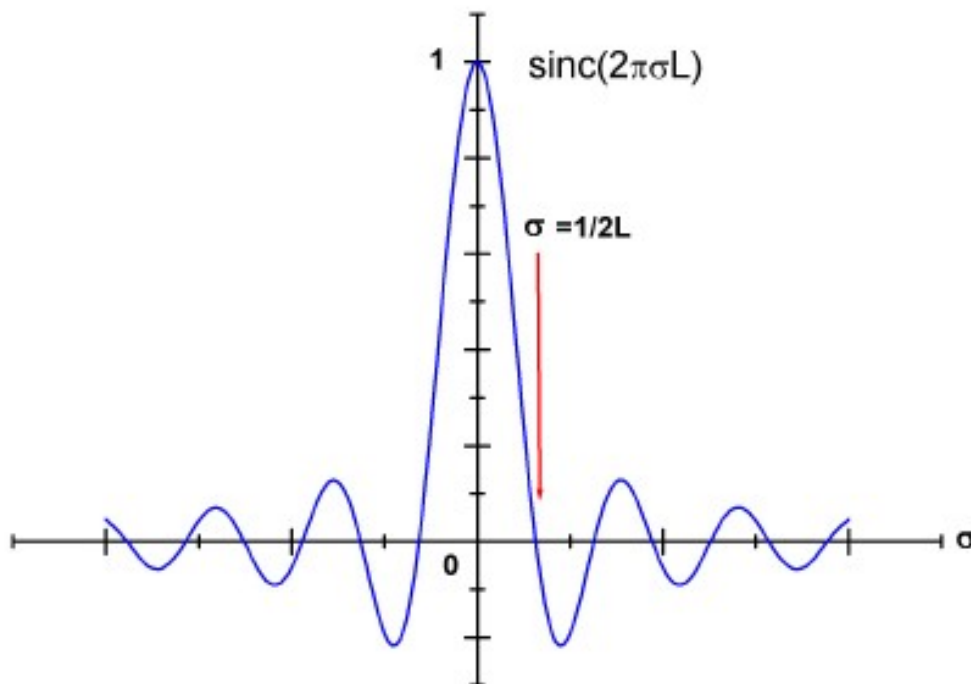


Figure 4.5: Sinc function

the x-axis in  $\sigma = 1/2L$  provides the *spectral resolution* of the instrument.

### IASI

Part of the payload of the MetOp series of EUMETSAT polar-orbiting meteorological satellites [Edwards and Pawlak, 2000], IASI is composed of the FTS and of an associated Integrated Imaging Subsystem (IIS), a broadband radiometer with a high spatial resolution for the co-registration with the Advanced Very-High-Resolution Radiometer (AVHRR) [Blumstein et al., 2004]. MetOp is characterized by a sun-synchronous orbit with equatorial crossing time at 9:30 a.m. and 21:30 p.m. local times. IASI has been providing continuous data since October 2006, when it was firstly launched aboard MetOp-A. It was followed by IASI-B (MetOp-B), launched in 2012 and IASI-C (MetOp-C), launched in 2018.

All the three instruments (A, B and C) cover the spectral range from  $645$  to  $2760\text{ cm}^{-1}$ , with a spectral resolution of  $0.5\text{ cm}^{-1}$  and a spectral sampling of  $0.25\text{ cm}^{-1}$ , for a total of  $8461$  spectral channels. In order to obtain a uniform global coverage, IASI acquires measurements by scanning its Field of Regard (FOR) across the orbit track, with viewing angles that range from nadir up to  $48.3$  degrees on either side of the satellite track. Angularly, each FOR has a dimension of about  $3.3^\circ \times 3.3^\circ$ , which, on ground, corresponds to a footprint of about  $50 \times 50\text{ km}$  at nadir. For each FOR (30 in total for scan) the instrument simultaneously acquires 4 spectra, each with a Field of View (FOV) of about  $12\text{ km}$  of diameter at nadir.

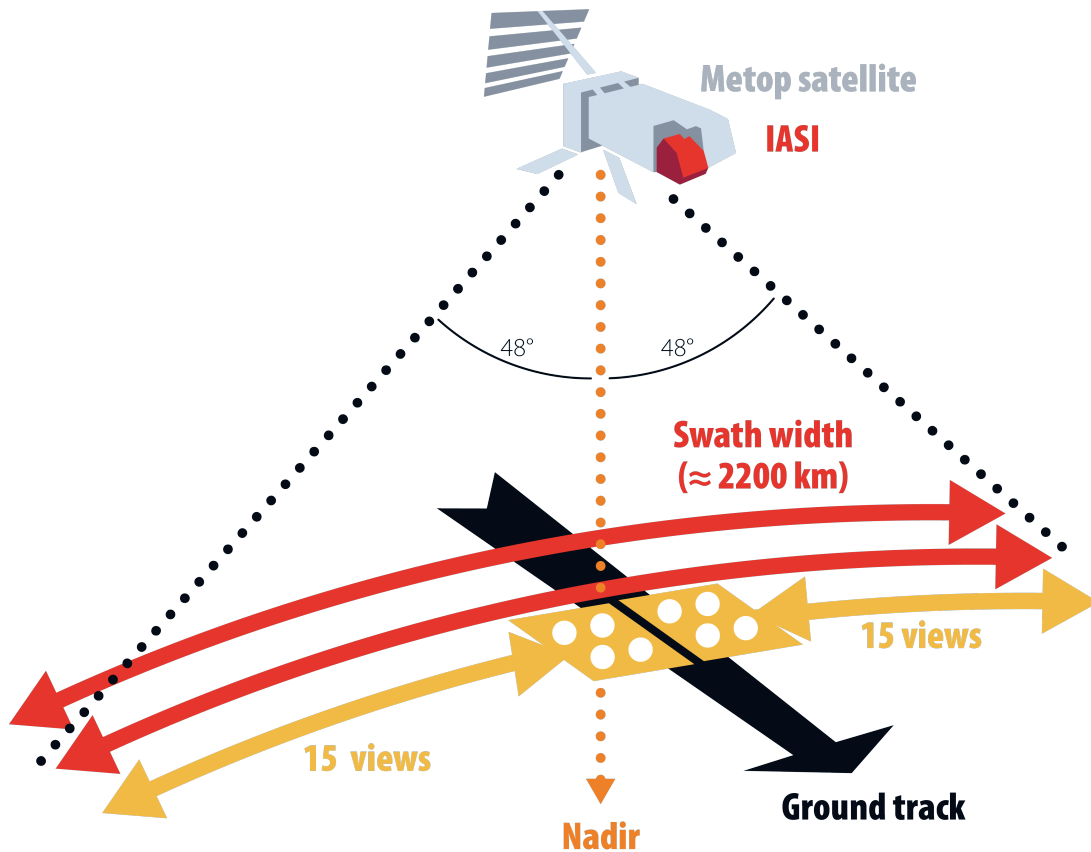


Figure 4.6: IASI trace and geometry from [Clerbaux et al., 2009]

In the next years, the continuity of the IASI mission will be guaranteed by the new generation of IASI (IASI-NG). This sensor will be characterized by the same features of the previous IASI instruments, but with an improved spectral resolution of  $0.25\text{ cm}^{-1}$  and a spectral sampling of  $0.125\text{ cm}^{-1}$ . Furthermore, since FORUM will fly in loose formation with IASI-NG, thus, for the first time from space, the two instruments will cover the whole Earth's emission spectrum [Ridolfi et al., 2020].

### 4.2.2 CERES

In this work, we exploit the *CERES – SYN1deg – Ed4A* products ([https://doi.org/10.5067/TERRA+AQUA/CERES/SYN1DEG-1HOUR\\_L3.004A](https://doi.org/10.5067/TERRA+AQUA/CERES/SYN1DEG-1HOUR_L3.004A)) to get information about the observed cloud cover field on a global scale. Among the various products, the

## Chapter 4. The contribution of IASI observed radiances to the detection of EC-Earth climate model biases

---

dataset provides  $1^\circ$ -regional 3-hourly cloud coverage derived from MODIS and geostationary satellites.

The high temporal resolution of the product allows to easily find coincidences with IASI measurements and to analyze the large-scale atmospheric conditions where the IASI spectrum has been detected. As discussed in Section 4.3.1, this is useful for the analysis, since CERES data refer to an area ( $1^\circ \times 1^\circ$ ) of extension similar to the EC-Earth atmospheric resolution ( $0.7^\circ \times 0.7^\circ$ ). We also use the CERES Energy Budget and Filled (EBAF) dataset v.4.1 to estimate the observed clear-sky broadband fluxes.

### 4.2.3 IASI radiance climatology

In this work, we consider IASI data from the Fundamental Climate Data Record (FCDR) of reprocessed Metop-A Level 1c product (*DOI* : 10.15770/EUM\_SEC\_CLM\_0014), provided by EUMETSAT through the European Weather Cloud (EWC) service. On the basis of this dataset, which is homogeneous and validated over the whole selected time period (2008-2016), we build a monthly clear-sky radiance climatology on a global scale.

First, we use the quality flag (variable *GQisFlagQual*) available in the dataset to discard corrupted spectra. Then, among the 120 observed spectra of each scan across the satellite track, we only select those corresponding to the 8 pixels closest to the nadir view. Thus, the clear-sky spectra are detected by exploiting the cloud cover derived from the AVHRR (variable *GEUMAVHRR1BCLDFRAC* and *GEUMAvhrr1BQual*) [Guidard et al., 2011]. In the same way, we distinguish the land / ocean surface through the information (variable *GEUMAvhrr1BLandFrac*) provided by the AVHRR.

IASI measured spectra are selected from  $2^\circ \times 2^\circ$  cells centered on the ECE model cells for which spectra are simulated (Figure 4.3). On the one hand, the dimension of these cells is large enough to allow the selection of a sufficiently large number of IASI spectra. On the other hand, these cells do not overlap each other, thus each IASI measurement contributes only once to the statistics. For each of these cells, we compute the monthly average radiance using IASI measured spectra that meet the following conditions:

- The radiance is measured in day-time, in the near-nadir geometry, over the ocean, and corresponds to clear-sky conditions (cloud mask of AVHRR = 0).
- The measured radiance falls into a CERES grid cell, measured within 3 hours from the IASI observation time, with cloud cover less than 30 %. Since CERES grid cells have a dimension of  $1 \times 1$  degree, similar to the ECE model cells, applying the same threshold to the cloud cover we ensure consistency of the atmospheric conditions between model and observations.

Finally, we compute the monthly zonal averages of observed radiances by averaging the monthly means obtained at the  $2^\circ \times 2^\circ$  cells falling within the selected latitude belt.

## 4.3 Results and Discussion

### 4.3.1 Model-Observation comparison strategy

While the model outputs are provided every 6 hours on a fixed grid, MetOp performs about 14 orbits per day and IASI ground track is at 9:30 AM (descending node) and PM (ascending node) at the equator.

As already discussed in the previous sections, in order to limit the time mismatch between model and satellite measurements, we limit the comparison to day-time and IASI observations performed during the descending node (9:30 Local Solar Time equator crossing) are compared to EC-Earth synthetic radiances provided between 6 and 12 local time.

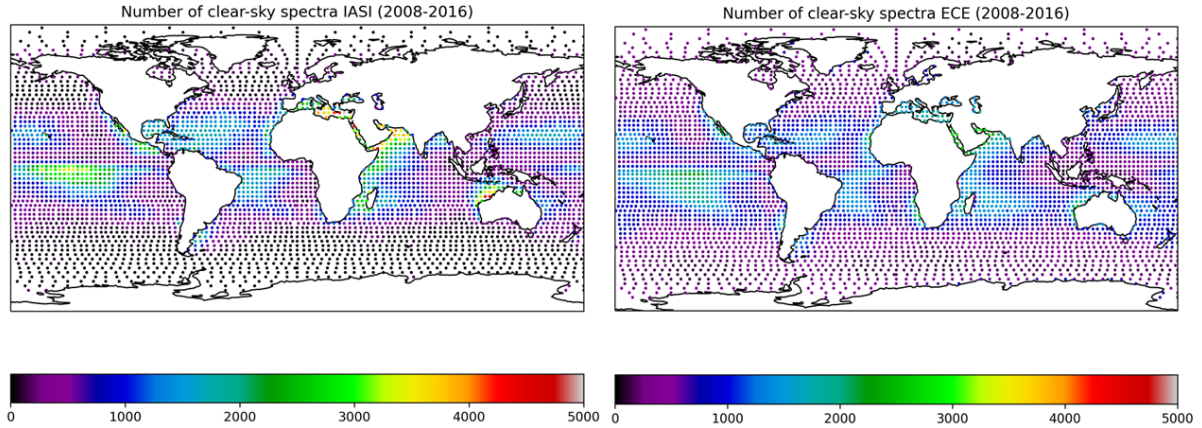


Figure 4.7: Number of observed (left) and simulated (right) spectral radiances that contribute to the clear-sky statistics, for each lat x long cell.

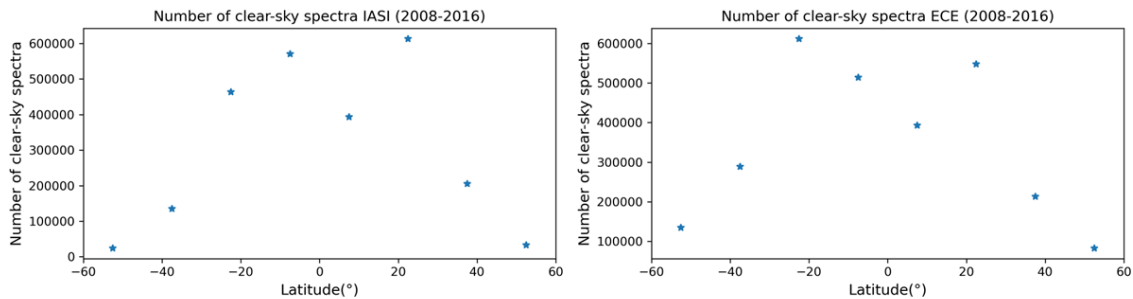


Figure 4.8: Number of observed (left) and simulated (right) spectral radiances that contribute to the clear-sky zonal means presented.

The left and right panels of Fig. 4.7 show, respectively, the number of measured and simulated spectra that meet the above specified conditions, in the time interval from 2008 to 2016.

As expected, the number of selected spectra is not homogeneously distributed across the globe. Indeed, most of the selected spectra are located in the subtropics ( $[15^{\circ}\text{-}30^{\circ}\text{ N}]$  and  $[15^{\circ}\text{-}30^{\circ}\text{ S}]$ ), corresponding to the descending branch of the Hadley Cell. However, the pattern of the number of selected spectra is very similar in simulations and measurements in the tropical and subtropical regions.

Note, however, that the filters used particularly affect the mid-latitudes ( $[45^{\circ}\text{-}60^{\circ}\text{ N}]$  and  $[45^{\circ}\text{-}60^{\circ}\text{ S}]$ ), where only few IASI pixels survive the selection process (see plots in

## Chapter 4. The contribution of IASI observed radiances to the detection of EC-Earth climate model biases

Fig 4.8). The small number of observations meeting the mentioned criteria could contribute to spurious biases at these latitudes. This is one of the reasons why we mostly focus our analysis on the tropical regions ( $[-30^\circ \text{ S } 30^\circ \text{ N}]$ ). In these regions the comparison method and the main results of the work are considered reliable.

For the sake of clarity, the following table describes the statistics of the clear-sky spectra used in the climatology for IASI and EC-Earth (Table 4.1). For each latitudinal band, the table shows the total number of grid cells (second column), the number of clear-sky grid cells with at least 1 measured or simulated spectrum per month (third and fourth columns) and the average number of spectra per month in these grid cells (fifth and sixth columns).

Lat Band	Tot gcells	N. of gcells (IASI)	N. of gcells (ECE)	N. of obs. (IASI)	N. of obs. (ECE)
60S – 45S	493	33	428	8	3
45S – 30S	506	147	495	9	5
30S – 15S	573	332	565	14	10
15S – 0S	497	317	457	17	10
0N – 15N	501	256	447	15	8
15N – 30N	491	320	477	18	10
30N – 45N	304	116	291	15	7
45N – 60N	221	34	198	9	4

Table 4.1: Statistics of the IASI and ECE spectra contained in the respective climatologies

In general, for IASI only a few grid cells per month have spectra at the highest latitudes. On the contrary, simulated spectra can be detected at almost all grid cells in a month. This difference can affect the comparison, especially at high and mid-latitudes, where the large difference in the number of available cells may represent a source of bias. On the other hand, in the tropical oceans this difference is smaller and the statistics tend to be similar (Table 4.1).

To check the sensitivity of our analysis, we also applied a threshold to select the minimum number of spectra in each grid cell. More in detail, we removed the grid cells containing less than 5 spectra per month, in order to eliminate from the comparison the grid cells with too few observations, which, as a consequence, could be not representative of the whole month.

Lat Band	Tot gcells	N. of gcells (IASI)	N. of gcells (ECE)	N. of obs. (IASI)	N. of obs. (ECE)
60S – 45S	493	15	41	16	7
45S – 30S	506	72	206	15	8
30S – 15S	573	220	439	19	12
15S – 0S	497	239	321	24	15
0N – 15N	501	171	247	22	13
15N – 30N	491	239	356	23	13
30N – 45N	304	74	139	25	11
45N – 60N	221	18	41	16	8

Table 4.2: Statistics of the IASI and ECE spectra contained in the respective climatologies after the application of the threshold

The statistics of the clear-sky spectra under this condition is shown in Table 4.2. The number of cells with at least 5 spectra per month (third column of the tables) appears strongly reduced, in particular in the model, since here we have an average of few spectra per month over most grid points.

Furthermore, we have verified that the application of the threshold does not affect the results of our analysis over tropical latitudes, where we focus our study. As a consequence, we have proceeded with the comparison performed without the application of the threshold.

### 4.3.2 Sensitivity of a simulated OLR spectrum to atmospheric temperature and gas concentrations

In order to better correlate the differences between modelled and observed radiances to model biases, we first studied, for a reference tropical atmosphere, the sensitivity of the radiance computed with  $\sigma$ -IASI to model temperature and trace species concentration.

Figure 4.9 shows a spectrum of OLR at the TOA simulated by  $\sigma$ -IASI in clear-sky conditions. The spectral ranges measured by IASI and FORUM are highlighted, together with the approximated spectral ranges of the atmospheric window regions and the main gas absorption bands, which are summarised in table 4.3.

The FIR region (from 100 - 667  $\text{cm}^{-1}$ ) is dominated by the signature of the rotational band of water vapour (blue shade), whose study will be consolidated with the help of future FORUM measurements [Brindley and Harries, 1998]. In anticipation of FORUM measurements, we focus here on the MIR region of the spectrum measured by IASI (645 - 2760  $\text{cm}^{-1}$ ) from 2006 onward. In this region, the spectrum undergoes a strong absorption between 640 - 750  $\text{cm}^{-1}$  due to  $\text{CO}_2$ . In more detail, in the core of  $\text{CO}_2$  band (centered at 660  $\text{cm}^{-1}$ ), the atmosphere appears opaque from space and the radiance reaching TOA is originated from the stratosphere. On the contrary, in the wing of the  $\text{CO}_2$  band measured by IASI (700 - 750  $\text{cm}^{-1}$ ), the effective emission level is located in the middle- to upper-troposphere. From 800 to 950  $\text{cm}^{-1}$  and from 1100 to 1250  $\text{cm}^{-1}$  (red shades), the atmosphere is almost transparent and the radiance reaching the TOA mainly originates from the surface or the atmospheric layers closest to the surface. Other strong absorption bands are located between 980 and 1080  $\text{cm}^{-1}$  (ozone, green shade), between 1200 and 1400  $\text{cm}^{-1}$  (methane, pink shade) and between 1250 and 1350  $\text{cm}^{-1}$  (nitrous oxide, grey shade). Finally, the roto-vibrational water vapour band, located between 1400 and 1850  $\text{cm}^{-1}$ , is highlighted.

Acronym	Band Details	Spectral Range ( $\text{cm}^{-1}$ )
WV1	Water vapour (1)	100 - 500
$\text{CO}_2$	Carbon Dioxide	640 - 750
AW1	Atmospheric Window (1)	800 - 950
$\text{O}_3$	Ozone	980 - 1080
AW2	Atmospheric Window (2)	1100 - 1250
$\text{CH}_4$	Methane	1200 - 1400
$\text{N}_2\text{O}$	Nitrous Oxide	1250 - 1350
WV2	Water vapour (2)	1400 - 1850

Table 4.3: Approximated spectral intervals of the atmospheric windows and the main absorption bands highlighted in Fig. 4.9.

The radiance reaching TOA originates mainly from upper atmospheric layers in the spectral regions of strong absorption, while in more transparent regions it originates from

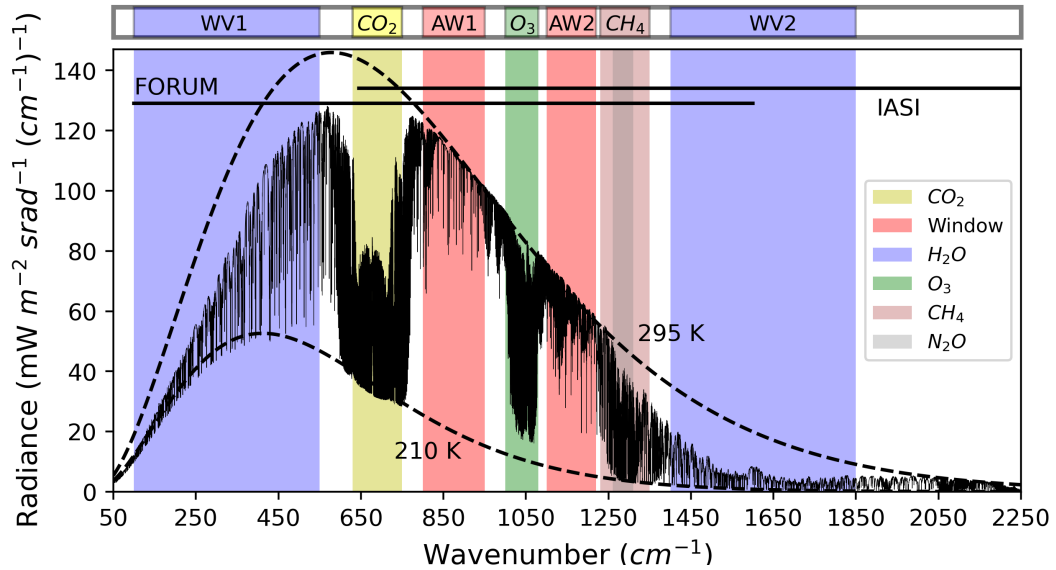


Figure 4.9: Spectrum simulated in clear-sky conditions over tropical ocean by the  $\sigma$ -IASI RTM. The main absorption bands are highlighted. Dashed lines show the equivalent blackbody emission at typical surface (295 K) and tropopause (210 K) temperatures.

the lower atmospheric layers. More accurate information on the atmospheric layers contributing to the observed OLR spectrum can be extracted from the analysis of the Jacobians, defined as the partial derivatives of radiance with respect to the most relevant atmospheric parameters. The Jacobians in Figure 4.10 are computed with the  $\sigma$ -IASI RTM for a tropical standard atmosphere over ocean at the IASI sampling of  $0.25 \text{ cm}^{-1}$  from 10 to  $2250 \text{ cm}^{-1}$ . For a better readability of the graph, the Jacobian values shown are the absolute values normalized to the maximum value for each quantity, separately.

As we can see from Figure 4.10, the entire spectrum is sensitive to the temperature profile (red areas):

- the atmospheric window *AW1* is more transparent than the atmospheric window *AW2*, where the radiation is slightly sensitive to the water vapour concentration. In the first case (*AW1*), the radiation is affected by the temperature of atmospheric layers between 0 and 3 km while, in the second one (*AW2*), it is controlled by the temperature of layers at greater heights, up to about 7 km;
- the FIR is strongly affected by the temperature of lower and medium troposphere [3 - 10 km];
- the  $\text{CO}_2$  absorption band is mainly sensitive to stratospheric temperature [25 - 40 km] in the core of the band and to mid-to-upper tropospheric temperature [5 - 20 km] in the wing of the band;
- the  $\text{O}_3$  band is affected by surface, lower troposphere and lower stratosphere temperature;
- the roto-vibrational band of water vapour *WV2* is sensitive to tropospheric temperature [5 - 10 km].

Specific features can be noticed for each gas:

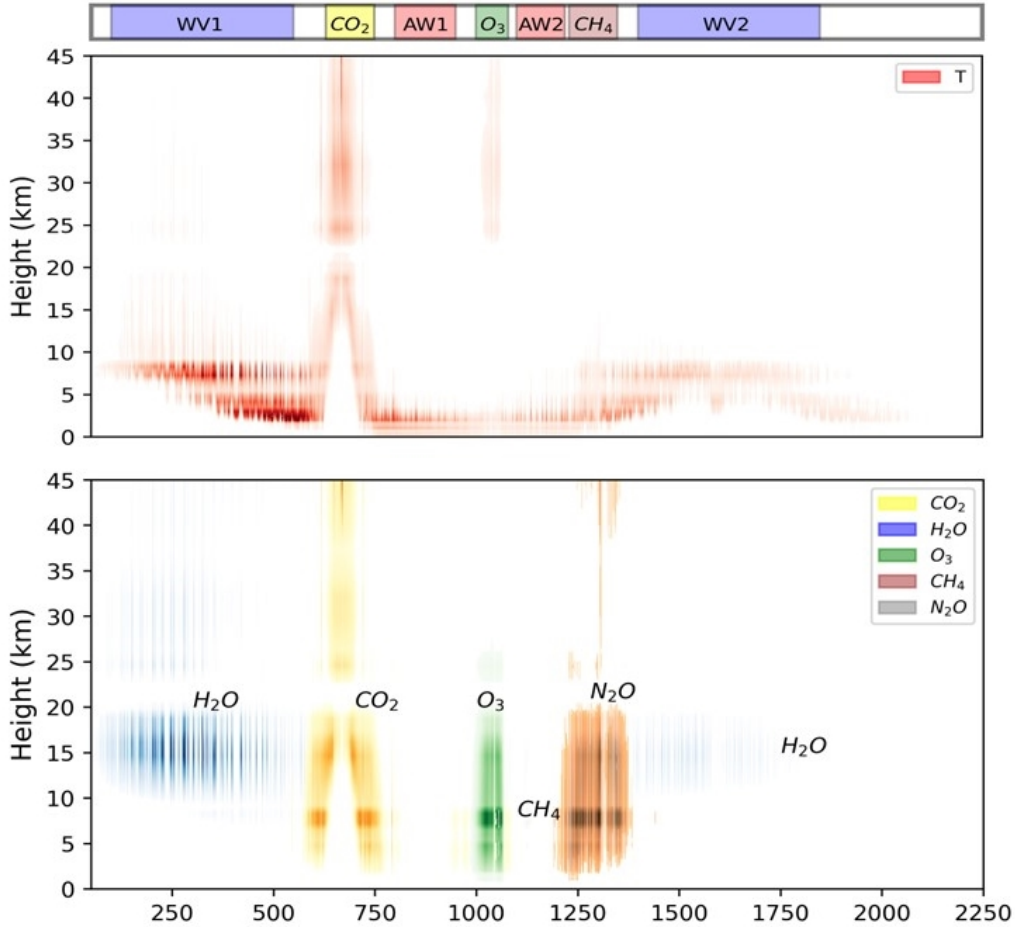


Figure 4.10: Absolute values of normalized Jacobians computed with  $\sigma$ -IASI for a tropical standard atmosphere with respect to the temperature (top panel) and gases concentration (bottom panel).

- the outgoing radiance between  $1400$  and  $1850\text{ cm}^{-1}$  (*WV2*) is attenuated by  $\text{H}_2\text{O}$  in the upper troposphere (blue area) from  $10$  to  $20$  km. Water vapour also reduces OLR in the FIR region (*WV1*);
- between  $980$  and  $1080\text{ cm}^{-1}$ , the ozone concentration strongly influences the spectrum over most of the troposphere (green area);
- at the same levels, the spectrum is affected by  $\text{CH}_4$  concentration between  $1200$  and  $1400\text{ cm}^{-1}$  and by  $\text{N}_2\text{O}$  between  $1250$  and  $1350\text{ cm}^{-1}$ ;
- in the  $\text{CO}_2$  band, the spectrum is sensitive to  $\text{CO}_2$  concentration at the same height where it is particularly sensitive to temperature profile. Thus, it is influenced by  $\text{CO}_2$  concentration in the stratosphere in the core of the band while in the wings of the band it is sensitive to  $\text{CO}_2$  present in the troposphere.

A change of sign of the Jacobian is observed for all gases between troposphere and stratosphere (not shown). In fact, in the troposphere absorption processes dominate the

## Chapter 4. The contribution of IASI observed radiances to the detection of EC-Earth climate model biases

---

emission ones (so increased concentration reduces the OLR), while the opposite happens in the stratosphere.

### 4.3.3 Assessment of EC-Earth biases in simulated clear-sky radiances with respect to IASI measurements

On the basis of these assumptions, a systematic comparison has been performed using a dataset that covers the years from 2008 to 2016, for latitudes ranging from 60°S to 60°N. Land and ocean surface cases were analyzed separately, however, here we focus only on the ocean cases. In fact, the low temporal sampling of the model (the RTM is called every 6 hours) and the uncertainties in the land surface emissivity do not allow to perform accurate comparisons between measured and observed radiances over land. In general, over land, the model shows a strong negative bias with respect to day-time measurements, and an important positive bias in night-time cases. Considering all-day measurements and simulations, a negative difference of about 3 K in brightness temperature persists in the atmospheric window between model and observations, pointing at a cold model bias of land surface temperature. Due to the significant differences in the atmospheric window, here we do not speculate on the results of the intercomparisons over land. We rather focus on the comparison of daytime measurements and model outputs over ocean.

Figure 4.11 shows the 9 years average of Brightness Temperature (BT) differences (model - observations) over the ocean. Considering that model SSTs are constrained to be equal to the observed values, we expect small differences between model and IASI spectral radiances in the atmospheric spectral windows (*AW1*, *AW2*). Thus, the limited discrepancies in BTs obtained in the spectral window *AW1* in the tropical belt [30° S, 30° N] confirm the self-consistency of the comparison performed. Instead, as mentioned in Sect. 4.3.2, the atmospheric window *AW2* is more sensitive to the presence of water vapour and shows a small positive bias. At mid latitudes, however, especially in the southern hemisphere, a negative model bias is present in both the atmospheric windows, thus making difficult the comparison at all the frequencies at these latitudes. This model bias is thought to be due to the difference in the number of points selected for ECE and IASI and affected by the cloud cover representation in the model, as further discussed in Sect. 4.3.6.

Significant discrepancies, of about 3.5 K, are present in the CO<sub>2</sub> band at all latitudes, which might indicate a warm bias in the model temperature of the upper-troposphere and stratosphere. A warm bias is also seen in the roto-vibrational water vapour band (*WV2*), but this is limited to the tropical latitudinal belt, between 30°S and 30°N.

In a similar way, the bias visible in the O<sub>3</sub> band is strictly dependent on latitude and is characterised by a positive sign at the tropics, while it tends to take negative values at mid latitudes. As described in Sect. 4.3.2, this spectral band is affected by surface, lower troposphere and stratospheric temperatures.

On the basis of the above considerations, we focus our analysis on the discrepancies found over tropical ocean where the BT differences in the atmospheric windows are close to zero.

Figure 4.12 shows the 2008-2016 average of model simulated and observed BTs (equation 1.3) over ocean, at tropical latitudes [30° S, 30°N] (top panels) and their differences (bottom panels). In this case we see that the model is generally in good agreement with the observations and the most significant discrepancies are found in the CO<sub>2</sub> band, in the

O<sub>3</sub> band and along the water vapour absorption band (*WV2*).

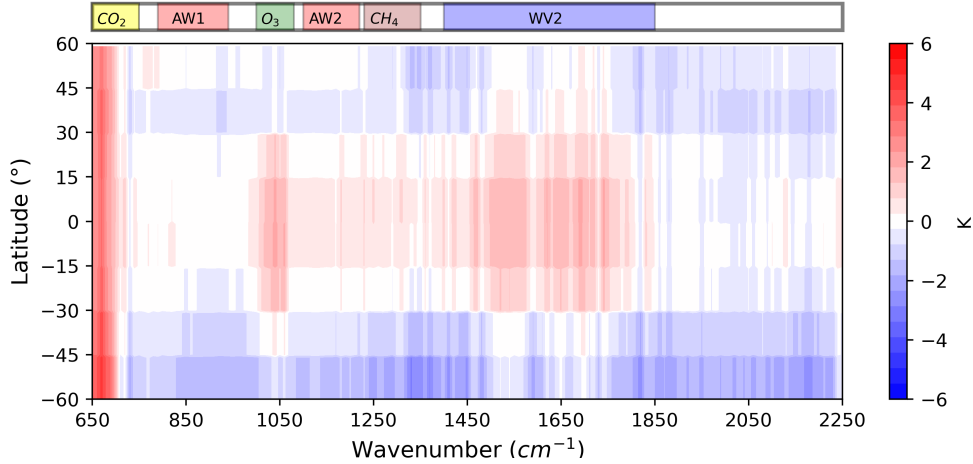


Figure 4.11: Brightness Temperature differences (model - observations) over ocean, averaged over the period 2008 - 2016

For the same period, the average clear-sky OLR flux computed by EC-Earth over ocean, between the latitudes 30°S and 30°N is equal to  $288.47 \pm 0.34 \text{ Wm}^{-2}$ . This is slightly overestimated compared to the analogous average clear-sky flux obtained from CERES observations, that is equal to  $287.36 \pm 0.32 \text{ Wm}^{-2}$ . From the Stefan-Boltzmann law, considering the power radiated by a black body at the temperature of 295 K (about the average surface temperature of tropical ocean), a difference of  $1 \text{ Wm}^{-2}$  corresponds to a BT difference of about 0.2 K, i.e. smaller than the biases localized in specific wavenumber ranges that we found from the spectral analysis.

To date, systematic FIR spectral radiance measurements from space are not yet available, thus we are not able to characterize the discrepancies between model and observations in the whole OLR spectral range. Despite that, the analysis presented shows clearly that a good agreement between simulated and observed total OLR fluxes may be obtained from the cancellation of opposite-in-sign systematic errors, localized in specific spectral ranges. In conclusion, observations of spectrally resolved OLR fluxes from space are needed for a proper tuning of model parameters.

#### 4.3.4 Temperature biases

It is possible to characterise the height dependence of the model temperature bias by focusing the analysis on specific spectral bands, that are sensitive to the atmospheric temperature at different heights.

Figure 4.13 shows the 9-years monthly averages of simulated and observed BTs over ocean in four spectral intervals together with the respective temperature Jacobians, which highlight the atmospheric levels to which the spectrum is most sensitive to the temperature.

The largest sensitivity to temperature in the stratosphere is found in the spectral interval centered at  $660 \text{ cm}^{-1}$  (panel A), while the channel at  $700 \text{ cm}^{-1}$  is sensitive to temperature in the upper troposphere and stratosphere (panel B). The maximum sensitivity to temperature in the mid-troposphere is reached in the spectral interval centered at  $730 \text{ cm}^{-1}$ . Finally, as usual, the spectral channels in the atmospheric window, in this

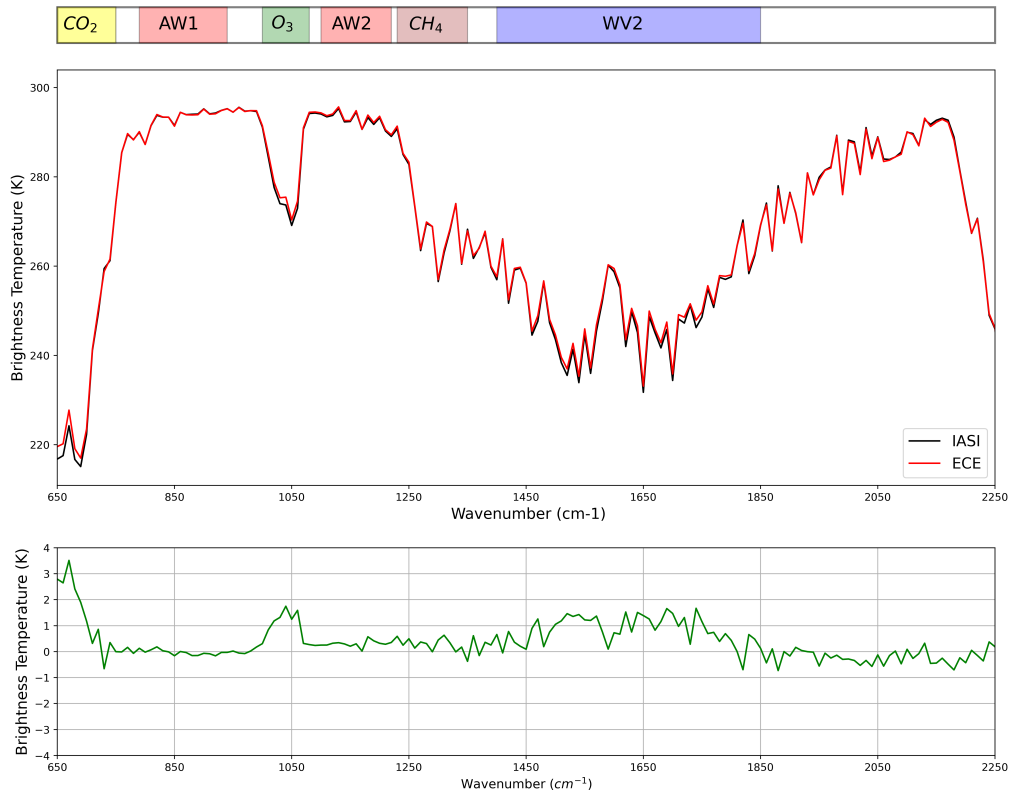


Figure 4.12: Average (2008-2016) Brightness Temperatures computed by EC-Earth and measured by IASI over the tropical ocean [30° S, 30°N] (top panel). The bottom panel shows the BT differences model minus observation.

case averaged between 845 and 855  $\text{cm}^{-1}$ , are a proxy of the lower troposphere and surface temperature. As already mentioned, the spectral intervals centered at 660  $\text{cm}^{-1}$ , 700  $\text{cm}^{-1}$  and 730  $\text{cm}^{-1}$  are not only sensitive to temperature but also to  $\text{CO}_2$  concentration. The model, however, uses  $\text{CO}_2$  global average concentrations smoothly increasing with time according to the actual measurements, thus any uniform warm model bias cannot be attributed to an erroneous carbon dioxide concentrations (see Section 4.1.1). The regional and seasonal variabilities of  $\text{CO}_2$  concentrations amount at most to a few ppm, causing only small local seasonal biases.

Therefore, panel A of Figure 4.13 confirms the presence of a strong stratospheric warm bias in the model. The more we move towards the lower layers of the atmosphere (panels A and B of Fig. 4.13), the more the bias is reduced, until its sign reverses in the spectral band centered at 730  $\text{cm}^{-1}$  (see panel C), which is sensitive to the mid-tropospheric temperature. Finally, as expected, the bias is very small in the atmospheric window over ocean (panel D). A more peaked seasonality is present in the ECE curve, which is however within the standard deviation of the two curves. BT differences between ECE and IASI in the spectral intervals of Figure 4.13 are also shown on a global scale in Figure 4.14. From these plots, it is evident that the biases are homogeneous over the tropical and subtropical latitudes, where we are comparing the simulated and observed BT. Some spatial compensating biases are only present at 850  $\text{cm}^{-1}$ , in the atmospheric window.

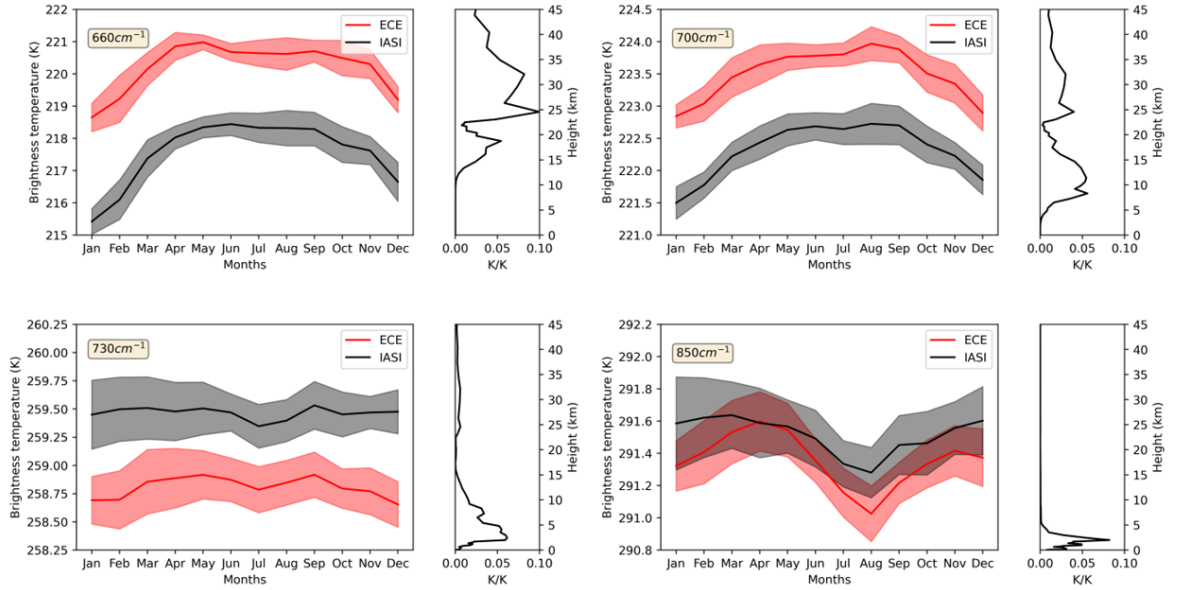


Figure 4.13: Brightness Temperature (BT) averaged in different spectral intervals over tropical ocean [30° S, 30°N]. The red line identifies the model BT while the black line describes the observed BT. The shadow areas represent the standard deviations. Note the different vertical scales used in the plots. On the right, the integrated jacobians of the temperature in the respective spectral bands.

However, these differences are generally very small, always within 1 K.

We further tested the results of the spectral analysis by comparing the temperature and humidity obtained from the climate model outputs with data provided by ERA5, the latest climate reanalysis from ECMWF. The reanalysis combines available data from different instruments (satellites, ships, weather stations etc.) with models, to generate a complete and continuous global coverage of the main geophysical variables [Hersbach et al., 2020]. The Figure 4.15 shows the temperature differences between EC-Earth and ERA5 reanalysis, averaged over 15 years (2000 - 2014). The strong warm bias in the stratosphere confirms the discrepancy found in our spectral analysis in the region at  $660\text{ cm}^{-1}$ . In the same way, we find an agreement of the small temperature bias found in the lower troposphere compared to the ERA5 reanalysis with the result highlighted at  $730\text{ cm}^{-1}$  (see panels C in Figures 4.13 and 4.14).

On the other hand, through the analysis of the band centered at  $700\text{ cm}^{-1}$  (see Panel B of Fig. 4.13), sensitive to the upper tropospheric temperature, we did not detect the cold model bias visible in Fig. 4.15 at the tropopause.

Actually, the result of our spectral analysis is not in contradiction with the outcome of the comparison with the ERA5 reanalysis. In fact, the spectral band at  $700\text{ cm}^{-1}$  (panel B of Fig. 4.13) is also partially affected by the positive stratospheric temperature bias, which can easily mask the underlying negative bias at the tropopause.

To prove the agreement, we inferred the BT bias from the temperature bias obtained from the comparison between the EC-Earth model and ERA5 (Figure 4.15).

Since we are performing this comparison over tropical latitudes, we computed the

## Chapter 4. The contribution of IASI observed radiances to the detection of EC-Earth climate model biases

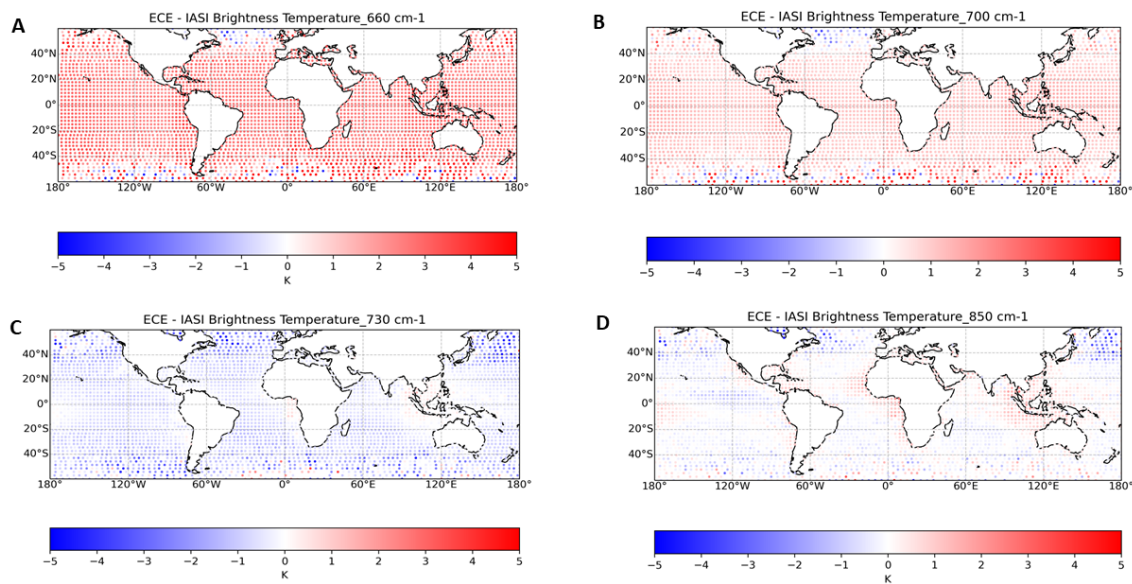


Figure 4.14: Brightness Temperature (BT) averaged in different spectral intervals over the globe [60° S, 60°N]

mean profile of these temperature biases along tropical latitudes [-30S, 30N]. Then, we performed the scalar product of these profiles with the respective Jacobians, computed from the profiles of a standard tropical atmosphere.

The result of this estimation is summarized in Table 4.4.

Spectral Channel( $\text{cm}^{-1}$ )	660	700	730	850
Most sensitive region to temperature (km)	[25-45]	[5-15] and [20-35]	[3-10]	[0-5]
BT bias - ERA5 (K)	+2.5	+0.8	-0.2	-0.2
BT bias - IASI (K)	+3.5	+1.5	-0.8	-0.2

Table 4.4: Inferred BT biases estimated from the comparison between climate model outputs and ERA5 data and from the comparison of climate model and IASI BT climatologies

The clear-sky BT biases found in the comparison with IASI are generally consistent with the estimates inferred here from the comparison with ERA5. Remarkably, the sign is consistent in all cases, although some differences are found in the magnitude. The spectral analysis indicates a stronger positive bias in the stratosphere ( $660 \text{ cm}^{-1}$ ) than inferred from ERA5. This is also seen in the spectral band at  $700 \text{ cm}^{-1}$ . In addition, we also have a more pronounced negative bias at  $730 \text{ cm}^{-1}$ , possibly produced by a larger negative temperature bias of the model in the middle troposphere. Finally, the BT biases for the spectral bands at  $850 \text{ cm}^{-1}$  show a very good agreement with the estimates obtained from the ERA5 reanalysis. It is important to note that the discrepancies between the BT biases, described in the last two rows of Table 4.4 may arise from different causes. First, the comparison of temperature and water vapour concentration profiles of Figure 4.15 is performed in all-sky conditions, while the spectral analysis reflects the differences

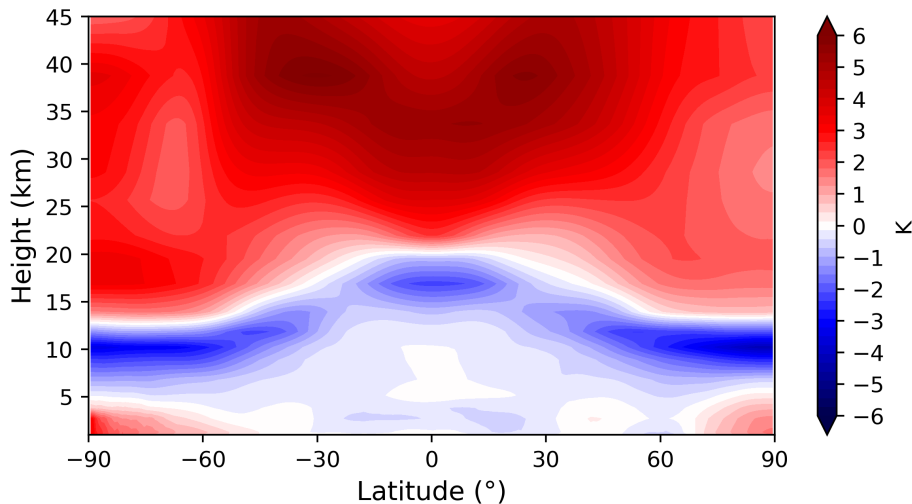


Figure 4.15: Differences between EC-Earth climate model and ERA5 reanalysis temperatures. Differences are a 15 years [2000 - 2014] average.

observed in clear-sky. Furthermore, the Jacobian used in the estimation of Table 4.4 is referred to a standard tropical atmosphere, on the basis of the dataset of Anderson et al. [1986], which may differ from the real one.

### 4.3.5 Water vapour biases

We now exploit the intervals  $725\text{-}735\text{ cm}^{-1}$  and  $1395\text{-}1405\text{ cm}^{-1}$  to explore the accuracy of the representation of the water vapour concentration in the model. In fact, as illustrated by the integrated Jacobians reported on the left panel of Fig. 4.16, the spectral band at  $1400\text{ cm}^{-1}$  (*WV2*) is sensitive both to the tropospheric temperature and to the upper tropospheric water vapour concentration. In both spectral intervals, the maximum sensitivity to temperature occurs between 3 and 10 km (green and pink lines on the left panel of Fig. 4.16). Since the previous analysis (panel C of Fig. 4.13) has shown a small negative BT bias at  $730\text{ cm}^{-1}$  assigned to a cold bias of the mid-tropospheric temperature in the model, if the water vapour concentration were well represented, we would see a negative BT bias in the spectral band  $1395\text{-}1405\text{ cm}^{-1}$ . However, since the model BT in the spectral interval centered at  $1400\text{ cm}^{-1}$  shows a slightly positive bias (Figure 4.16, right panel), we conclude that the negative temperature bias of the model seems to be over-compensated by a dry bias of the water vapour profile in the 7 - 15 km range. In fact, a too dry upper troposphere in the model allows more radiant energy to reach the TOA, as also witnessed by the negative sign of the water Jacobian shown on the left panel of Fig. 4.16.

As for the temperature, we compared our results with that obtained from the comparison with the ERA5 reanalysis (Figure 4.17).

Furthermore, to verify the consistency of the BT bias derived from our analysis, we inferred the BT bias obtained from the ERA5 water vapour biases.

The result of this estimation is summarized in Table 4.5.

The BT biases for the spectral bands at  $1400\text{ cm}^{-1}$  show a very good agreement with the estimates obtained from the ERA5 reanalysis. In both cases, the positive BT bias at

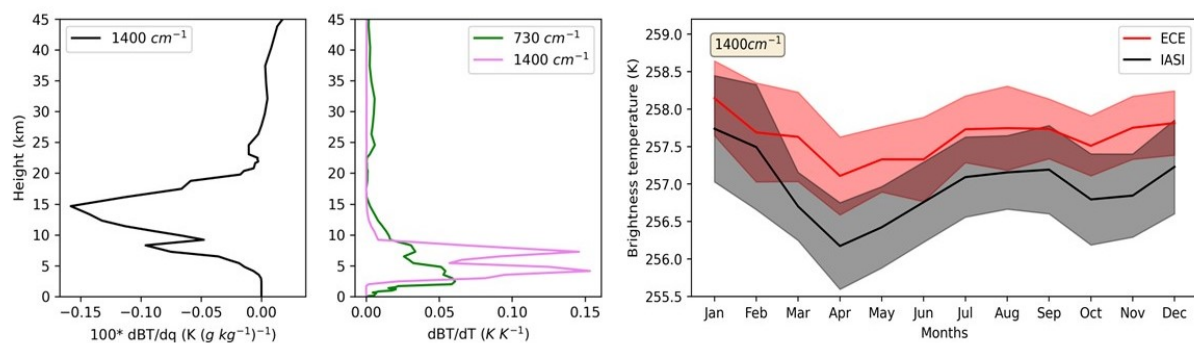


Figure 4.16: On the left, the integrated jacobians of the water vapour and temperature in the spectral bands 730 and 1400  $\text{cm}^{-1}$ . On the right, Brightness Temperature (BT) averaged at 1400  $\text{cm}^{-1}$  over tropical ocean [30° S, 30°N]. The red line identifies the model BT while the black line describes the observed BT. The shadow areas represent the standard deviations.

Spectral Channel( $\text{cm}^{-1}$ )	730	1400
Most sensitive region to temperature (km)	[3-10]	[3-10]
Most sensitive region to water vapour (km)	–	[5-20]
BT bias - ERA5 (K)	-0.2	+0.7
BT bias - IASI (K)	-0.8	+0.5

Table 4.5: Inferred BT biases estimated from the comparison between climate model outputs and ERA5 data and from the comparison of climate model and IASI BT climatologies

1400  $\text{cm}^{-1}$  may be interpreted as a negative bias of water vapour concentration in the upper troposphere of the model.

### 4.3.6 Discussion

We have seen that a perfect spatial and temporal matching of measurements and simulations is very difficult to actualise, therefore, systematic biases could also arise from the strategy adopted to sample the data. To evaluate the impact of the data sampling strategy, we carried out the following test. We interpolated the EC-Earth model cloud fraction and the measured CERES cloud fraction to a regular space grid of  $1^\circ \times 1^\circ$  and time step of 6 hours. Then, assuming alternatively the interpolated CERES and EC-Earth cloud fractions, we built the statistical distributions for the year 2008 of the same observed SST for the grid points with a cloud fraction less than 30 %. Figure 4.18 shows the SST statistical distributions obtained for EC-Earth and CERES cloud fractions, at tropical (left) and mid- (right) latitudes. At tropical latitudes the SST distributions obtained with the model (red boxes) and CERES (grey boxes) cloud fractions are quite similar: the average values differ by 0.4 K and the standard deviations ( $\approx 4.5$  K) differ by less than 0.1 K. On the other hand, at southern mid-latitudes ( $-60^\circ$  S,  $-45^\circ$  S, see the right panel of Fig. 4.18) the offset between the two distributions amounts to 0.9 K. The small

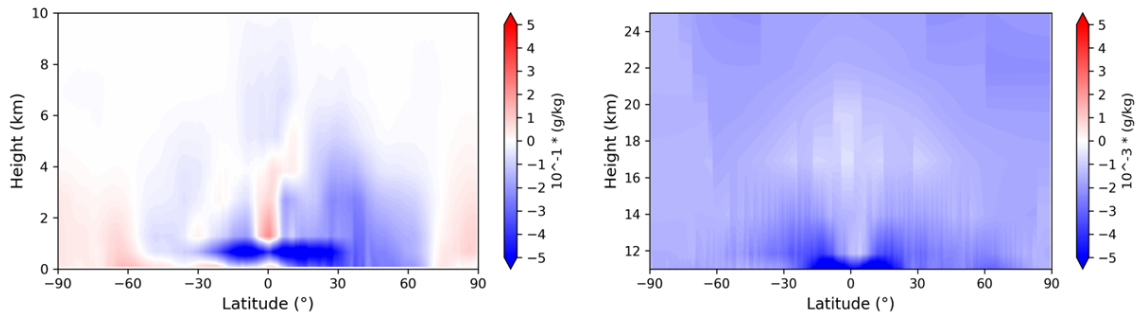


Figure 4.17: Differences between EC-Earth climate model and ERA5 water vapour concentration in the troposphere (left) and in the stratosphere (right). Differences are a 15 years [2000 - 2014] average.

bias at the tropics could be related to the differences in the seasonal cycle we observed in the BT of the atmospheric spectral window (panel D of Figure 4.13). The larger bias of 0.9 K at the southern mid-latitudes is likely contributing to the observed negative model BT bias found in the atmospheric window at the southern mid-latitudes in Figure 4.11. The good agreement between the two SST distributions found in the tropical latitude belt strengthens our confidence on the previous analyses we presented for tropical latitudes. At these latitudes, the choice of comparing model and measured climatologies corresponding to cloud fractions smaller than 30 % ensures that the biases introduced by the data sampling strategy is smaller than  $\approx 0.5$  K, i.e., also smaller than most of the model biases inferred from Fig. 4.13.

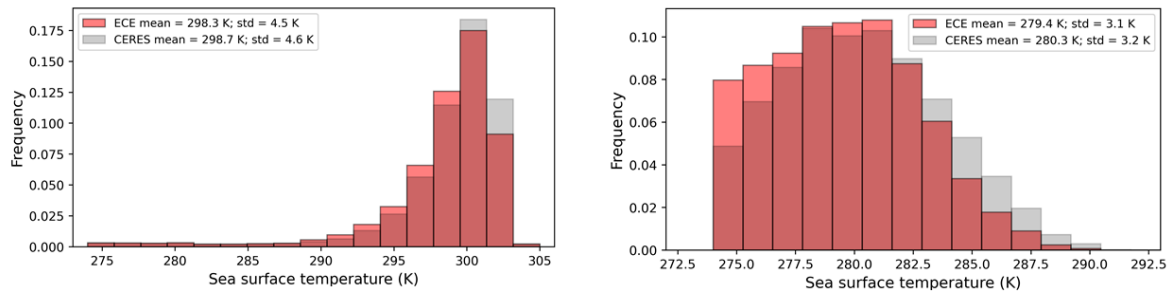


Figure 4.18: Distribution of sea surface temperature for cloud fraction  $< 30$  %, assuming the EC-Earth (red) or the CERES (grey) cloud fractions. The distributions were computed for tropical-  $[-30^{\circ}\text{S}, +30^{\circ}\text{N}]$  latitudes (left) and mid-  $[-60^{\circ}\text{S}, -45^{\circ}\text{S}]$  latitudes (right).

## 4.4 Conclusions

In this work, we implemented the  $\sigma$ -IASI RTM in the COSP package in order to perform on-line simulations of synthetic clear-sky spectra starting from the EC-Earth GCM profiles on a global scale with a time step of 6 hours for the period 2008-2016. Thus, we compared

## Chapter 4. The contribution of IASI observed radiances to the detection of EC-Earth climate model biases

---

the EC-Earth-simulated spectral radiances to the IASI-measured radiances built from the Fundamental Climate Data Record (FCDR) of reprocessed Metop-A Level 1c product on a frequency grid of  $10 \text{ cm}^{-1}$ . We limited the analysis to the clear-sky conditions identified by grid-points where the observed (CERES) and simulated (EC-Earth) cloud fraction is smaller than 30%. We found that such a small threshold limits the indirect effect of clouds on radiation in the model. The comparison has been firstly performed on a global scale ensuring spatial and temporal coincidence between the modeled and observed spectra. Then, we focused on the day-time tropical ocean  $[30^\circ \text{ S}, 30^\circ \text{ N}]$  area, where the analysis is not affected by the uncertainties due to the land emissivity and the discrepancies between observed and simulated radiances in the atmospheric window are close to zero.

The spectral analysis carried out in these conditions leads to the detection of the following EC-Earth model biases, which, due to compensations, do not show up in the comparison of the total OLR fluxes:

- A strong ( $\approx 3.5 \text{ K}$ ) positive temperature bias in the stratosphere.
- A small ( $\approx 1 \text{ K}$ ) negative temperature bias in the troposphere.
- A positive bias in the BTs in the water vapour band indicating an under-estimation of water vapour in the model in the upper troposphere.

Finally, the clear-sky BT biases found in the comparison with IASI are generally consistent with the estimates inferred here from the comparison with ERA5.



# 5

## Future perspectives

We have shown how the comparison of the OLR radiation of the EC-Earth model with spectrally resolved measurements has allowed to identify biases in the model in clear-sky conditions. The extension of this analysis in presence of clouds opens new possibilities of testing and improving climate modelling since the representation of clouds constitutes the greatest source of uncertainty in climate models. Here, we provide a possible approach to mitigate the prohibitive computational cost of simulating spectrally resolved radiances in all-sky conditions with the  $\text{COSP}+\sigma - \text{IASI}$  tool, implemented in the EC-Earth climate model. In addition, in the second part of this chapter, we calculate the linear trend of observed and synthetic clear-sky spectrally resolved radiances, over the period 2008-2016. Since OLR spectra contain the spectral signatures of the main climate variables, the calculation of spectral trends may allow to directly infer specific climate feedbacks from observations.

### 5.1 Towards the EC-Earth-IASI comparison in all-sky conditions

In Section 1.3.3 we have described how the radiative transfer scheme of the EC-Earth climate model relies on subcolumns generators to represent the sub-grid structure of clouds and improve the simulation of radiative fluxes. Indeed, the subcolumns generator stochastically provides sub-grid profiles of the cloud cover, ice and water cloud content. The ensemble of these subcolumns reproduces the overall mean profile of the coarser grid cell of the model [Räisänen et al., 2004]. Finally, for each model cell, the McICA approximation is applied to the set of subcolumns generated to compute the broadband energy fluxes.

The instrument simulators contained in the COSP package exploit the same principle: the Subgrid Cloud Overlap Profile Sampler (SCOPS) [Bodas-Salcedo et al., 2011] provides a set of subcolumns to mimic the footprint size of the simulated instrument and to directly

compare the synthetic observations with the real ones [Oreopoulos et al., 2022]. However, SCOPS is a built-in module of COSP while the radiation scheme adopted in the climate model is coupled with its own subcolumns generator.

Initially developed for the ISSCP simulator, SCOPS generates subgrid profiles of cloud cover, ice and water content that are compatible with the mean vertical profiles of clouds of the model grid cell, on the basis of one of the overlap rules presented in 1.3.3.

SCOPS accounts for convective and stratiform clouds: for each type, the cloud fraction of the generated subcolumns at the different layers is 0 or 1, and the water and ice content are horizontally homogeneous. The same scheme can be applied for the hydrometeors.

In chapter 4.3.1, by restricting the analysis to clear-sky ocean areas, we avoided the difficulties arising from the representation of sub-grid cloud structure, directly providing the atmospheric profiles of the model grid cells to the  $COSP + \sigma - IASI$  tool.

To extend the comparison between simulated and observed radiances to all-sky conditions, a different approach has to be adopted, and here we present some preliminary results in that direction. First of all, to mimic the size of IASI pixel, whose diameter is about 12 km, at least 50 subcolumns have to be generated starting from the EC-Earth grid-cell, which covers an area of 80x80 km at the equator. Then, the SCOPS code is applied to generate a set of subcolumns for each grid cell, on the basis of the "maximum-random overlap" scheme. As a consequence, in addition to the whole-cell variables, mentioned in Section 4.1.1, the  $\sigma - IASI$  RTM now receives as input N subcolumn profiles of cloud cover, ice and water cloud content, ice and water radius of the cloud particles.

In this new configuration, the whole-cell radiance should be computed as:

$$R_{tot} = \frac{1}{N} \sum_{n=1}^N R_n \quad (5.1)$$

where  $R_{tot}$  is the radiance averaged over the N sub-columns (with  $N = 50$ ) and  $R_n$  is the radiance computed for a single sub-column. This operation produces a strong increase of the computational cost of the model simulation. First of all, in presence of clouds,  $\sigma - IASI$  requires more computational resources to solve the radiative transfer equation. In addition, the RTM should be called for each subcolumn ( $R_n$ ). In this configuration, the estimated computational cost of the tool  $COSP + \sigma - IASI$  becomes approximately 200 times higher than the cost required in clear-sky conditions. For the climate model simulation, this means passing from the initial 4000 CHPSY to the prohibitive computational cost of 800 000 CHPSY. Moreover, the synthetic radiance calculated in this way is not directly comparable to the IASI measurements, which involves a single pixel at a time.

Since we will compare EC-Earth and IASI climatologies, we consider here the radiance average over a relatively long time period. Following an approach similar to that adopted in the McICA approximation (see equation 1.3.3), we can express the temporal averaged radiance as:

$$\overline{R_{tot}} = \frac{1}{N} \frac{1}{T} \sum_{n=1}^N \sum_{t=1}^T R_{n,t} \quad (5.2)$$

where  $R_{n,t}$  is the radiance computed for the n-th subcolumn at each time step t of the time range  $T$ .

To reduce the computational cost of 5.2, we randomly pick only one subcolumn  $n$  in each grid cell for each time step  $t$ :

$$\overline{R_{tot}} \approx \frac{1}{T} \sum_{t=1}^T R_{n_t} \quad (5.3)$$

Now  $R_{n_t}$  is the radiance computed at time step  $t$  for a randomly selected subcolumn  $n$ . In this way,  $\sigma - IASI$  RTM is called only once per grid cell and the computational cost of the simulation is not burdened with the high number of generated sub-columns. Moreover, in this way we simulate the all-sky radiance for a single subcolumn, whose dimension is directly compatible with the field of view of IASI instrument.

Summarizing, there are three possible strategies for the computation of the all-sky radiances:

1. The radiative transfer equation is solved using the mean profiles of the cloud properties relative to the ECE grid cell, without the generation of subcolumns. More in detail, the grid cell profiles of clouds used in the simulation are computed in IFS using a generalised cloud overlap assumption between maximum and random: the degree of randomness between two layers increases with increasing vertical separation distance between the layers [Hogan and Illingworth, 2000]
2. Radiative computations are performed for all the subcolumns generated (high computation cost)
3. Radiative transfer is computed for one randomly selected subcolumns whose dimension is compatible with the IASI field of view (equation 5.3)

Here, we present a first comparison between methods 1 and 3, applied to a single time step  $t_1$  of the model (January 2008, 6 AM).

The model cloud field at  $t_1$  is shown in Figure 5.1, while the differences between radiance fields computed with the method 3 and method 1 are shown for a spectral ( $880 \text{ cm}^{-1}$ ) of the atmospheric window in figure 5.2. This channel is selected because the differences between radiances computed in clear and all-sky condition are generally larger in the atmospheric window.

With method 3, that considers only one subcolumn, it is more likely to pick a clear-sky scene because while the subcolumn is representative of an area of about  $100 \text{ km}^2$ , the coarse grid cell of the model represents an area of approximately  $6000 \text{ km}^2$ .

The analysis presented in this Section is preliminary and further work is needed in this direction. However, the result provided by method 3 above (a single random subcolumn) seems promising for the final implementation of the all-sky simulator in EC-Earth.

## 5.2 Spectral trends

Starting from the climatologies of the observed and synthetic spectra, provided by IASI and EC-Earth, we evaluate linear trends in clear-sky spectrally resolved radiances, following the approach presented by Whitburn et al. [2021]. In that work, trends are calculated

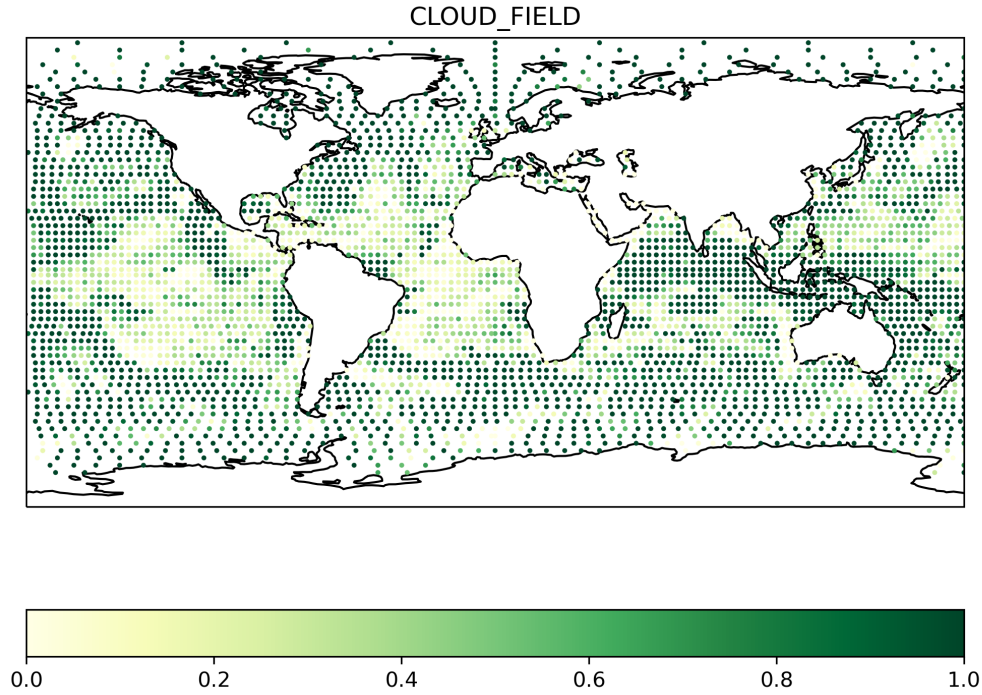


Figure 5.1: Simulated total cloud fraction for January 2008 - 06 UTC

from 10 years of IASI spectrally resolved fluxes, on the basis of the algorithm described in [Whitburn et al. \[2020\]](#).

We here obtain the trends of OLR radiances by performing a fit of a Fourier series in each spectral band, over steps of  $10 \text{ cm}^{-1}$ , using the method presented in [Gardiner et al. \[2008\]](#).

$$F(t, b_0, \mathbf{c}, \mathbf{d}) = b_0 t + \sum_{i=1}^8 \left( c_i \cos\left(\frac{2\pi t}{T_i}\right) + d_i \sin\left(\frac{2\pi t}{T_i}\right) \right) \quad (5.4)$$

In this equation,  $t$  is measured in months and  $b_0, c_i, d_i$  are the fitting parameters. The terms in the sum are eight sine and eight cosine functions and represent the periodic oscillations with period  $T_i$ . In  $T_i$  we include annual (12 months), semi-annual (6 months), and other characteristic atmospheric periodicities of 3, 4, 8, 9, 24 and 36 months [[Haenel et al., 2015](#)], [[Valeri et al., 2017](#)].

In [Figures 5.3 and 5.4](#), the trends are computed from the monthly zonal means of OLR and are provided as the relative variation of the OLR with respect to 2008 (expressed in percent). While in the case of IASI data we focus on MIR spectral range, here restricted between  $650$  and  $2250 \text{ cm}^{-1}$ , in the case of EC-Earth, we simulated radiances also in the FIR, so the analysis is extended to the spectral interval between  $200$  to  $2250 \text{ cm}^{-1}$ .

Generally, the pattern of simulated and observed trends is in good agreement over the MIR spectral range, where both the measurements and the simulations are available.

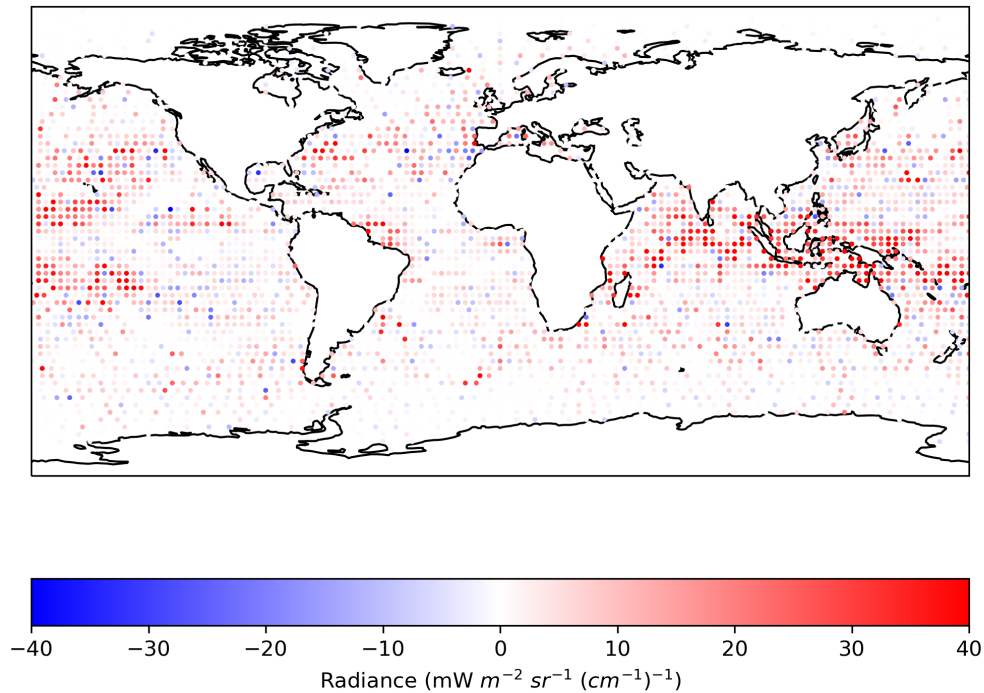


Figure 5.2: Radiance difference at  $880\text{ cm}^{-1}$  between method 3 and method 1

Indeed, the core of the  $\text{CO}_2$  band [ $660\text{-}670\text{ cm}^{-1}$ ] shows a negative trend over tropical and subtropical latitudes, while it is positive in mid-latitudes. In contrast, the wing of  $\text{CO}_2$  [ $690\text{-}730\text{ cm}^{-1}$ ] is uniformly negative at all latitudes. In the atmospheric windows (AW1 and AW2 in Table 4.3), both simulated and observed radiances provide small positive trends, with most significant discrepancies at mid-latitudes, where, however, the number of clear-sky spectra involved in the analysis is very small (see Section 4.3.3). Finally, the largest differences occur in the water vapour band (WV2), even if the signs of the trends are generally consistent, especially in the tropics.

To better investigate the physical causes of the spectral trends, we also show the trend computed from EC-Earth simulated radiances on a global scale in the four spectral bands already analyzed in the previous chapter (Fig. 4.13). More in detail, Figure 5.5 - panel A shows the plot of ECE trends of the monthly means OLR computed for each model grid cell in the atmospheric window AW1 ( $850\text{ cm}^{-1}$ ). Panel B describes the trends centered at  $660\text{ cm}^{-1}$ , panel C shows the ECE trends at  $730\text{ cm}^{-1}$  and panel D describes the ECE trends at  $1400\text{ cm}^{-1}$ .

In the following sections, we show how the spectral trends, in this example limited to the atmospheric window and to the  $\text{CO}_2$  band, can provide detailed information about the evolution of the main variables of climate system and its impact on the OLR.

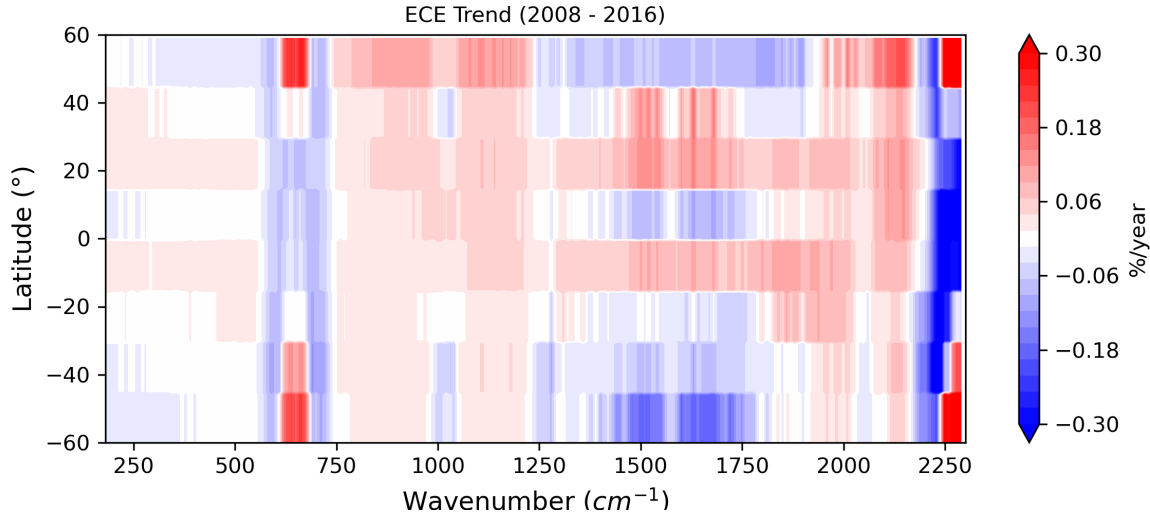


Figure 5.3: Zonal mean spectrally resolved linear trends from ECE climate model (2008-2016)

### Atmospheric window

In the atmospheric windows AW1 and AW2 (Table 4.3), the OLR at TOA is mainly controlled by the change in surface temperature. As a consequence, trends found in these spectral regions are closely linked to the change in the surface temperatures. Since the ECE model was run with prescribed SSTs and SIC, from January 2008 to December 2016, a very similar pattern is expected in trends of IASI clear-sky radiances in the atmospheric window.

Despite the zonal averages show a uniform positive trend (Fig. 5.3), the plot in Fig. 5.5 (panel A) highlights a significant spatial heterogeneity.

Starting from the Northern hemisphere, we can observe a region of negative trend in the North Atlantic. According to [Whitburn et al., 2021], this is related to the North Atlantic Warming Hole (WH) and it is identified as a consequence of the weakening of the Atlantic Meridional Overturning Circulation (AMOC) and the increase of the ice melting rate in Greenland. In fact, AMOC is responsible for the transport of warm tropical masses in the North Atlantic and climate projections indicate a weakening of this process causing a cooling of the subpolar Arctic [Keil et al., 2020] in the last decades, despite global warming.

In the North Eastern Pacific, we can distinguish a large area affected by a strong positive trend. This is likely the effect of the Pacific Decadal Oscillation (PDO), a periodic surface temperature anomaly in the Pacific Ocean. When the interior Pacific is cool, the temperatures along the Pacific coast are above the climatic average and PDO is defined as positive. Otherwise, the PDO is defined as negative and the temperature anomalies are inverted. The period we take into account starts with a negative PDO (during 2008-2012) and ends with a positive PDO (during 2014-2016), directly affecting the trends over the Pacific Ocean.

In the Southern Hemisphere, the occurrence of a strong La El Niña episode in 2010-2011 and a strong El Niño event in 2015-2016 affects dramatically the trends, providing a positive trend ( about  $0.1 \text{ %/year}$ , or  $0.7 \cdot 10^{-4} \text{ Wm}^{-2}$  per year) over the Tropical Pacific Ocean.

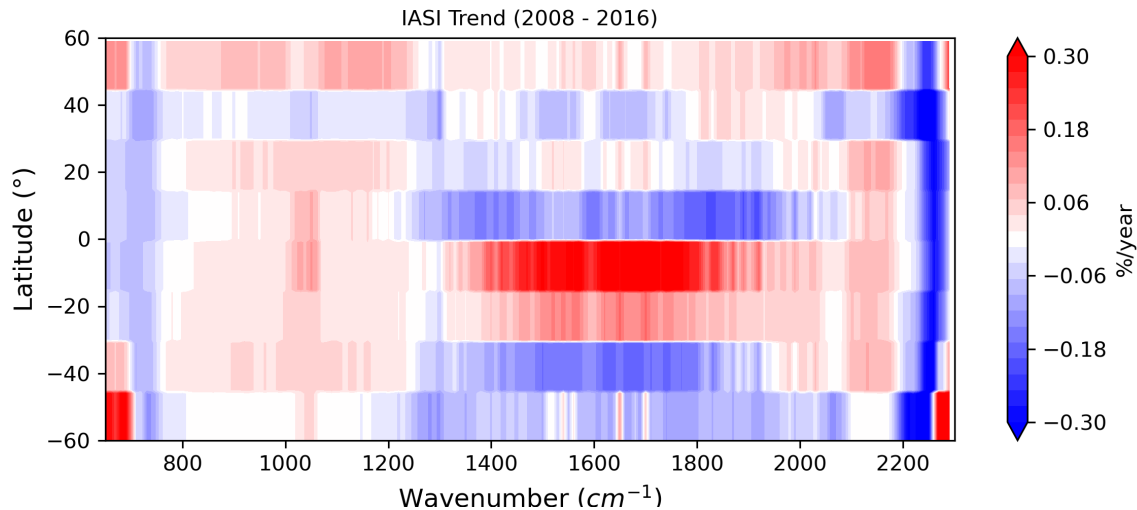


Figure 5.4: Zonal mean spectrally resolved linear trends from IASI (2008-2016)

### CO<sub>2</sub> band

In the core of the CO<sub>2</sub> spectral band, where OLR measured at TOA is emitted mainly from the stratosphere, positive trend dominates at high latitudes, while negative trends occur over the Tropical Ocean (see Fig. 5.3 and Fig. 5.4). Conversely, the wings of CO<sub>2</sub> spectral band, particularly sensitive to the mid-troposphere are characterized by negative trends at all latitudes in both cases. The global OLR trends provided by ECE in these spectral bands are shown in Figure 5.5, panel B (660 cm<sup>-1</sup> core CO<sub>2</sub>) and C (730 cm<sup>-1</sup> wing CO<sub>2</sub>).

Trends in stratosphere and troposphere are mainly affected by the change of temperature at these altitudes and by the increase of greenhouse gases concentration. In turn, global atmospheric temperatures are conditioned by a strengthening of the Brewer-Dobson Circulation (BDO) under climate warming. This global scale circulation is responsible for the rise and intrusion of tropospheric air into the stratosphere at tropical latitudes and the consequent transport of these air masses poleward until their descent at middle and high latitudes [Butchart, 2014]. Due to the increase of greenhouse gases and SSTs, this circulation is accelerating causing a warming of the troposphere at the tropics and a cooling of the lower stratosphere [Garcia and Randel, 2008]. Conversely, at high latitudes the strengthening of the descending motion of the stratospheric air masses produces an increase of the temperature due to the adiabatic heating.

This could explain the different signs of trends in the tropics and mid-latitudes in Figures 5.3 and 5.4 and in the panel B of Figure 5.5.

Finally, in the wings of the CO<sub>2</sub> band, trends are always negative due to the increase of CO<sub>2</sub> concentration in the atmosphere (see panel C of Figure 5.5). This causes a shift of the radiation emission level at higher, and then cooler, tropospheric altitudes and is the main driver of present-day climate change.

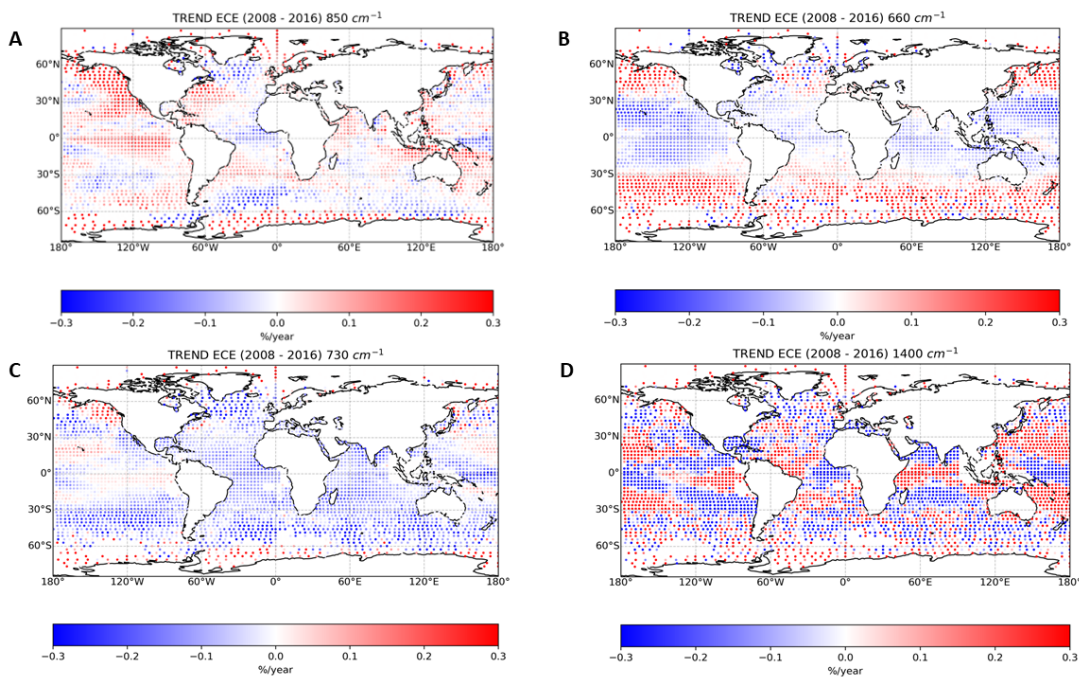


Figure 5.5: Global Trends computed on the basis of ECE simulated radiances over the period 2008-2016. Panel A describes trends in the atmospheric window at 850  $cm^{-1}$ , panel B represents trends at 660  $cm^{-1}$ , panel C shows trends at 730  $cm^{-1}$  and panel D describes trends at 1400  $cm^{-1}$

# Conclusions

The availability of long-term measurements of broadband integrated energy fluxes at Top of the Atmosphere makes these data the standard benchmark to evaluate the ability of general circulation models to represent the Earth’s radiation budget and hence to infer on climate evolution. For this reason, climate models are systematically tuned to best match the observed broadband fluxes, mainly provided by the ERBE mission [Barkstrom, 1984], started in the mid-70s, and the more recent CERES mission [Loeb et al., 2018], which is the current reference dataset.

In the first part of this work, we followed this standard approach and we compared the main variables contributing to the ERB, simulated by 34 state-of-the-art climate models participating to CMIP6, with CERES observational data, over the period 2000-2014. On a global scale, the simulated values are generally consistent with the observed quantities and the CMIP6 models perform better than any previous model generation [Wild, 2020]. In particular, the global average of the OLR and the OSR fluxes in all-sky conditions are found within the calibration error of CERES, which is equal to about  $4 \text{ Wm}^{-2}$  and  $2 \text{ Wm}^{-2}$  (corresponding to two standard deviations), in the two spectral regions, respectively. However, the spatial distribution of the biases highlights large regional differences: in the case of the all-sky OLR, we found biases reaching  $10 \text{ Wm}^{-2}$  at the tropical latitudes, while the OSR in all-sky conditions showed even larger biases, up to  $30 \text{ Wm}^{-2}$  over the subtropical regions.

By comparing energy fluxes in all and clear-sky conditions, the greatest source of uncertainty in GCMs has been identified in the representation of clouds and, consequently, in the effects of clouds on solar and thermal radiation. Specifically, the largest biases are detected in the subtropics and over the Southern Ocean, that are the areas more affected by the presence of low marine clouds. At the subtropics, simulated cloud cover is less than the observed value and this could explain the low simulated reflectivity of solar radiation highlighted in the multi-model mean. Furthermore, most models share the uniform negative bias of the OSR over the Southern Ocean. It is hypothesized that this long-standing bias could be generated by an insufficient amount of simulated supercooled liquid clouds modelled at these latitudes [Kay et al., 2016].

In clear-sky conditions, OLR and OSR model biases are generally much smaller as compared to all-sky case. The main sources of biases for the clear-sky OSR are mainly attributed to surface albedo and to the too high snow reflectivity, affecting polar regions. In some regions, also the complexity of the topography, that is roughly approximated in climate models, contributes to this bias. Although referring to simplified atmospheric conditions, clear-sky OLR is still affected by a uniform negative bias, present at all the latitudes. In this framework, we stressed that a complication may arise in this comparison, due to the different approaches used in climate models and CERES in computing energy fluxes in the absence of clouds.

An additional problem to be considered consists in the fact that even when simulated energy fluxes are very close to the observed ones, a seemingly good agreement may be due to compensation errors occurring in different spectral bands. For this reason, in the second part of this PhD work, we aimed to highlight the significant contribution of satellite measurements of the *outgoing longwave spectrally resolved radiances* in the evaluation of climate models performances. In fact, starting from the analysis of the spectral radiances, the signatures of the main climate variables can be identified, separated and used to assess climate model biases. In addition, spectra measured on a global scale represent a more accurate benchmark than those provided by reanalysis datasets, which are computed assimilating observations in model simulations. Moreover, the direct comparison of spectral radiances is not affected by the systematic biases affecting atmospheric profiles derived by applying a priori constraints to otherwise severely ill-conditioned inversions of satellite nadir spectral measurements.

This kind of comparison is possible because stable hyperspectral measurements have been performed since the mid-2000s, and, nowadays, long time series of OLR spectral radiances are available for the exploitation from a climate perspective. Specifically, the Mid-Infrared spectral range (667 to 2750  $\text{cm}^{-1}$ ) has been deeply investigated thanks to the measurements of various space-borne sensors (IASI, AIRS, etc.) on a global scale, while the Far-Infrared region, from 100 to 667  $\text{cm}^{-1}$ , will be explored from space from 2027, by the FORUM instrument, selected to be the ninth ESA Earth Explorer mission. Both IASI-NG and FORUM are Fourier Transform Spectrometer and they will fly in loose formation to acquire high resolution radiances of all the Earth emission spectrum.

On the basis of these considerations, we compared 9 years of IASI clear-sky radiances to synthetic spectra extracted from the EC-Earth GCM, a state-of-the-art European model based on ECMWF’s Integrated Forecasting System for the atmosphere–land component. IASI radiances climatology is built from the Fundamental Climate Data Record (FCDR) of the reprocessed Metop-A Level 1c product, provided by EUMETSAT through the European Weather Cloud (EWC) service. To simulate spectra based on the atmospheric and surface state provided by the climate model, the radiative transfer model  $\sigma$ –IASI has been integrated within the COSP package inside the EC-Earth model. The implementation of the RTM is required to produce OLR radiances because the radiative scheme of climate models can only provide integrated energy fluxes using approximated procedures, such as the correlated-k distribution method [Mlawer et al., 1997] and the McICa approximation [Pincus et al., 2003].

Even if the  $\sigma$ –IASI RTM had already been validated against IASI measurements, Aircraft Measurements (NAST-I) and ground-based measurements, before implementing  $\sigma$ –IASI in the EC-Earth climate model, the accuracy of this RTM in the FIR region was further tested by comparison with REFIR-PAD measurements acquired in 2005 during a stratospheric balloon campaign from Teresina (Brazil). During this experiment, on-board a balloon gondola, the REFIR-PAD instrument measured for the first time the FIR spectral range, without the use of cooled detectors, laying the ground for the future FORUM mission. At the same time, IASI balloon, hosted on the same platform, performed measurements in the MIR spectral interval.

To assess the  $\sigma$ –IASI accuracy, we first retrieved the atmospheric profiles using a Bayesian inversion algorithm based on the  $\sigma$ –IASI and then, starting from the retrieved profiles, we simulated the spectral radiances. Since  $\sigma$ –IASI is able to provide high-resolution radiances that can be convolved with the Spectral Response Function of any

## Conclusions

---

instrument, we simulated both the REFIR-PAD and the IASI balloon measured spectra. We found a very good agreement between observed and simulated radiances, in both cases.

After the implementation of the new *COSP +  $\sigma$  - IASI* module in EC-Earth, we performed an atmosphere-only simulation from 2008 to 2016, with prescribed sea surface temperature and sea-ice concentration, to generate a set of synthetic radiances in clear-sky conditions. The outputs have been provided every 6 hours, in  $10 \text{ cm}^{-1}$  spectral bands for the time period 2008-2016. The same conditions have been used to build a climatology of IASI clear-sky spectral radiance measurements.

The long term comparison between EC-Earth simulated radiances and IASI observed radiances has shown the presence of a warm positive model bias ( $\approx 3.5 \text{ K}$ ) in the stratosphere and a smaller ( $\approx 1 \text{ K}$ ) negative temperature bias in the troposphere. Finally, we have found a positive bias in the model BTs relating to the water vapour spectral band, which is caused by an under-estimation of water vapour in the EC-Earth upper troposphere. These biases have been further confirmed through the comparison of the profiles of temperature and water vapour of the EC-Earth climate model and the ERA5 reanalysis.

Long-term spectrally resolved radiances are still poorly exploited to test and improve climate models performance. This work shows a fruitful approach to detect biases in climate model and opens new possibilities for extending the analysis in presence of clouds, that represent the greatest source of uncertainty in models. The same approach can be extended to the comparison of trends in the spectral radiance, which are directly linked to specific climate feedbacks. In addition, in the near future, the comparison will hopefully be extended to include FORUM FIR measurements, for a comprehensive analysis of the climate model ability in reproducing the whole Earth emission spectrum.



# Acknowledgements

At this point, I'd like to take time to thank all the people I worked profitably together: Dr. Piera Raspollini and Dr. Ugo Cortesi and all the group "Sondaggio dell'Atmosfera" of the "Istituto di Fisica Applicata Nello Carrara" in Florence, Dr. Federico Fabiano (ISAC-CNR), Dr. Marco Ridolfi (INO-CNR), Prof. Jost Von Hardenberg (Politecnico di Torino) and Prof. Tiziano Maestri (Università di Bologna).

Thank you for giving me the opportunity to work on a new, complex and challenging topic, about the most fascinating subject I know.

Thanks to Prof. Carmine Serio, Prof. Guido Masiello and Dr. Sara Venafra from "Università degli studi della Basilicata", who made available the sigma-IASI code, developed in the framework of FORUM-SCIENZA project (No. 2019-20-HH.0), founded by the Italian Space Agency.

Thanks to CINECA for providing computational resources through the Italian Super-Computing Resource Allocation and EUMETSAT for making available the huge amount of L1c IASI data through the European Weather Cloud service (EWC).

Thanks to Prof. Quentin Libois and Dr. Lucie Leonarsky for the interesting insights they gave me, on the basis of the useful collaboration we have established.

Thanks again to Federico, who, during these years, taught me that every "wrong run" can be followed by the correct one.

Thanks to my Family, for the perspective it gave me from which to look at the future.

Thanks to my Friends and the jungle vines that hold us together.

Finally, thanks to Carmen for the efforts she made to keep building our world.



# Bibliography

- Amato, U., Masiello, G., Serio, C., and Viggiano, M. (2002). The  $\sigma$ -iasi code for the calculation of infrared atmospheric radiance and its derivatives. *Environmental Modelling & Software*, 17(7):651–667.
- Anderson, G. P., Clough, S. A., Kneizys, F., Chetwynd, J. H., and Shettle, E. P. (1986). Aflgl atmospheric constituent profiles (0.120 km). Technical report, Air Force Geophysics Lab Hanscom AFB MA.
- Balsamo, G., Beljaars, A., Scipal, K., Viterbo, P., van den Hurk, B., Hirschi, M., and Betts, A. K. (2009). A revised hydrology for the ecmwf model: Verification from field site to terrestrial water storage and impact in the integrated forecast system. *Journal of hydrometeorology*, 10(3):623–643.
- Barker, H., Cole, J., Morcrette, J.-J., Pincus, R., Räisänen, P., von Salzen, K., and Vaillancourt, P. (2008). The monte carlo independent column approximation: An assessment using several global atmospheric models. *Quarterly Journal of the Royal Meteorological Society*, 134(635):1463–1478.
- Barkstrom, B. R. (1984). The earth radiation budget experiment (erbe). *Bulletin of the american meteorological society*, 65(11):1170–1185.
- Bloom, H. J. (2001). The cross-track infrared sounder (cris): a sensor for operational meteorological remote sensing. In *IGARSS 2001. Scanning the Present and Resolving the Future. Proceedings. IEEE 2001 International Geoscience and Remote Sensing Symposium (Cat. No. 01CH37217)*, volume 3, pages 1341–1343. IEEE.
- Blumstein, D., Chalon, G., Carlier, T., Buil, C., Hebert, P., Maciaszek, T., Ponce, G., Phulpin, T., Tournier, B., Simeoni, D., et al. (2004). Iasi instrument: Technical overview and measured performances. In *Infrared Spaceborne Remote Sensing XII*, volume 5543, pages 196–207. SPIE.
- Bodas-Salcedo, A., Webb, M., Bony, S., Chepfer, H., Dufresne, J.-L., Klein, S., Zhang, Y., Marchand, R., Haynes, J., Pincus, R., et al. (2011). Cosp: Satellite simulation software for model assessment. *Bulletin of the American Meteorological Society*, 92(8):1023–1043.
- Brindley, H. and Bantges, R. (2016). The spectral signature of recent climate change. *Current Climate Change Reports*, 2(3):112–126.
- Brindley, H., Bantges, R., Russell, J., Murray, J., Dancel, C., Belotti, C., and Harries, J. (2015). Spectral signatures of earth’s climate variability over 5 years from iasi. *Journal of Climate*, 28(4):1649–1660.

- 
- Brindley, H. E. and Harries, J. E. (1998). The impact of far ir absorption on clear sky greenhouse forcing: sensitivity studies at high spectral resolution. *Journal of Quantitative Spectroscopy and Radiative Transfer*, 60(2):151–180.
- Butchart, N. (2014). The brewer-dobson circulation. *Reviews of geophysics*, 52(2):157–184.
- Carli, B., Barbis, A., Harries, J. E., and Palchetti, L. (1999). Design of an efficient broadband far-infrared fourier-transform spectrometer. *Applied optics*, 38(18):3945–3950.
- Clerbaux, C., Boynard, A., Clarisse, L., George, M., Hadji-Lazaro, J., Herbin, H., Hurtmans, D., Pommier, M., Razavi, A., Turquety, S., et al. (2009). Monitoring of atmospheric composition using the thermal infrared iasi/metop sounder. *Atmospheric Chemistry and Physics*, 9(16):6041–6054.
- Cortesi, U., Del Bianco, S., Gai, M., Laurenza, L. M., Ceccherini, S., Carli, B., Barbara, F., and Buchwitz, M. (2014). Sensitivity analysis and application of klima algorithm to gosat and oco validation. *Technical, scientific and research reports*, 6:1–153.
- Del Bianco, S., Carli, B., Gai, M., Laurenza, L. M., and Cortesi, U. (2013). Xco2 retrieved from iasi using klima algorithm. *Annals of Geophysics*, 56.
- Della Fera, S., Fabiano, F., Raspollini, P., Ridolfi, M., Cortesi, U., Barbara, F., and von Hardenberg, J. (2022). On the use of iasi spectrally resolved radiances to test the ec-earth climate model (v3. 3.3) in clear-sky conditions. *EGUsphere*, pages 1–22.
- Dewitte, S. and Clerbaux, N. (2017). Measurement of the earth radiation budget at the top of the atmosphere—a review. *Remote Sensing*, 9(11):1143.
- Dines, W. (1917). The heat balance of the atmosphere. *Quarterly Journal of the Royal Meteorological Society*, 43(182):151–158.
- Döscher, R., Acosta, M., Alessandri, A., Anthoni, P., Arneth, A., Arsouze, T., Bergmann, T., Bernadello, R., Bousetta, S., Caron, L.-P., et al. (2021). The ec-earth3 earth system model for the climate model intercomparison project 6. *Geoscientific Model Development Discussions*, pages 1–90.
- Edwards, P. and Pawlak, D. (2000). Metop: The space segment for eumetsat’s polar system. *ESA bulletin*, pages 7–18.
- Edwards, P. N. (2011). History of climate modeling. *Wiley Interdisciplinary Reviews: Climate Change*, 2(1):128–139.
- Eyring, V., Bony, S., Meehl, G. A., Senior, C. A., Stevens, B., Stouffer, R. J., and Taylor, K. E. (2016). Overview of the coupled model intercomparison project phase 6 (cmip6) experimental design and organization. *Geoscientific Model Development*, 9(5):1937–1958.
- Fichefet, T. and Maqueda, M. M. (1997). Sensitivity of a global sea ice model to the treatment of ice thermodynamics and dynamics. *Journal of Geophysical Research: Oceans*, 102(C6):12609–12646.

- 
- Fortuin, J. P. and Langematz, U. (1995). Update on the global ozone climatology and on concurrent ozone and temperature trends. In *Atmospheric Sensing and Modelling*, volume 2311, pages 207–216. International Society for Optics and Photonics.
- Garcia, R. R. and Randel, W. J. (2008). Acceleration of the brewer–dobson circulation due to increases in greenhouse gases. *Journal of the Atmospheric Sciences*, 65(8):2731–2739.
- Gardiner, T., Forbes, A., De Mazière, M., Vigouroux, C., Mahieu, E., Demoulin, P., Velasco, V., Notholt, J., Blumenstock, T., Hase, F., et al. (2008). Trend analysis of greenhouse gases over europe measured by a network of ground-based remote ftir instruments. *Atmospheric Chemistry and Physics*, 8(22):6719–6727.
- Grieco, G., Masiello, G., Matricardi, M., Serio, C., Summa, D., and Cuomo, V. (2007). Demonstration and validation of the  $\varphi$ -iasi inversion scheme with nast-i data. *Quarterly Journal of the Royal Meteorological Society: A journal of the atmospheric sciences, applied meteorology and physical oceanography*, 133(S3):217–232.
- Guidard, V., Fourrié, N., Brousseau, P., and Rabier, F. (2011). Impact of iasi assimilation at global and convective scales and challenges for the assimilation of cloudy scenes. *Quarterly Journal of the Royal Meteorological Society*, 137(661):1975–1987.
- Haenel, F., Stiller, G., Von Clarmann, T., Funke, B., Eckert, E., Glatthor, N., Grabowski, U., Kellmann, S., Kiefer, M., Linden, A., et al. (2015). Reassessment of mipas age of air trends and variability. *Atmospheric Chemistry and Physics*, 15(22):13161–13176.
- Hansen, J., Sato, M., Kharecha, P., and Von Schuckmann, K. (2011). Earth’s energy imbalance and implications. *Atmospheric Chemistry and Physics*, 11(24):13421–13449.
- Harries, J., Carli, B., Rizzi, R., Serio, C., Mlynchak, M., Palchetti, L., Maestri, T., Brindley, H., and Masiello, G. (2008). The far-infrared earth. *Reviews of Geophysics*, 46(4).
- Hazeleger, W., Severijns, C., Semmler, T., Ștefănescu, S., Yang, S., Wang, X., Wyser, K., Dutra, E., Baldasano, J. M., Bintanja, R., et al. (2010). Ec-earth: a seamless earth-system prediction approach in action. *Bulletin of the American Meteorological Society*, 91(10):1357–1364.
- Hersbach, H., Bell, B., Berrisford, P., Hirahara, S., Horányi, A., Muñoz-Sabater, J., Nicolas, J., Peubey, C., Radu, R., Schepers, D., et al. (2020). The era5 global reanalysis. *Quarterly Journal of the Royal Meteorological Society*, 146(730):1999–2049.
- Hogan, R. J. and Illingworth, A. J. (2000). Deriving cloud overlap statistics from radar. *Quarterly Journal of the Royal Meteorological Society*, 126(569):2903–2909.
- Hogan, R. J. and Matricardi, M. (2020). Evaluating and improving the treatment of gases in radiation schemes: the correlated k-distribution model intercomparison project (ckdmip). *Geoscientific Model Development*, 13(12):6501–6521.
- Hourdin, F., Mauritsen, T., Gettelman, A., Golaz, J.-C., Balaji, V., Duan, Q., Folini, D., Ji, D., Klocke, D., Qian, Y., et al. (2017). The art and science of climate model tuning. *Bulletin of the American Meteorological Society*, 98(3):589–602.

- 
- Huang, X., Ramaswamy, V., and Schwarzkopf, M. D. (2006). Quantification of the source of errors in am2 simulated tropical clear-sky outgoing longwave radiation. *Journal of Geophysical Research: Atmospheres*, 111(D14).
- Huang, Y. and Ramaswamy, V. (2009). Evolution and trend of the outgoing longwave radiation spectrum. *Journal of climate*, 22(17):4637–4651.
- Huang, Y., Ramaswamy, V., Huang, X., Fu, Q., and Bardeen, C. (2007). A strict test in climate modeling with spectrally resolved radiances: Gcm simulation versus airs observations. *Geophysical Research Letters*, 34(24).
- Hurrell, J. W., Hack, J. J., Shea, D., Caron, J. M., and Rosinski, J. (2008). A new sea surface temperature and sea ice boundary dataset for the community atmosphere model. *Journal of Climate*, 21(19):5145–5153.
- Kay, J. E., Wall, C., Yettella, V., Medeiros, B., Hannay, C., Caldwell, P., and Bitz, C. (2016). Global climate impacts of fixing the southern ocean shortwave radiation bias in the community earth system model (cesm). *Journal of Climate*, 29(12):4617–4636.
- Keil, P., Mauritsen, T., Jungclaus, J., Hedemann, C., Olonscheck, D., and Ghosh, R. (2020). Multiple drivers of the north atlantic warming hole. *Nature Climate Change*, 10(7):667–671.
- Khanal, S., Wang, Z., and French, J. R. (2020). Improving middle and high latitude cloud liquid water path measurements from modis. *Atmospheric research*, 243:105033.
- Kiehl, J. T. and Trenberth, K. E. (1997). Earth’s annual global mean energy budget. *Bulletin of the American meteorological society*, 78(2):197–208.
- Le Marshall, J., Jung, J., Derber, J., Chahine, M., Treadon, R., Lord, S., Goldberg, M., Wolf, W., Liu, H., Joiner, J., et al. (2006). Improving global analysis and forecasting with airs. *Bulletin of the American Meteorological Society*, 87(7):891–894.
- Lee, W.-L., Liou, K., and Wang, C.-c. (2013). Impact of 3-d topography on surface radiation budget over the tibetan plateau. *Theoretical and applied climatology*, 113(1):95–103.
- LeMone, M. A. and Pennell, W. T. (1976). The relationship of trade wind cumulus distribution to subcloud layer fluxes and structure. *Monthly Weather Review*, 104(5):524–539.
- Liuzzi, G., Masiello, G., Serio, C., Meloni, D., Di Biagio, C., and Formenti, P. (2017). Consistency of dimensional distributions and refractive indices of desert dust measured over lampedusa with iasi radiances. *Atmospheric Measurement Techniques*, 10(2):599–615.
- Loeb, N. G., Doelling, D. R., Wang, H., Su, W., Nguyen, C., Corbett, J. G., Liang, L., Mitrescu, C., Rose, F. G., and Kato, S. (2018). Clouds and the earth’s radiant energy system (ceres) energy balanced and filled (ebaf) top-of-atmosphere (toa) edition-4.0 data product. *Journal of Climate*, 31(2):895–918.

- 
- Loeb, N. G., Rose, F. G., Kato, S., Rutan, D. A., Su, W., Wang, H., Doelling, D. R., Smith, W. L., and Gettelman, A. (2020). Toward a consistent definition between satellite and model clear-sky radiative fluxes. *Journal of Climate*, 33(1):61–75.
- Loeb, N. G., Wielicki, B. A., Doelling, D. R., Smith, G. L., Keyes, D. F., Kato, S., Manalo-Smith, N., and Wong, T. (2009). Toward optimal closure of the earth’s top-of-atmosphere radiation budget. *Journal of Climate*, 22(3):748–766.
- Lott, F. and Miller, M. J. (1997). A new subgrid-scale orographic drag parametrization: Its formulation and testing. *Quarterly Journal of the Royal Meteorological Society*, 123(537):101–127.
- Madec, G., Bourdallé-Badie, R., Bouttier, P.-A., Bricaud, C., Bruciaferri, D., Calvert, D., Chanut, J., Clementi, E., Coward, A., Delrosso, D., et al. (2017). Nemo ocean engine. *Bulletin of the American meteorological society*.
- Mauritsen, T., Stevens, B., Roeckner, E., Crueger, T., Esch, M., Giorgetta, M., Haak, H., Jungclaus, J., Klocke, D., Matei, D., et al. (2012). Tuning the climate of a global model. *Journal of advances in modeling Earth systems*, 4(3).
- Meinshausen, M., Nicholls, Z. R., Lewis, J., Gidden, M. J., Vogel, E., Freund, M., Beyerle, U., Gessner, C., Nauels, A., Bauer, N., et al. (2020). The shared socio-economic pathway (ssp) greenhouse gas concentrations and their extensions to 2500. *Geoscientific Model Development*, 13(8):3571–3605.
- Meinshausen, M., Vogel, E., Nauels, A., Lorbacher, K., Meinshausen, N., Etheridge, D. M., Fraser, P. J., Montzka, S. A., Rayner, P. J., Trudinger, C. M., et al. (2017). Historical greenhouse gas concentrations for climate modelling (cmip6). *Geoscientific Model Development*, 10(5):2057–2116.
- Meyssignac, B., Boyer, T., Zhao, Z., Hakuba, M. Z., Landerer, F. W., Stammer, D., Köhl, A., Kato, S., L’ecuyer, T., Ablain, M., et al. (2019). Measuring global ocean heat content to estimate the earth energy imbalance. *Frontiers in Marine Science*, 6:432.
- Minnis, P., Sun-Mack, S., Chen, Y., Chang, F.-L., Yost, C. R., Smith, W. L., Heck, P. W., Arduini, R. F., Bedka, S. T., Yi, Y., et al. (2020). Ceres modis cloud product retrievals for edition 4—part i: Algorithm changes. *IEEE Transactions on Geoscience and Remote Sensing*, 59(4):2744–2780.
- Mlawer, E. J., Taubman, S. J., Brown, P. D., Iacono, M. J., and Clough, S. A. (1997). Radiative transfer for inhomogeneous atmospheres: Rrtm, a validated correlated-k model for the longwave. *Journal of Geophysical Research: Atmospheres*, 102(D14):16663–16682.
- Norton, R. H. and Beer, R. (1976). New apodizing functions for fourier spectrometry. *J. Opt. Soc. Am.*, 66(3):259–264.
- Norton, R. H. and Beer, R. (1977). Errata: New apodizing functions for fourier spectrometry. *J. Opt. Soc. Am.*, 67(3):419–419.

- 
- Oreopoulos, L., Cho, N., Lee, D., Lebsock, M., and Zhang, Z. (2022). Assessment of two stochastic cloud subcolumn generators using observed fields of vertically resolved cloud extinction. *Journal of Atmospheric and Oceanic Technology*.
- Palchetti, L., Brindley, H., Bantges, R., Buehler, S., Camy-Peyret, C., Carli, B., Cortesi, U., Del Bianco, S., Di Natale, G., Dinelli, B., et al. (2020). unique far-infrared satellite observations to better understand how earth radiates energy to space. *Bulletin of the American Meteorological Society*, 101(12):E2030–E2046.
- Pincus, R., Barker, H. W., and Morcrette, J.-J. (2003). A fast, flexible, approximate technique for computing radiative transfer in inhomogeneous cloud fields. *Journal of Geophysical Research: Atmospheres*, 108(D13).
- Pithan, F., Shepherd, T. G., Zappa, G., and Sandu, I. (2016). Climate model biases in jet streams, blocking and storm tracks resulting from missing orographic drag. *Geophysical Research Letters*, 43(13):7231–7240.
- Qu, X., Hall, A., Klein, S. A., and Caldwell, P. M. (2014). On the spread of changes in marine low cloud cover in climate model simulations of the 21st century. *Climate dynamics*, 42:2603–2626.
- Räsänen, P., Barker, H. W., Khairoutdinov, M. F., Li, J., and Randall, D. A. (2004). Stochastic generation of subgrid-scale cloudy columns for large-scale models. *Quarterly Journal of the Royal Meteorological Society: A journal of the atmospheric sciences, applied meteorology and physical oceanography*, 130(601):2047–2067.
- Ridolfi, M., Del Bianco, S., Di Roma, A., Castelli, E., Belotti, C., Dandini, P., Di Natale, G., Dinelli, B. M., C-Labonnote, L., Palchetti, L., et al. (2020). Forum earth explorer 9: Characteristics of level 2 products and synergies with iasi-ng. *Remote Sensing*, 12(9):1496.
- Ridolfi, M., Tirelli, C., Ceccherini, S., Belotti, C., Cortesi, U., and Palchetti, L. (2022). Synergistic retrieval and complete data fusion methods applied to forum and iasi-ng simulated measurements. *Atmospheric Measurement Techniques Discussions*, pages 1–22.
- Rizzi, R., Palchetti, L., Carli, B., Bonsignori, R., Harries, J. E., Leotin, J., Peskett, S., Serio, C., and Sutera, A. (2002). Feasibility of the spaceborne radiation explorer in the far infrared (refir). In *Optical Spectroscopic Techniques, Remote Sensing, and Instrumentation for Atmospheric and Space Research IV*, volume 4485, pages 202–209. SPIE.
- Rodgers, C. D. (2000). *Inverse methods for atmospheric sounding: theory and practice*. Number 2 in Series on atmospheric, oceanic and planetary physics. World Scientific, Singapore.
- Rodgers, C. D. and Connor, B. J. (2003). Intercomparison of remote sounding instruments. *Journal of Geophysical Research: Atmospheres*, 108(D3).
- Serio, C., Masiello, G., Esposito, F., Di Girolamo, P., Di Iorio, T., Palchetti, L., Bianchini, G., Muscari, G., Pavese, G., Rizzi, R., et al. (2008). Retrieval of foreign-broadened water

- 
- vapor continuum coefficients from emitted spectral radiance in the h<sub>2</sub>o rotational band from 240 to 590 cm<sup>-1</sup>. *Optics Express*, 16(20):15816–15833.
- Soden, B. J. and Vecchi, G. A. (2011). The vertical distribution of cloud feedback in coupled ocean-atmosphere models. *Geophysical Research Letters*, 38(12).
- Sohn, B.-J., Schmetz, J., Stuhlmann, R., and Lee, J.-Y. (2006). Dry bias in satellite-derived clear-sky water vapor and its contribution to longwave cloud radiative forcing. *Journal of climate*, 19(21):5570–5580.
- Stephens, G. (1978). Radiation profiles in extended water clouds. i: Theory. *Journal of Atmospheric Sciences*, 35(11):2111–2122.
- Susskind, J., Molnar, G., Iredell, L., and Loeb, N. G. (2012). Interannual variability of outgoing longwave radiation as observed by airs and ceres. *Journal of Geophysical Research: Atmospheres*, 117(D23).
- Team, G. G. A. M. D., Anderson, J. L., Balaji, V., Broccoli, A. J., Cooke, W. F., Delworth, T. L., Dixon, K. W., Donner, L. J., Dunne, K. A., Freidenreich, S. M., et al. (2004). The new gfdl global atmosphere and land model am2–lm2: Evaluation with prescribed sst simulations. *Journal of Climate*, 17(24):4641–4673.
- Tiedtke, M. (1993). Representation of clouds in large-scale models. *Monthly Weather Review*, 121(11):3040–3061.
- Trenberth, K. E. and Fasullo, J. T. (2010). Simulation of present-day and twenty-first-century energy budgets of the southern oceans. *Journal of Climate*, 23(2):440–454.
- Trepte, Q., Minnis, P., and Arduini, R. F. (2003). Daytime and nighttime polar cloud and snow identification using modis data. In *Optical Remote Sensing of the Atmosphere and Clouds III*, volume 4891, pages 449–459. SPIE.
- Trepte, Q. Z., Minnis, P., Sun-Mack, S., Yost, C. R., Chen, Y., Jin, Z., Hong, G., Chang, F.-L., Smith, W. L., Bedka, K. M., et al. (2019). Global cloud detection for ceres edition 4 using terra and aqua modis data. *IEEE Transactions on Geoscience and Remote Sensing*, 57(11):9410–9449.
- Valeri, M., Barbara, F., Boone, C., Ceccherini, S., Gai, M., Maucher, G., Raspollini, P., Ridolfi, M., Sgheri, L., Wetzol, G., et al. (2017). Ccl 4 distribution derived from mipas esa v7 data: intercomparisons, trend, and lifetime estimation. *Atmospheric Chemistry and Physics*, 17(16):10143–10162.
- Vignesh, P. P., Jiang, J. H., Kishore, P., Su, H., Smay, T., Brighton, N., and Velicogna, I. (2020). Assessment of cmip6 cloud fraction and comparison with satellite observations. *Earth and Space Science*, 7(2):e2019EA000975.
- Von Schuckmann, K., Cheng, L., Palmer, M. D., Hansen, J., Tassone, C., Aich, V., Adusumilli, S., Beltrami, H., Boyer, T., Cuesta-Valero, F. J., et al. (2020). Heat stored in the earth system: where does the energy go? *Earth System Science Data*, 12(3):2013–2041.

- 
- Von Schuckmann, K., Palmer, M., Trenberth, K. E., Cazenave, A., Chambers, D., Champollion, N., Hansen, J., Josey, S., Loeb, N., Mathieu, P.-P., et al. (2016). An imperative to monitor earth’s energy imbalance. *Nature Climate Change*, 6(2):138–144.
- Waliser, D. E., Li, J.-L. F., Woods, C. P., Austin, R. T., Bacmeister, J., Chern, J., Del Genio, A., Jiang, J. H., Kuang, Z., Meng, H., et al. (2009). Cloud ice: A climate model challenge with signs and expectations of progress. *Journal of Geophysical Research: Atmospheres*, 114(D8).
- Whitburn, S., Clarisse, L., Bauduin, S., George, M., Hurtmans, D., Safieddine, S., Coheur, P. F., and Clerbaux, C. (2020). Spectrally resolved fluxes from iasi data: Retrieval algorithm for clear-sky measurements. *Journal of Climate*, 33(16):6971–6988.
- Whitburn, S., Clarisse, L., Bouillon, M., Safieddine, S., George, M., Dewitte, S., De Longueville, H., Coheur, P.-F., and Clerbaux, C. (2021). Trends in spectrally resolved outgoing longwave radiation from 10 years of satellite measurements. *npj climate and atmospheric science*, 4(1):1–8.
- Wild, M. (2020). The global energy balance as represented in cmip6 climate models. *Climate Dynamics*, 55:553–577.
- Zhang, H. and Jing, X. (2016). Advances in studies of cloud overlap and its radiative transfer in climate models. *Journal of Meteorological Research*, 30(2):156–168.